A Study of Vitrified Nuclear Wasteforms by Molecular Dynamics, Electron Microscopy and Raman Spectroscopy

Barrie J. Goodman

September 2015

A Thesis submitted to the University of Kent

in the subject of Physics

for the Degree of Master of Science

Main text word count: 24 953

Abstract

In this study an attempt is made to create molecular dynamics (MD) models of borate glass, alkali borosilicate glasses, and UK vitreous High Level Radioactive Wasteforms. The study also includes experimental studies of vitrified wasteforms by helium pycnometry, scanning electron microscopy (SEM), energy dispersive X-ray spectroscopy (EDX), X-ray florescence spectroscopy (XRF) and Raman spectroscopy.

Molecular dynamics models of alkali borosilicate glasses were created using Buckingham and BHM potentials in the constant pressure and temperature ensemble. The models using BHM potentials showed more realistic boron coordination numbers than those using Buckingham potentials. However structural features such as Si-O, Li-O and Na-O nearest neighbour distances and O-Si-O and O-B-O bond angles were considered satisfactory using Buckingham potentials.

SEM images showing phase separation in four different vitrified wasteforms are presented. The chemical composition of the phases were determined using SEM EDX. XRF spectroscopy was obtained from the wasteforms in powder form and show qualitative agreement with nominal compositions.

Raman spectroscopy also revealed the presence of MoO_4 tetrahedra in a glass environment and in phases such as $CaMoO_4$ and $Na(Gd,Nd)(MoO_4)_2$. The presence of ruthenium, cerium and zirconium phases were also found in the Raman spectra of wasteforms.

MD models of three simplified vitrified wasteforms were created using Buckingham potentials. Two models of each wasteform were created. The first models used only two-body potentials and showed MoO_6 octahedra connected to borosilicate network formers. In the second model of each wasteform, an additional O-Mo-O three-body potential was applied. The results of the second models showed MoO_4 tetrahedra detached from the borosilicate network which is a realistic feature in comparison to the experimental observations.

Acknowledgements

I would like to take this opportunity to thank my Supervisor Dr Gavin Mountjoy for the patience, inspiration and encouragement provided throughout the duration of this project.

I wish to acknowledge my 'better half' Charlene who became my wife and mother of my second daughter Isla during this work, and to thank Charlene for the all the sacrifices she and our eldest daughter Lexie made for me to complete this work.

Thanks also goes to Rick Short from the Nuclear Decommissioning Authority and to Mike Harrison from National Nuclear Laboratory for the information and samples provided.

Thanks to Timothy Kinnear for the all the help with learning Linux commands and altering FORTRAN codes that I would have been lost with otherwise.

Thank you to my work colleagues Andrew Clark, Adrian Tottenham and Wayne Chuter of the Safety Case Management team at Dungeness A Site for proofreading this document.

Finally I would like to thank my employer Magnox Ltd for partially financing this project.

CONTENTS

1. Introduction

1.1. High Level Nuclear Waste

In 2013 approximately 20% of electricity generated in the UK was generated by nuclear power plants [1]. At a nuclear power plant heat is generated in nuclear reactors by fission of uranium and plutonium atoms in nuclear fuel. Once nuclear fuel has come to the end of its useful life, it is removed from the reactor core and is either reprocessed so that any remaining useful material may be recovered and re-used (closed fuel cycle), or, it may be disposed of (open fuel cycle) [2]. Countries that reprocess nuclear fuel include China, France, India, Japan, Russia and the UK [3]. During reprocessing, fuel is dissolved in nitric acid and the useful elements (uranium and plutonium) are chemically extracted by a process known as the Plutonium-Uranium Extraction (PUREX) process [3], [4], [5]. In this process, uranium and plutonium are extracted whilst fission products, cladding materials, transuranic elements and traces of plutonium remain in the acid as a liquid waste form known as High Level Waste (HLW). Due to its plutonium content, HLW will remain radioactive for thousands of years [4].

1.2. Immobilisation of High Level Waste

The UK's preferred option for the long term management of HLW (and other radioactive waste) is storage in a purpose built Geological Disposal Facility (GDF) [6]. Prior to final disposal in a GDF, it is necessary to immobilise potentially mobile radioactive waste into a stable, durable form that will reduce the likelihood of radionuclide dispersion and is suitable for long term storage. Immobilisation is defined by the International Atomic Energy Agency as "conversion of a waste into a waste form by solidification, embedding, or encapsulation" [7].

Reviews of HLW immobilisation in glass and ceramic materials are provided by Donald, Metcalfe and Taylor [8] and Lee, Ojovan, Stennett and Hyatt [4]. Collectively, these reviews discuss the origins of HLW and the rationale for

immobilising HLW. The reviews also consider the materials and techniques studied internationally for immobilisation in glasses and ceramics.

1.2.1. Vitrification of HLW in Glasses

Vitrification of HLW can be described as the dissolution of waste into a glass matrix [5] and is the generally accepted solution for HLW immobilisation. Advantages of vitrification include the small volume of the final waste form, the large number of elements that can potentially be incorporated into glasses, the potentially high chemical durability of glass materials and the resistance of glasses to radioactivity [4, 8].

According to Donald et al. [8] and Lee et al. [4] borosilicate glasses are the type of glass most widely used for HLW immobilisation. Advantages of borosilicate glasses include their ability to act as a solvent for a wide range of waste elements, their mechanical and thermal stabilities, their radiation resistance and chemical durability. Their compositions can be modified which in turn allows modification of their properties. Borosilicate glasses are also widely used commercially and have been studied extensively. Examples of borosilicate glass compositions used for HLW vitrification in the UK, USA, Germany, France and Russia can be found in Lee et al. [4]. However it is known that elements such as molybdenum, chromium and sulphur have limited solubility in borosilicate glasses [4, 5].

1.2.2. Vitrification of HLW in the UK

In the UK, HLW is immobilised at the Waste Vitrification Plant (WVP) at Sellafield where HLW is vitrified using a base glass composition known as "MW" (Mixture Windscale) [9]. MW glass was originally composed of 60.61 mol % SiO_2, 18.57 mol % B_2O_3, 10.53 mol % Na_2O and 10.29 mol % Li_2O [10, 11]. However, it was later discovered that adding lithium to the HLW feed improves reactivity in the melting plant [9]. The MW glass mixture was modified so that half of the lithium content of the final waste product came from the base glass mixture and the other half from the HLW feed. This resulted in a new base glass mixture known as "MW-½Li", which is the current base glass mixture used at the Waste

Vitrification Plant. From the wt % data provided in [9] , the "MW-½Li" mixture is composed of 63.83 mol % SiO_2, 19.55 mol % B_2O_3, 11.07 mol % Na_2O and 5.55 mol % Li_2O.

1.3. Phase Separation in Vitrified HLW Containing Molybdenum

1.3.1. Phase Separation in Alkali Borosilicate Glass

Despite the broad range of elements that can be dissolved within borosilicate glasses, there are a small number of elements that have very low solubility. Molybdenum is an element that appears in HLW but is insoluble in borosilicate glasses at concentrations above 1 wt% [12], furthermore, the presence of Mo above 1 wt% can lead to the formation of separate phases during HLW glass melt cooling. [13]. Some of these phases are known as "yellow phase" due to their colour and may contain alkali molybdates, sulphates and chromates. These phases can cause enhanced corrosion of melting plant components during the glass melting stage of the vitrification process and due to their water solubility, could also reduce the chemical durability of the final solid wasteform [12, 13].

1.3.2. Future HLW Wasteforms

According to Harrison [9] a new base glass composition is currently undergoing trails at the Vitrification Test Rig (VTR) at Sellafield. This new glass composition is known as "Ca/Zn" and it is expected that this will be used as a replacement for MW glass in immobilising HLW in the UK as it encourages Mo to form insoluble $CaMoO_4$ crystal phases and prevent formation of soluble yellow phases.

1.4. Crystalline and Amorphous Solids

1.4.1. Crystalline Solids

Broadly speaking, the structure of solids can be categorised into one of two types: crystalline or amorphous. Crystalline solids (or crystals) are highly ordered solids that are formed from a periodic arrangement of their constituent atoms. A crystal

structure can be described in terms of a crystal lattice and basic building blocks called unit cells. A crystal lattice is an infinite, periodic array of points with translational symmetry. The position of any lattice point with respect to another is given by the vector:

$$\mathbf{P} = u\mathbf{a} + v\mathbf{b} + w\mathbf{c} \tag{1.1}$$

Where **a, b** and **c** are vectors known as the lattice vectors and u, v and w are positive or negative integers [14]. The parallelepiped defined by **a** , **b** and **c** is known as the unit cell. **Figure 1.1** below illustrates a simple cubic lattice with the lattice vectors shown (red) and, a position vector connecting two lattice points in (blue).

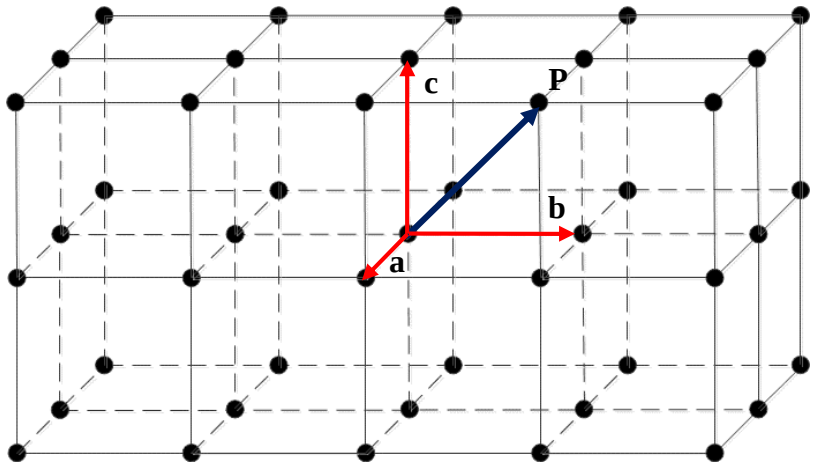

Figure 1.1: A simple cubic crystal lattice, unit cell and vector connecting two lattice points.

The unit cell can be thought of as the basic building block of a crystal structure that contains the smallest repeating arrangement of atoms in the crystal. The lengths of the unit cell sides (i.e. $a = |\mathbf{a}|$, $b = |\mathbf{b}|$ and $c = |\mathbf{c}|$) and the angles between them (α, β and γ) are collectively referred to as the unit cell parameters. **Figure 1.2** shows a unit cell for a natural sodium borosilicate ($NaBSiO_4$) crystal. Note that the unit cell shown in **Figure 1.2** is not cubic.

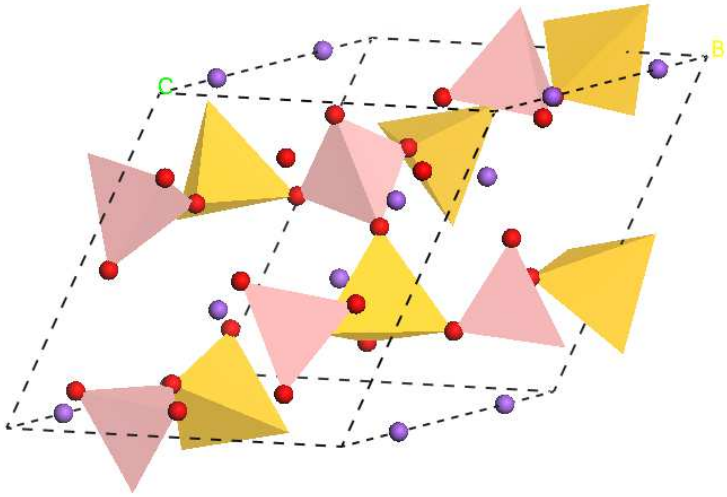

Figure 1.2: $NaBSiO_4$ unit cell with unit cell parameters $a = b = 8.035$ Å, $c = 7.703$ Å, $\alpha = \beta = 90$ ° and $\gamma = 120$ °.

1.4.2. Amorphous Solids

In contrast to crystalline solids, the structure of amorphous materials are not defined in terms of a lattice or unit cells and are therefore disordered. **Figure 1.3 (a)** shows a two-dimensional schematic of a binary compound in crystalline form and **Figure 1.3 (b)** shows a similar schematic of the same compound in an amorphous form.

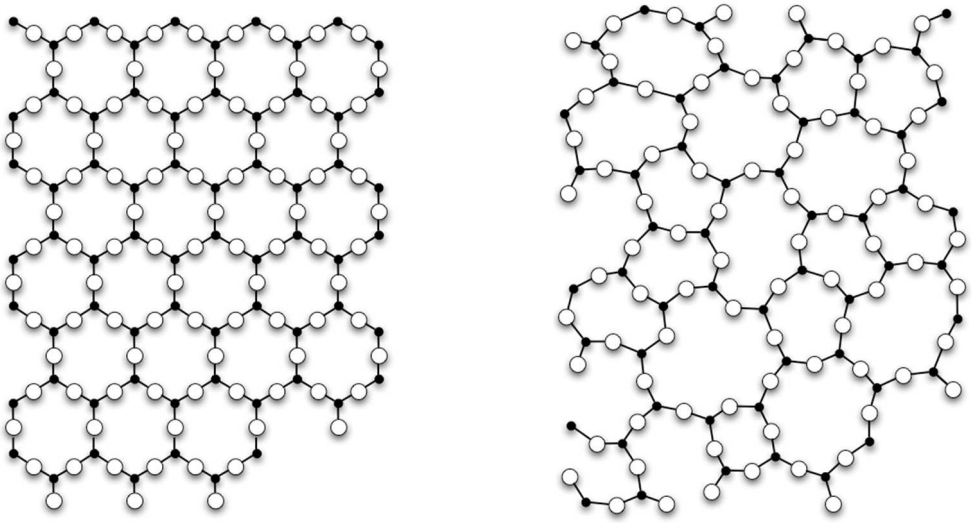

(a) **(b)**

Figure 1.3: Two-dimensional schematics of (a) a binary compound forming a crystalline structure and (b) the same compound in an amorphous structure.

1.5. Describing Glasses and Glass Structures

1.5.1. Glass Formation

If a liquid is cooled below its melting temperature, T_m, at a rate that does not allow crystallisation to occur, a supercooled liquid is formed. If a supercooled liquid is further cooled, the viscosity increases to a point where the structure of the material freezes in place and an amorphous solid (glass) is formed. **Figure 1.4** shows how the volume of a given liquid changes with temperature when it cools to form a glass and a crystalline solid.

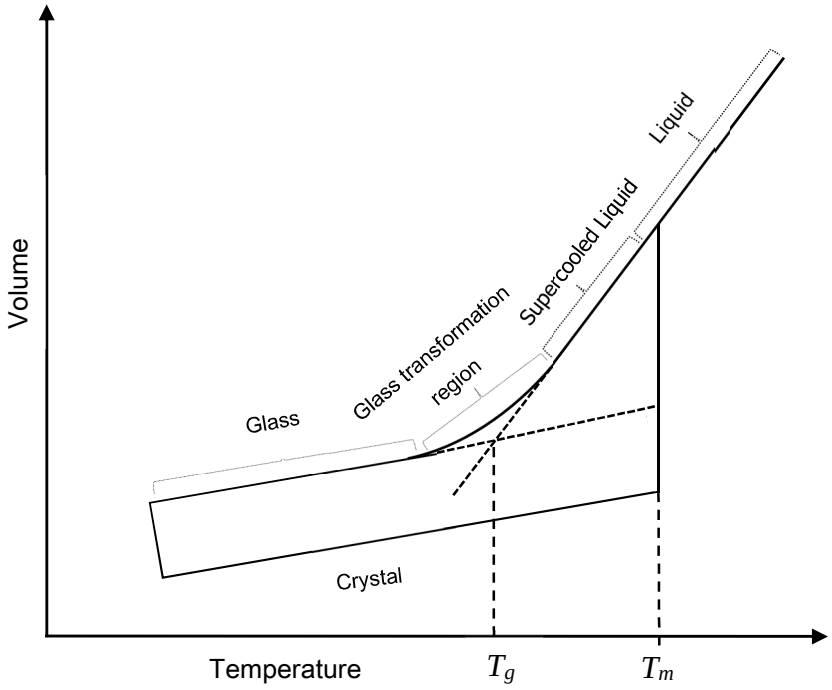

Figure 1.4: Volume versus temperature curves during glass formation and crystallisation.

Glasses are amorphous solids that lack long range periodic atomic structure and exhibit 'glass transition behaviour' [15]. Glass transition behaviour can be thought of as the reversible transition of a material from liquid to solid without the abrupt change in volume that occurs when a liquid is cooled and undergoes crystallisation. Therefore glasses more closely resemble liquids than crystalline solids. Despite their lack of long range order, glasses are generally comprised of

a network of basic structural units and are therefore considered to possess short range order.

Silica (SiO_2) provides the most common example of a compound that exists in both crystalline and amorphous forms (e.g. quartz crystals and silicate glasses). In the case of both crystalline and amorphous SiO_2, the basic structural unit is a SiO_4 tetrahedron (see **Figure 1.5 (a)** and **(b)**). In the crystalline form, the SiO_4 tetrahedra are arranged uniformly throughout the structure whereas in the amorphous (glass) form, the tetrahedra are randomly orientated with respect to each other.

(a) **(b)**

Figure 1.5: (a) "ball and stick" and (b) polyhedral representations of SiO_4 tetrahedra. Gold regions represent silicon atoms and red spheres represent oxygen atoms.

1.5.2. Glass Forming Materials

In theory, any liquid can form a glass if cooled at a high enough rate however there are some materials that form glasses much more easily than others. According to Paul [16], the only elements that can form glasses are phosphorus, sulphur, selenium and tellurium. Materials that readily form glasses are known as 'glass formers'. Examples of glass formers include B_2O_3, SiO_2, GeO_2 and P_2O_5. These oxides form random networks of interconnected tetrahedral and/or triangular building blocks. In 1932 Zachariasen [17] suggested a set of empirical rules that must be satisfied for an oxide (A_xO_y) to be considered a good glass former: (1) no oxygen atom may be linked to more than two network cations of species A, (2) the number of oxygen atoms surrounding each cation A must be

small (around 3 or 4), (3) polyhedral units share corners only (i.e. not corners of faces) and (4) at least three corners of each polyhedron must be shared to create a three-dimensional network.

Elements added to a glass that form highly ionic bonds with oxygen do not take part in network formation and are known as 'network modifiers' (or 'modifiers'). Such elements break up the network by forming non-bridging oxygens (NBOs) as shown in **Figure 1.6**.

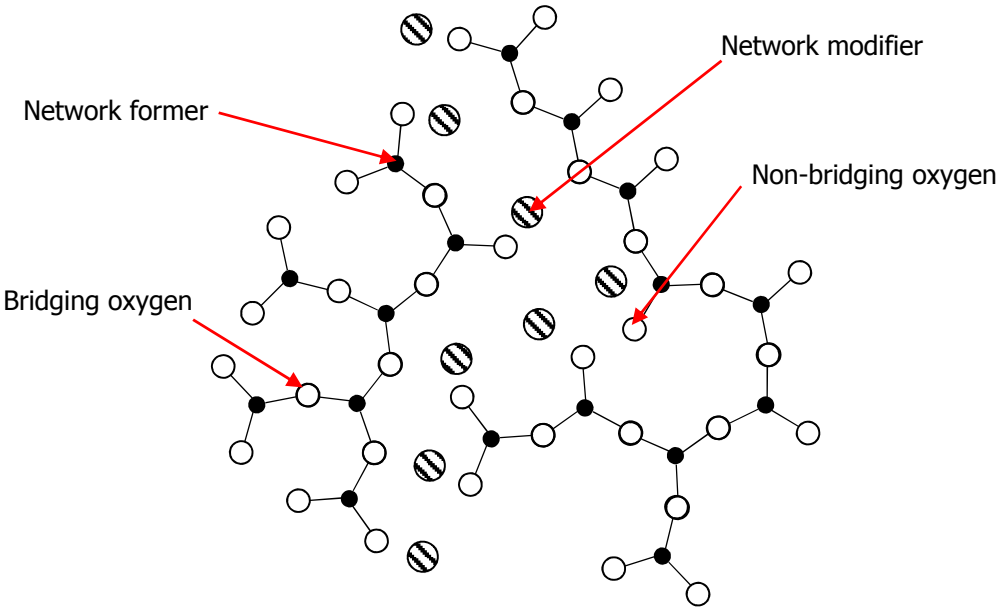

Figure 1.6: Schematic of the effect of network modifiers. Each network modifier in this schematic creates one NBO.

As well as network formers and modifiers, there are certain substances that do not form networks readily themselves but may take part in network formation if mixed with network formers (e.g. Al_2O_3 may take part in network formation in silicate glasses). Such materials are referred to as intermediates.

1.5.3. Radial Distribution Function

Radial distribution functions (RDFs) provide information on the average distances between atoms and are useful for describing the structure of amorphous materials. RDFs can be derived from computer simulations (e.g. Monte Carlo or Molecular Dynamics) and from experimental methods such as neutron or X-ray diffraction. RDFs are therefore useful for comparing experimental data with computer simulations. A partial pair RDF $g_{ij}(r)$, describes the average distance between a chosen atom of species i and all other atoms of species j in a spherical shell of thickness r and $r + dr$ and is given by **Equation (1.2)** below:

$$g_{ij}(r) = 4\pi r^2 \rho_j(r) \qquad \textbf{(1.2)}$$

Where $\rho_j(r)$ is the radial density distribution for atomic species j which is equal to zero at distances less than the nearest neighbour distance and tends to the average density of atom type j ρ_j at large distances.

Partial pair RDFs shall herein be referred to as RDFs. RDFs have been used in this work to determine the average nearest neighbour distances between cations (X) and neighbouring oxygen atoms (O). The average nearest neighbour distances $<d_{X\text{-}O}>$ have been calculated using **Equation (1.3)** below:

$$< d_{X-O} >= \frac{\sum g_{ij}(r) \cdot r}{\sum g_{ij}(r)} \qquad \textbf{(1.3)}$$

Note that the calculation of $<d_{X\text{-}O}>$ only includes values of $g_{ij}(r)$ between $r = 0$ and the first minimum immediately after the first maximum in the RDF (as illustrated in **Figure 1.7** below). The first maximum in the RDF represents the mode X-O distance. Standard deviations in from the average nearest neighbour distances were calculated using **Equation (1.4).**

$$\sigma = \sqrt{\frac{\sum (r - < d_{X-O} >)^2 \cdot g_{ij}(r)}{\sum g_{ij}(r)}} \qquad \textbf{(1.4)}$$

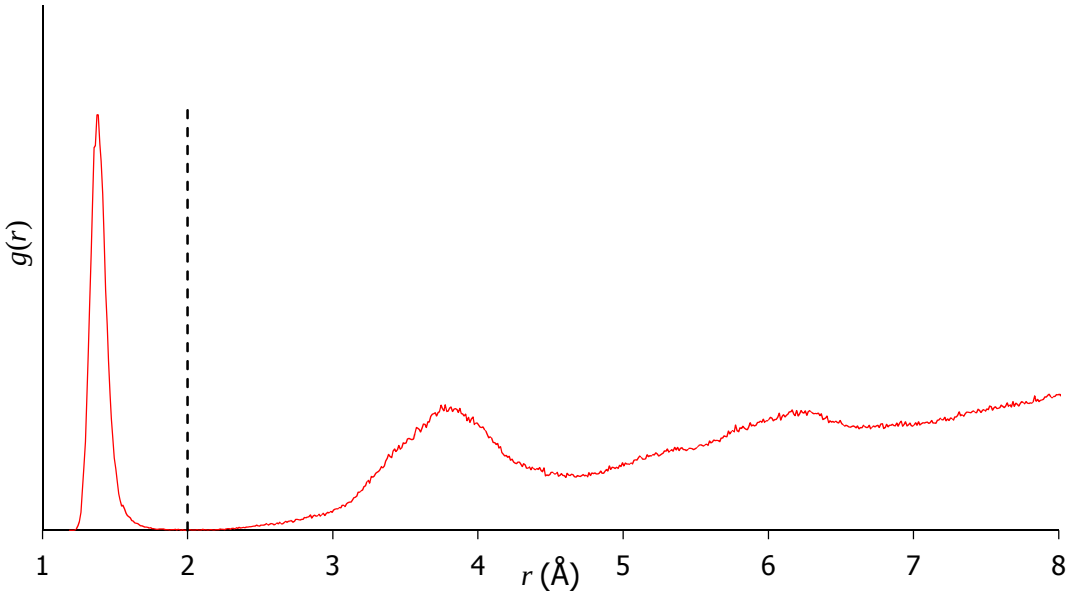

Figure 1.7: Example radial distribution function for Si-O in a silicate glass. The dashed line shows the cut off for the calculation of the average nearest neighbours distance.

1.5.4. Coordination Numbers

The coordination number of one atom type to another provides insight into the arrangement of atoms in a material. The coordination number can be thought of as the number of nearest neighbours of atom type j surrounding atom type i. For example, it is possible for boron to three- and four-coordinate with oxygen as illustrated in **Figure 1.8**.

(a) **(b)**

Figure 1.8: Visual representations of: (a) three-coordinated boron and (b) four-coordinated boron.

The coordination number of atomic species j surrounding an atom of species i, $CN_{ij}(r)$, is found by integrating the RDF from atom i to radial distance r=R as per **Equation (1.5)**:

$$CN_{ij}(r) = \int_{r=0}^{R} g_{ij}(r)dr = \int_{r=0}^{R} 4\pi r^2 \rho_j(r)dr \qquad \textbf{(1.5)}$$

1.5.5. Bond Angle Distributions

Bond angle distributions (BADs) show the range of bond angles present for a particular atomic triplet i, j and k (see **Figure 1.9** below). BADs along with RDFs and coordination numbers, provide insight into the arrangement of atoms in a material.

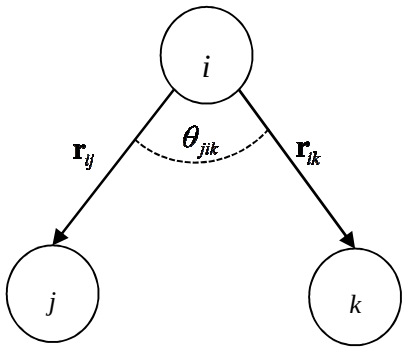

Figure 1.9: Diagram of an atomic triplet *i*, *j* and *k*.

1.5.6. Network Connectivity

Another important feature in the description of glass structures is the connectivity of the network. The network connectivity can be expressed in terms of 'Q^n' units which describe the number of bridging oxygen atoms for a given polyhedral unit. For example, the polyhedron labelled 'A' in **Figure 1.10** is a Q^4 silicate polyhedron which is connected to four other polyhedra via the oxygen atoms at its vertices. Since all the oxygen atoms associated with polyhedron 'A' are connected to other polyhedra, polyhedron A is a Q^4 unit and has no NBOs. The polyhedron labelled 'B' in **Figure 1.10** is a Q^3 unit and has one NBO, the polyhedron labelled C is a Q^2 unit and has two NBOs.

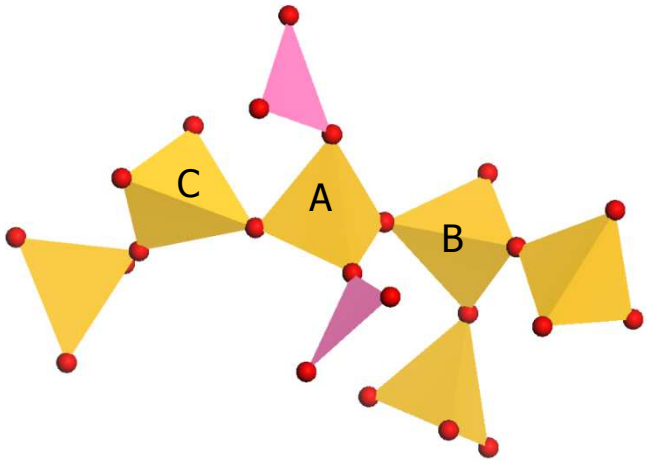

Figure 1.10: Diagram illustrating Q^n notation. Gold tetrahedra are silicon atoms, pink triangles are boron atoms and red spheres are oxygen atoms.

1.6. Chapter 1 References

[1] Department for Energy and Climate Change, "Digest of United Kingdom Energy Sources," The Stationery Office, London, 2014.

[2] The Royal Society, "Fuel Cycle Stewardship in a Nuclear Renaissance," The Royal Society, London, 2011.

[3] L. B. Silverio and W. d. Q. Lamas, "An analysis of development and research in spent nuclear fuel reprocessing," *Energy Policy,* vol. 39, pp. 281-289, 2011.

[4] W. H. Lee, M. I. Ojovan, M. C. Stennett and N. C. Hyatt, "Immobilisation of radioactive waste in glasses, glass composite materials and ceramics," *Adv. Appl. Ceram.,* vol. 105, no. 1, pp. 3-32, 2006.

[5] G. Roth and S. Weisenburger, "Vitrification of high level liquid waste: glass chemistry, process chemistry and process technology," *Nucl. Eng. Des.,* vol. 202, pp. 197-207, 2000.

[6] Department of Energy and Climate Change, "Implementing geological disposal: A framework for the long-term management of higher activity radioactive waste," 08 July 2014. [Online]. Available: https://www.gov.uk/government/uploads/system/uploads/attachment_data/file/332890/GDF_White_Paper_FINAL.pdf. [Accessed August 2014].

[7] International Atomic Energy Agency, "www-pub.iaea.org," 2003. [Online]. Available: www-pub.iaea.org/MTCD/publications/PDF/Pub1155_web.pdf. [Accessed 7 August 2014].

[8] I. W. Donald, B. L. Metcalfe and R. N. J. Taylor, "The immobilization of high level radioactive wastes using ceramics and glasses," *J. Mater. Sci.,* vol. 32, pp. 5851-87, 1997.

[9] M. T. Harrison, "Vitrification of High Level Waste in the UK," *Procedia Materials Science,* vol. 7, pp. 10-15, 2014.

[10] D. Holland, B. G. Parkinson, M. M. Islam, A. Duddridge, J. M. Roderick, A. P. Howes and C. R. Scales, "NMR insights into wasteforms for the vitrification of high-level nuclear waste," *Appl. Magn. Reson.,* vol. 32, pp. 483-497, 2007.

[11] B. G. Parkinson, D. Holland, M. E. Smith, A. P. Howes and C. R. Scales, "The effect of Cs2O additions on HLW wasteform glasses," *J. Non-Cryst. Solids.,* vol. 32, pp. 483-497, 2007.

[12] G. Calas, M. Le Grand, L. Galoisy and D. Ghaleb, "Structural role of molybdenum in nuclear glasses: an EXAFS study," *J. Nucl. Mater.,* vol. 322, no. 1, pp. 15-20, 2003.

[13] R. J. Short, R. J. Hand, N. C. Hyatt and G. Möbus, "Environment and oxidation state of molybdenum in simulated high level waste glass compositions," *J. Nucl. Mater.,* vol. 340, pp. 179-186, (2005).

[14] R. J. D. Tilley, Understanding Solids: The Science of Materials, Chichester: John Wiley and Sons Ltd, 2013.

[15] J. E. Shelby, An Introduction to Glass Science and Technology, 2nd ed., Cambridge: The Royal Society of Chemistry, 2005.

[16] A. Paul, Chemistry of Glasses, London: Chapman and Hall, 1990.

[17] W. H. Zachariasen, "The atomic arrangement in glass,," *J. Am. Chem. Soc.,* vol. 54, no. 10, pp. 3841-3851, 1932.

2. Methods and Theory

2.1. Molecular Dynamics Simulation

2.1.1. Introduction to Molecular Dynamics

Classical molecular dynamics (MD) simulations are widely used in the study of glass structures [1]. In such simulations, classical physics is employed to compute velocities and positions of atoms by integrating Newton's second law of motion [2].

$$\mathbf{F}(t) = m\mathbf{a}(t) = m\frac{d^2}{dt^2}\mathbf{r}(t) \qquad \textbf{(2.1)}$$

The use of classical mechanics allows systems containing large numbers of atoms to be studied that would otherwise be extremely time consuming to model using quantum mechanics.

A MD simulation consists of a 'box' containing N atoms. The positions and velocities of the atoms in the box are determined by solving **Equation (2.1)** for each atom. This process is repeated until the properties of the system remain constant, (i.e. until the system reaches equilibrium). Once equilibrium has been achieved, the system may be analysed and structural properties may be determined.

2.1.2 Molecular Dynamics Method

In order to solve **Equation (2.1)**, the force on each particle must be computed. In MD simulations the forces are specified in the form of potential energy functions $U(\mathbf{r(t)})$. The force is related to the potential by **Equation (2.2)**:

$$\mathbf{F}(\mathbf{r}(t)) = -\nabla U(\mathbf{r}(t)) \qquad \textbf{(2.2)}$$

Verlet algorithm

Equation (2.1) is integrated using Verlet's algorithm [3] which uses the Taylor expansion to define the position of a particle at times $t \pm \delta t$ as shown in **Equations (2.3)** and **(2.4)** below:

$$\mathbf{r}(t+\delta t) = \mathbf{r}(t) + \frac{d}{dt}\mathbf{r}(t)\delta t + \frac{1}{2}\frac{d^2}{dt^2}\mathbf{r}(t)\delta t^2 + \frac{1}{6}\frac{d^3}{dt^3}\mathbf{r}(t)\delta t^3 + O\delta t^4 \qquad \textbf{(2.3)}$$

$$\mathbf{r}(t-\delta t) = \mathbf{r}(t) - \frac{d}{dt}\mathbf{r}(t)\delta t + \frac{1}{2}\frac{d^2}{dt^2}\mathbf{r}(t)\delta t^2 - \frac{1}{6}\frac{d^3}{dt^3}\mathbf{r}(t)\delta t^3 + O\delta t^4 \qquad \textbf{(2.4)}$$

where O is the fourth order term of the expansion and δt is the time-step used in the MD simulation.

Combining **Equations (2.3)** and **(2.4)** gives:

$$\mathbf{r}(t+\delta t) \approx 2\mathbf{r}(t) - \mathbf{r}(t-\delta t) + \frac{d^2}{dt^2}\mathbf{r}(t)\delta t^2 + O\delta t^4 \qquad \textbf{(2.5)}$$

Equation (2.5) shows how the position of a particle at time $t + \delta t$ can be estimated in terms of the particle's acceleration at time t and its position at times t and $t - \delta t$. Note that **Equation (2.5)** contains an error proportional to δt^4.

Verlet Leapfrog Algorithm

Note that **Equation (2.5)** does not include a term for the velocity of the particles which is required for the determination of certain properties of the system such as kinetic energy. The velocities are therefore determined using the Verlet Leapfrog algorithm which estimates the particle velocities at half-time step intervals as described below.

$$\mathbf{v}\left(t + \frac{\delta t}{2}\right) = \frac{\mathbf{r}(t+\delta t) - \mathbf{r}(t)}{\delta t} \qquad \textbf{(2.6)}$$

Rearranging for the position at time $t + \delta t$ gives:

$$\mathbf{r}(t+\delta t) = \mathbf{r}(t) + \mathbf{v}\left(t + \frac{\delta t}{2}\right)\delta t \qquad \textbf{(2.7)}$$

From mean value theorem the acceleration at time t can be defined as:

$$\mathbf{a}(t) = \frac{\mathbf{v}\left(t + \frac{\delta t}{2}\right) - \mathbf{v}\left(t - \frac{\delta t}{2}\right)}{\delta t} = \frac{\mathbf{F}(\mathbf{r}(t))}{m} \qquad \textbf{(2.8)}$$

The velocity at time $\mathbf{v}(t+\delta t/2)$ can therefore be written in terms of the force $\mathbf{F}(t)$:

$$\mathbf{v}\left(t + \frac{\delta t}{2}\right) = \mathbf{v}\left(t - \frac{\delta t}{2}\right) + \frac{\mathbf{F}(\mathbf{r}(t))}{m}\delta t \qquad \textbf{(2.9)}$$

Substituting **Equation (2.9)** into **Equation (2.7)** allows the position of the particles at time $t + \delta t$ to be calculated:

$$\mathbf{r}(t+\delta t) = \mathbf{r}(t) + \left[\mathbf{v}\left(t - \frac{\delta t}{2}\right) + \frac{\mathbf{F}(\mathbf{r}(t))}{m}\delta t\right]\delta t \qquad \textbf{(2.10)}$$

Kinetic Energy and Temperature Calculations

A disadvantage of using the Verlet Leapfrog algorithm is that positions and particles are computed out of sync with each other. This is undesirable where physical properties that depend on both position and velocity of the particles must be known simultaneously. **Equation (2.11)** below is used to estimate the velocity at time t.

$$\mathbf{v}(t) = \frac{\mathbf{v}\left(t + \frac{\delta t}{2}\right) + \mathbf{v}\left(t - \frac{\delta t}{2}\right)}{2} \qquad \textbf{(2.11)}$$

The temperature of the entire system at time t is related to the kinetic energy of each particle as shown in **Equation (2.12)**:

$$\sum_{i=1}^{N} m_i v_i^{\,2}(t) = \frac{N_f}{2} k_B T \qquad \textbf{(2.12)}$$

where k_B is the Boltzmann constant and N_f is the number of degrees of freedom.

2.1.3 Force Field

In this study, classical MD was utilised to simulate structures of glasses by treating the atoms that comprise the glass as rigid ions interacting via long-range electrostatic and short-range forces. The total potential associated with the system is:

$$U_T = \sum_{j=1}^{N} U_E + \sum_{j=1}^{N} U_S \qquad \textbf{(2.13)}$$

where U_E and U_s are the long range (electrostatic) and short range potential energy functions between constituent atoms respectively.

Long Range Electrostatic Interaction

Consider two charged particles, atom i with charge q_i and atom j with charge q_j separated by a vector $\mathbf{r}_{ij}$. According to classical electromagnetism, the potential energy of this system is:

$$U_E(r_{ij}) = \frac{e^2 q_i q_j}{4\pi\varepsilon_0 r_{ij}} \qquad \textbf{(2.14)}$$

where ε_0 is the permittivity of free space, e is the charge on an electron and $r_{ij} = |\mathbf{r}_{ij}|$.

The electrostatic interaction acts over an infinite range however, for the purposes of efficient MD simulations, its range will be restricted.

Short Range Interactions

In addition there are also short range interactions which must be considered. The short range interactions include a repulsive force that occurs when electron clouds overlap (a manifestation of the Pauli Exclusion Principle), and an attractive term that occurs due to induced dipole moments (or Van der Waals interactions). These short range interactions are normally specified via empirical potential energy functions.

Two-body Potentials

Two-body potentials are short range potential energy functions specified in terms of the distance between two particles. In this work, the Buckingham and Born-Huggins-Mayer (BHM) potentials will be used which are shown below in **Equations (2.15)** and **(2.16)** respectively:

$$U_{Buck}(r_{ij}) = A\exp\left(\frac{-\rho}{r_{ij}}\right) - \frac{C}{r_{ij}^{6}} \qquad \textbf{(2.15)}$$

$$U_{BHM}(r_{ij}) = A\exp\left[B(\sigma - r_{ij})\right] - \frac{C}{r_{ij}^{6}} - \frac{D}{r_{ij}^{8}} \qquad \textbf{(2.16)}$$

Three-body Potentials

In addition to two-body potentials, it is often beneficial to specify three-body potentials that constrain the angle θ_{jik} made between a central particle i interacting with (at least) two other neighbouring particles j and k (see **Figure 1.9** in **Chapter 1**). Constraining bond angles can influence coordination numbers.

In this work the screened harmonic three-body potential was used. The functional form of this potential is shown in **Equation (2.17)**.

$$U_{jik}(r_{ij}, r_{ik}, \theta_{jik}) = \frac{k}{2}(\theta_{jik} - \theta_0)^2 \exp\left[-\left(r_{ij}/\rho_1 + r_{ik}/\rho_2\right)\right] \qquad \textbf{(2.17)}$$

2.1.4 Evaluation of Interatomic Potential Functions

Before attempting to make MD simulations of glasses it was necessary to validate the potential functions and parameters describing the short range forces between constituent atoms in the glasses. This was carried out using the General Utility Lattice Program (GULP) [4].

The GULP package can be used to carry out energy minimisation calculations on an initial arrangement of particles that interact via user specified potential functions. In this work, the initial particle arrangements were based on the unit

cells of crystal structures containing atomic species found in the glasses of interest to this work. All crystallographic information was obtained from the Inorganic Crystal Structure Database (ICSD) [5].

The GULP program uses the Newton-Raphson method to compute the minimum energy starting from an input crystal structure. The energy minimisation process results in changes to the unit cell parameters and positions of the atoms in the crystal. The altered atomic positions subsequently cause changes to bond lengths and bond angles. When there is good agreement between the initial and final values, the interatomic potential parameters are considered suitable.

2.2 Helium Pycnometry

2.2.1 Introduction to Pycnometry

Pycnometry is a technique used to determine the volume of irregularly shaped solids. Determination of the volume combined with measurement of the mass allows the density of the solid to be calculated. In a pycnometer, helium gas is allowed to enter a chamber of fixed volume known as the reference cell. A valve is then opened and the gas expands into a chamber containing a sample known as the sample cell. If the gas pressures before and after expansion are known, the ideal gas law (**Equation (2.18)**) can be used to determine the volume of the sample.

$$PV = NRT \qquad \textbf{(2.18)}$$

Where P is pressure, V is volume, N = number of molecules, R is the molar gas constant and T is temperature.

Figure 2.1 below shows a schematic of the chambers inside a gas pycnometer.

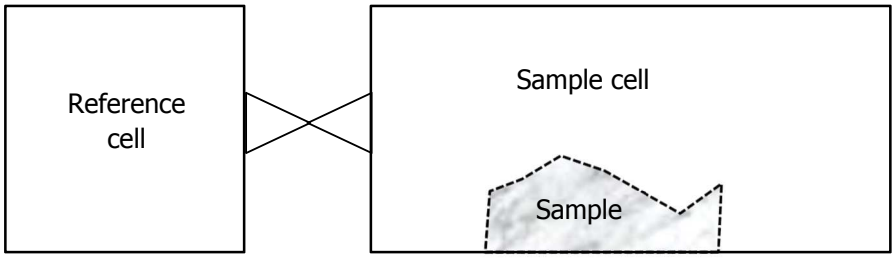

Figure 2.1: Schematic of a helium pycnometer.

If no gas is lost and the temperature remains constant throughout the experiment (i.e. N and T remain constant) the product of pressure and volume before and after expansion will be equal i.e.:

$$P_1V_1 = P_2V_2 = \text{constant} \qquad \textbf{(2.19)}$$

Where P_1 and V_1 are the respective pressures and volumes of the gas in the reference cell prior to expansion and P_2 and V_2 are the pressures and volumes of the gas in the reference and sample cells after expansion.

Let V_R, V_C and V_S be the volumes of the reference cell, samples cell and sample respectively.

When the reference cell is filled with gas prior to expansion we can write:

$$V_1 = V_R \qquad \textbf{(2.20)}$$

When the valve isolating the reference and sample cells is opened, the gas expands to occupy both the reference and sample cells. Since the sample occupies volume V_S, the volume occupied by the gas after expansion, V_2 is given by:

$$V_2 = V_R + V_C - V_S \qquad \textbf{(2.21)}$$

Substituting **Equation (2.21)** into **Equation (2.19)** gives:

$$P_1V_R = P_2(V_R + V_C - V_S) \qquad \textbf{(2.22)}$$

Rearranging for V_S gives:

$$V_S = V_C + V_R - \frac{P_1 V_R}{P_2} \quad \textbf{(2.23)}$$

Which can also be written as:

$$V_S = V_C - V_R\left(\frac{P_1}{P_2} - 1\right) \quad \textbf{(2.24)}$$

By measuring P_1 and P_2 directly from the digital manometer on the pycnometer, **Equation (2.24)** can be used with known values of V_C and V_R to determine the volume of the sample.

2.2.2 Helium Pycnometry Method

Samples were placed into the sample cell of a Quantachrome Instruments Multipycnometer (see **Figure 2.2**) which was then sealed. The sample and reference cells were purged with Helium gas for at least ten minutes. After purging, the cells were evacuated and the valve separating the reference and sample cells was closed. Helium gas was then introduced into the reference cell until the pressure reached approximately 17 psi, at which point, the gas inlet valve was closed and the pressure recorded as P_1. The valve separating the reference and sample cells was then opened allowing the gas to occupy both cells. At this point the pressure P_2 was noted. Using calibration values for the volumes of the reference cell V_R and sample cell V_C, **Equation (2.24)** was used to determine the volume of the sample.

The system was evacuated and the reference volume was once again pressurised to repeat the process. This procedure was repeated at least ten times for each sample.

Figure 2.2: Photograph of a Quantachrome Instruments Multipycnometer.

2.3 X-ray Fluorescence Spectroscopy

2.3.1 Introduction to X-ray Fluorescence

X-ray fluorescence (XRF) is a technique used to determine the elemental composition of a material. In XRF, a beam of high energy X-rays is directed onto a sample. Some of these incident X-rays will exchange energy with inner-shell electrons of atoms in the sample. This causes some inner-shell electrons to be ejected and leaves the atom in an excited state. Eventually, an electron in a higher energy shell will decay to fill the vacancy, releasing energy in the form of a fluorescent X-ray photon. **Figure 2.3** provides a schematic of the process.

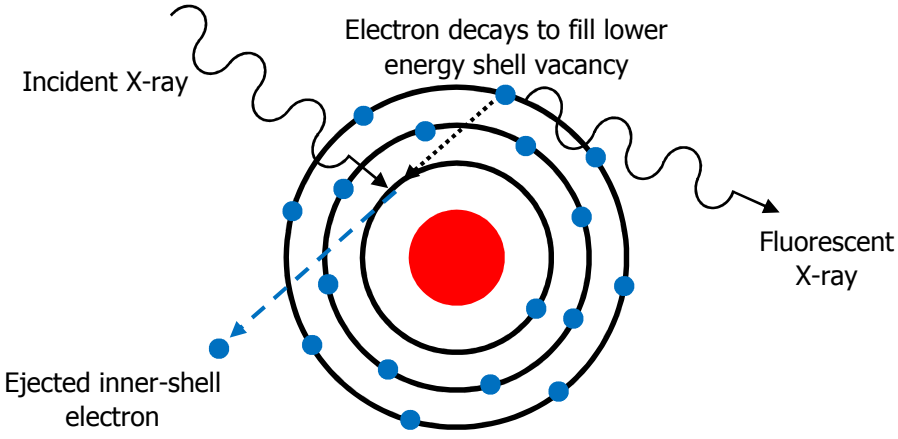

Figure 2.3: Schematic of the XRF emission process.

If an electron decays from an energy level E_1 to a lower energy level E_2 the energy of the emitted X-ray is given by:

$$E_1 - E_2 = h\nu \qquad \textbf{(2.25)}$$

where ν is the frequency of the X-ray and h is Planck's constant.

Since the difference in energy between electron shells are unique for each element, so too are the energies of the emitted X-rays. The detection of such X-rays therefore allow compositional data to be obtained from a sample.

2.3.2 X-ray Fluorescence Experimental Setup

All XRF measurements reported in this work were obtained using a PANalytical Epsilon 3 Energy Dispersive XRF spectrometer (see **Figure 2.4** below). Powdered samples of glass were loaded into plastic sample holders with a 3.6 μm mylar window. The powdered samples were loaded into the holders so that they formed a layer approximately 1 mm thick above the mylar window. The processing software was configured to report the spectrum in terms of percent oxide concentration.

Figure 2.4: Photograph of a PANalytical Epsilon 3 XRF spectrometer.

2.4 Scanning Electron Microscopy

2.4.1 Introduction to Electron Microscopy

In optical microscopy, visible light scattered off an object is refracted and focussed by a series of lenses to create a magnified image of the object. In an electron microscope, a sample is irradiated by a beam of electrons which interact with the sample and are detected to form an image. In an optical system light is refracted and focussed by lenses made of a transparent medium (i.e. glass). In an electron microscope, electrons are deflected and focussed by magnetic fields.

In theory, the image of an object produced by an optical system can be magnified by an infinite amount however, due to diffraction effects, the details that can be resolved are limited by the wavelength of the light scattered off the object. The resolving power of the system is inversely proportional to the wavelength, therefore a using a lower wavelength will result in a higher resolving power. According to quantum theory electrons exhibit wave-particle duality. The wavelength λ of a particle is given by:

$$\lambda = \frac{h}{p} \qquad \textbf{(2.26)}$$

where h is Planck's constant and p is momentum of the particle.

According to **Equation (2.26)**, particles with high kinetic energy are able to resolve finer details than particles with lower kinetic energy since their wavelengths are shorter. The wavelength of visible light ranges between 400-700 nm; from **Equation (2.26)** a 20 keV electron will have a wavelength of approximately 9×10^{-3} nm. Electron microscopes are therefore able to resolve much finer details than optical microscopes.

2.4.2 The Scanning Electron Microscope

In a scanning electron microscope (SEM) a beam of high energy electrons (known as the primary beam) is scanned across a target area of a sample. The electrons

in the primary beam (known as primary electrons) interact with the sample resulting in the ejection of electrons from the sample's surface which can be detected. The process is then repeated until, row by row, the full image has been produced. A schematic of a scanning electron microscope is provided in **Figure 2.5** below.

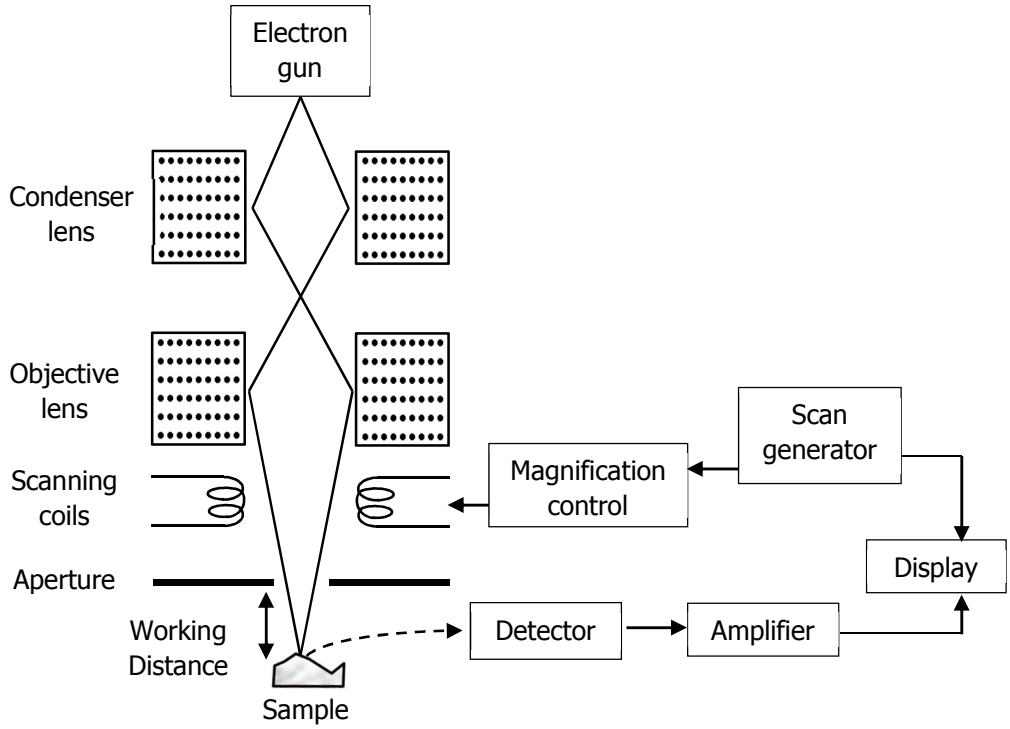

Figure 2.5: Schematic of diagram of an SEM adapted from [6] and [7].

2.4.3 Interactions between Electrons and Matter

Electrons may interact with atoms in matter by elastic or inelastic scattering events. Elastic scattering of electrons occurs when electrons enter a material and are scattered back out via electrostatic interactions with constituent atoms whilst suffering negligible kinetic energy loss. Electrons that are scattered out of a material in such a way are known as backscattered electrons. Since the scattering power of atoms depends on their atomic number, backscattered electrons are useful for distinguishing different elements or providing compositional images.

Inelastic scattering of electrons entering material may occur in a number of ways including: plasmon scattering, phonon scattering, secondary electron emission, inner-shell electron ejection, bremsstrahlung and cathodoluminescence. For obtaining further composition information, the fluorescent x-rays from inner-shell electron ejection can be analysed using EDX (or EDS), i.e. energy dispersive x-ray spectroscopy. For imaging purposes, the most important of these inelastic scattering interactions are the emission of secondary electrons.

Secondary electrons are emitted when a high energy incident electron strikes a valence electron in an atom causing it to be ejected. If the ejected electron is sufficiently close to the surface of the sample and has enough kinetic energy to overcome the work function of the material, then it may escape from the material's surface and be detected. According to Goodhew et al. [6] and Goldstein et al. [7], electrons that emerge from the sample with energies less than 50 eV are considered to be secondary electrons. Furthermore, Goodhew et al. [6] indicate that it is possible for the number of emitted secondary electrons to be greater than the number of incident electrons and therefore appear in abundance. However, despite their high abundance, secondary electrons only emerge from a relatively small volume within the sample (see **Figure 2.6** below). Secondary electron images are therefore useful for topographic or surface imaging.

2.4.4 Interaction Volume

The volume of the sample that primary electrons can penetrate is known as the interaction volume. Within the interaction volume, there are sub regions from which different signals can emerge. **Figure 2.6** below shows schematically the relative depths at which secondary electrons, backscattered electrons and X-rays emerge from. The size of the interaction volume (and therefore the size of the various regions), is dependent on the energy of the primary electrons and the atomic number of the elements in the sample. The greater the energy of the primary electron beam, the further the primary electrons will penetrate the sample. However the greater the atomic number of the target atoms, the greater

the number of scattering interactions that will prevent electrons penetrating further into the sample.

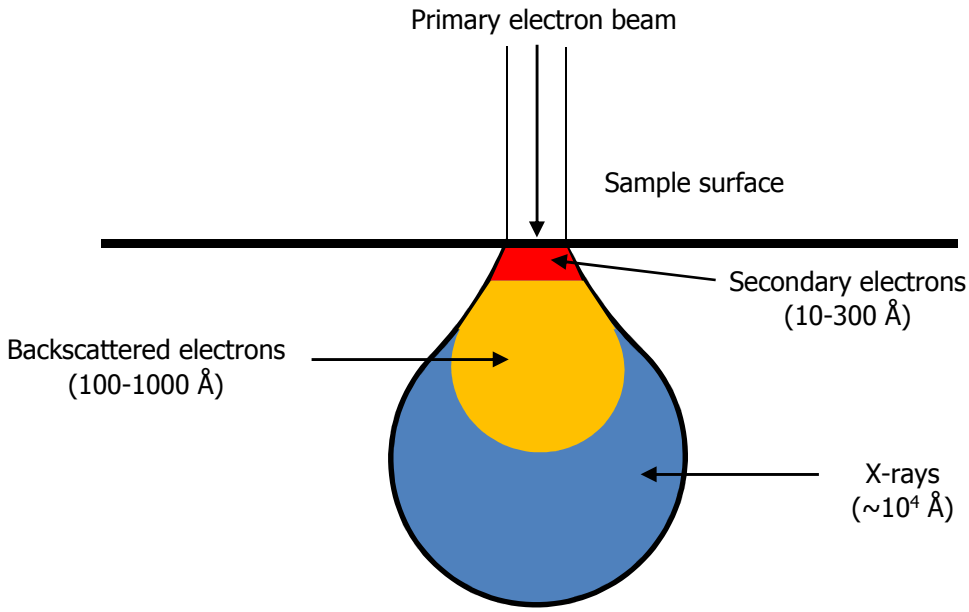

Figure 2.6: Schematic of the interaction volume from which secondary electrons, backscattered electrons and X-rays emerging from a sample may be detected.

2.4.5 Chemical Analysis with Energy Dispersive X-ray (EDX) Spectroscopy

As well as causing secondary and backscattered electrons to emerge from a sample, primary electrons entering a sample may also cause X-rays to be emitted. There are two types of X-ray emitted: characteristic X-rays and continuum X-rays. Characteristic X-rays are produced when a high energy electron causes ejection of an inner-shell electron, leaving it in a higher energy state, as described in **Section 2.3**. Since the differences in energy between electron shells are unique to each element, so too are the emitted X-rays. Such X-rays therefore allow compositional data from a sample to be obtained.

Continuum (or bremsstrahlung) X-rays have a continuous range of energies and are not characteristic of atoms in the sample.

2.4.6 SEM and EDX Experimental Setup

Backscattered electron (BSE) and secondary electron (SE) images were collected for the simulated vitrified waste forms described in **Section 4.1.2**. All images were taken on a Hitachi S-3400N Variable Pressure Scanning Electron Microscope (see **Figure 2.7**) with a (target) working distance of 10 mm and an accelerating voltage of 20 keV. Since the samples studied in this work were non-conducting, many of the SEM images presented in this work were made with the sample chamber at a pressure ~25 Pa in order to reduce charge accumulation on the samples and subsequent image distortion.

Energy Dispersive X-ray (EDX) spectra from the simulated vitrified waste samples described in **Section 4.1.2** were obtained using an Oxford Instruments X-max 80 mm^2 silicon drift detector. EDX spectral data was collected by generating an SEM image and then selecting a target region on image to collect data from. This allows EDX spectra to be obtained from a small region in the sample. The chemical composition data obtained from the instrument was analysed using the INCA software package also provided by Oxford Instruments. EDX data was obtained from the glass and crystalline phases (where applicable) for all samples studied in this work. The INCA software package returned the results in terms of oxide per cent composition.

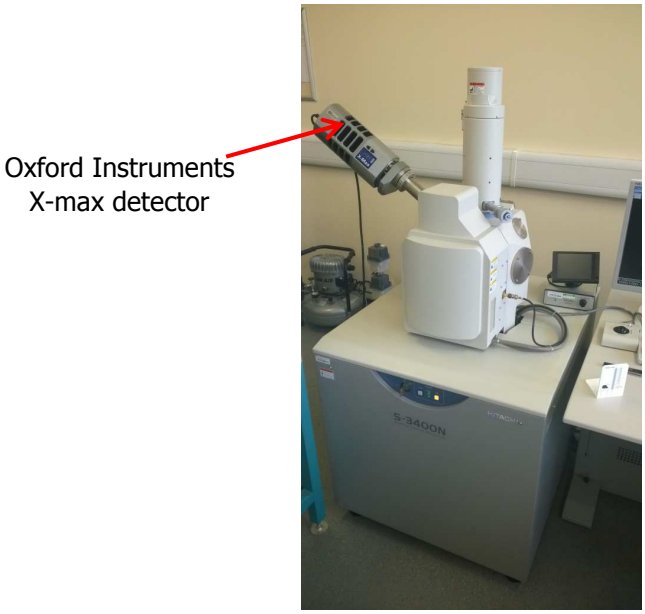

Figure 2.7: Photograph of an Hitachi S-3400N Variable Pressure Scanning Electron Microscope with mounted Oxford Instruments X-max detector.

2.5 Raman Spectroscopy

Raman spectroscopy is a molecular characterisation technique that provides information about the chemical bonds present in a material. The technique is so named because of its use of the Raman scattering phenomenon which was discovered by Sir C. V. Raman in 1928 [8].

When electromagnetic (EM) radiation is incident on matter, a number of interaction phenomena may occur including absorption, scattering and transmission [8]. In Rayleigh scattering, light incident upon matter is scattered elastically at the same frequency at which it arrived.

In addition to Rayleigh scattering, a very small proportion of light incident may be scattered at frequencies different to the incident light. Since the energy of a photon E (or "packet" of EM radiation) is related to its frequency by:

$$E = h\nu \tag{2.27}$$

When there is a change in the photon's frequency, an exchange of energy between the photon and the matter has taken place - this is known as inelastic

scattering. In Raman scattering, energy exchanges are due to molecular vibrations and rotations. Since the work presented in this dissertation only involves the study of solids, only vibrations will be considered henceforth.

2.5.1 Molecular Vibration

A vibrating diatomic molecule may be modelled as two masses (m_1 and m_2) connected by a spring as shown in **Figure 2.8** below. An analysis of the mechanics of such a model is provided by Ferraro et al. [9] and is presented below.

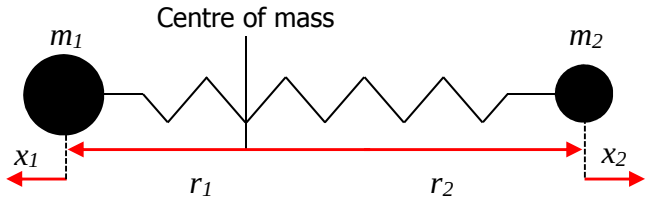

Figure 2.8: Schematic of a linear diatomic molecule modelled as two (unequal) masses connected by a spring.

If the displacement of m_1 and m_2 are x_1 and x_2 respectively the centre of mass condition requires that:

$$m_1(r_1 + x_1) = m_2(r_2 + x_2) \qquad \textbf{(2.28)}$$

According to Hooke's law, the force exerted on the masses by the spring following displacement is given by:

$$F = -k(x_1 + x_2) \qquad \textbf{(2.29)}$$

Where k is the spring constant.

Equations (2.28) and **(2.29)** allow us to write:

$$F = -k\left(\frac{m_1 + m_2}{m_1}\right)x_2 = -k\left(\frac{m_1 + m_2}{m_2}\right)x_1 \qquad \textbf{(2.30)}$$

The relative motion of a two mass system connected by a spring can be modelled as a single body with mass $\mu = \frac{m_1 + m_2}{m_1 m_2}$ (known as the reduced mass) with displacement $q = x_1 + x_2$.

The equation of motion for the single body can be written as:

$$F = \mu \frac{d^2}{dt^2} q = -kq \qquad \textbf{(2.31)}$$

Equation (2.31) is clearly the equation of a harmonic oscillator which has a solution of the form:

$$q(t) = q_0 \sin(\omega t + \phi) \qquad \textbf{(2.32)}$$

where

$$\omega = \sqrt{\frac{k}{\mu}} \qquad \textbf{(2.33)}$$

Making the substitution $\omega = 2\pi\nu_0$, where ν_0 is the natural vibrational frequency of the system, the displacement q of the reduced mass μ as a function of time t, is:

$$q = q_0 \sin(2\pi\nu_0 t + \phi) \qquad \textbf{(2.34)}$$

2.5.2 Classical Description of Raman Scattering

Vandenabeele [8] and Ferraro et al. [9] provide descriptions of the Raman scattering phenomenon using classical physics which are presented below.

The magnitude of the electric field strength E of an EM wave as a function of time is described by **Equation (2.35)** below:

$$E = E_0 \cos(2\pi \nu_E t) \qquad \textbf{(2.35)}$$

where E_0 is the maximum electric field strength and ν_E is the frequency of the wave.

Such a wave will induce an electric diploe moment in a diatomic molecule consisting of two different atomic species (such as the one shown in **Figure 2.8**) due to the difference in electronegativity between the two atoms. The magnitude of the dipole moment p is related to the electric field strength by:

$$p = \alpha E \qquad \textbf{(2.36)}$$

where α is the polarisability of the dipole.

The polarisability of an electric dipole can be thought of as the ease with which the charge distribution of the dipole can be changed. It is dependent on the displacement of the charges (i.e. q as discussed in **Section 2.5.1** above) and may be anisotropic (direction dependent).

For small values of displacement q, the relationship between the polarisability and the displacement can be written as a Taylor series:

$$\alpha = \alpha_0 + \left(\frac{\partial \alpha}{\partial q}\right)_0 q + \ldots \qquad \textbf{(2.37)}$$

where α_0 and $(\partial\alpha/\partial q)_0$ are the polarisability and rate of change of polarisability with displacement at $q = 0$ (i.e. equilibrium) respectively.

Substituting the molecular vibrational frequency ν_m for ν_0 in **Equation (2.34)** the atomic displacement q can be rewritten as:

$$q = q_0 \cos(2\pi\nu_m t) \qquad \textbf{(2.38)}$$

Substituting **Equations (2.37)** and **(2.38)** into **Equation (2.36)** the expression for the electric dipole moment is:

$$p = \alpha_0 E_0 \cos(2\pi\nu_E t) + \left(\frac{\partial\alpha}{\partial q}\right)_0 E_0 q_0 \cos(2\pi\nu_E t)\cos(2\pi\nu_m t) \qquad \textbf{(2.39)}$$

which can be written as:

$$\begin{aligned} p = {} & \alpha_0 E_0 \cos(2\pi\nu_E t) \\ & + \frac{1}{2}\left(\frac{\partial\alpha}{\partial q}\right)_0 E_0 q_0 \cos\{2\pi t(\nu_E + \nu_m)\} \\ & + \frac{1}{2}\left(\frac{\partial\alpha}{\partial q}\right)_0 E_0 q_0 \cos\{2\pi t(\nu_E - \nu_m)\} \end{aligned} \qquad \textbf{(2.40)}$$

The first term of **Equation (2.40)** will cause an electric dipole to generate an EM wave with the same frequency as the incident wave (i.e. Rayleigh scattering) and the other two components result in the production of EM waves with frequencies $\nu_E + \nu_m$ and $\nu_E - \nu_m$, which are the frequencies associated with Raman scattered radiation.

From **Equation (2.40)**, it can be seen that in order for Raman scattering from a vibrating electric dipole to occur, the rate of change of polarisability with respect to displacement at the equilibrium position (i.e. $(\partial\alpha/\partial q)_0$) must be non-zero. In order to illustrate this, consider a linear CO_2 molecule. If the molecule is vibrating with the two bonds connecting the oxygen atoms stretching and compressing at the same time, the polarisability will be higher when the oxygen atoms are further away from the central carbon atom than it will be when they are closer (see **Figure 2.9**). This symmetric vibration mode is therefore Raman active. If the two bonds stretch asymmetrically as shown in **Figure 2.10**, the polarisability will be the same for displacements of $\pm q$ and therefore this mode is Raman inactive.

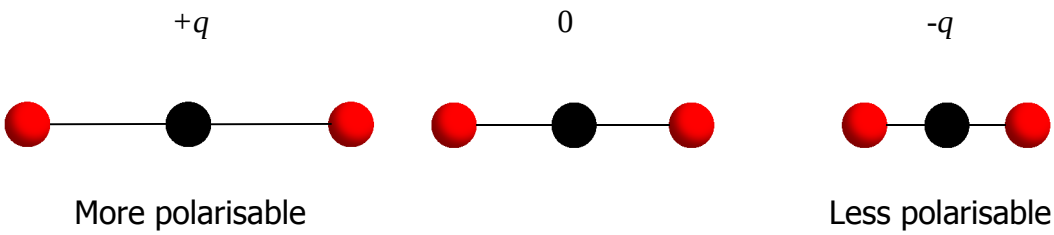

Figure 2.9: Schematic of a CO_2 molecule undergoing symmetric stretching.

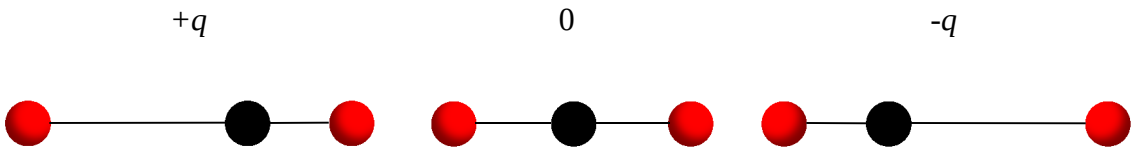

Figure 2.10: Schematic of a CO_2 molecule undergoing asymmetric stretching.

From a quantum perspective, Raman scattering can be thought of as the exchange of energy between a virtual vibrational energy state and a photon. It is possible for a molecule promoted to a virtual vibrational state to decay to a state of higher energy than the original state. In such a case, the photon has transferred energy to the molecule and the molecule emits a photon of frequency $\nu_E - \nu_m$ known as Stokes Raman scattering. Another possibility is for molecule in a virtual vibrational state to decay to a state of lower energy than the original state. In this case a photon with frequency $\nu_E + \nu_m$ is emitted known as anti-Stokes Raman scattering and the molecule has transferred energy to the photon. **Figure 2.11** below illustrates the virtual energy transitions taking place during Rayleigh and Raman scattering. It should be noted that of the scattering processes described above, Rayleigh scattering is by far the most probable outcome and only a very small fraction (approximately 10^{-6} of the incident light according to [10]) is Raman scattered.

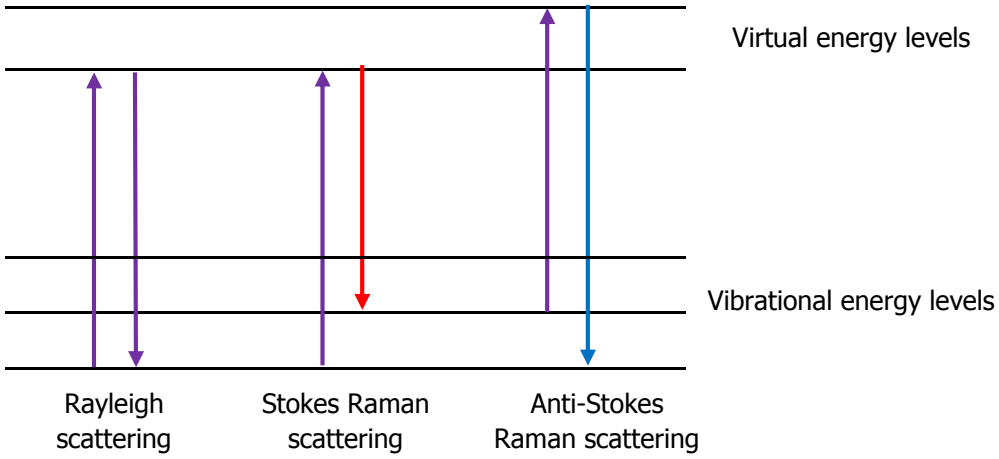

Figure 2.11: Rayleigh and Raman scattered light illustrated in terms of virtual energy levels.

2.5.3 Raman Shift

From classical electromagnetism, the wavelength λ of an EM wave is related to its frequency by:

$$c = \lambda \nu_E \tag{2.41}$$

where c is the speed of light.

From **Equation (2.41)**, a change in the frequency of the incident radiation results in a change to the wavelength λ of the radiation. For convenience, changes in photon energy can be reported in terms of change in wavenumber $\bar{\nu}$ which is defined as:

$$\bar{\nu} = \frac{1}{\lambda} \tag{2.42}$$

which is often measured in units of cm^{-1}.

From **Equations (2.33)**, **(2.41)** and **(2.42)** the frequency of a vibrating molecule can be written as:

$$\bar{\nu} = \frac{1}{2\pi c}\sqrt{\frac{k}{\mu}} \tag{2.43}$$

Equation (2.43) shows that wavenumber is proportional to the square root of the spring constant (bond strength) and inversely proportional to the square root of the mass of the bonded atoms. Different molecules will therefore have different frequencies of vibration and produce different Raman spectra.

2.5.4 Raman Spectroscopy Experimental Setup

Raman spectra were obtained for each sample described in **Section 4.1** using a Horiba LabRAM HR spectrometer (see **Figure 2.12**). All spectra were collected with the samples at room temperature across the range of $\bar{\nu}$ equal to 50-2000 cm^{-1} using a 532 nm (green) laser with a maximum power output of < 500 mW. A grating with 600 lines/mm was used, providing a resolution of 2 cm^{-1}. Laser light was focussed onto millimetre size samples using a ×50 objective lens mounted on a microscope. Spectra were obtained from three different sites on each sample. Each site was scanned five times with an acquisition time of 10 s/scan.

Figure 2.12: Photograph of a Horiba LabRAM HR Spectrometer.

2.6 Chapter 2 References

[1] P. Alfonso, "Properties calculations of silica-based glasses by atomistic simulations techniques: A review," *J. Phys. Chem. C,* vol. 113, pp. 20773-20784, 2009.

[2] A. R. Leach, Molecular Modelling: Principles and Applications, harlow: Addison Wesley Longman Limited, 1996.

[3] D. Frenkel and B. Smit, Understanding Molecular Simulation: From Algorithms to Applications, London: Academic Press, 2001.

[4] J. D. Gale, "GULP - a computer program for the symmetry adapted simulation of solids," *J. Chem. Soc., Faraday Trans.,* vol. 93, pp. 629-637, 1997.

[5] FIZ Karlsruhe - Leibniz-Insitut für Informationsinfrastruktur GmbH, "Inorganic Crystal Structure Database," Eggenstein-Leopoldshafen.

[6] P. J. Goodhew, J. Humphreys and R. Beanland, Electron Microscopy and Analysis, London: Taylor and Francis, 2001.

[7] J. I. Goldstein, D. E. Newbury, P. Echlin, D. C. Joy, A. D. Romig, Jr., C. E. Lyman, C. Fiori and E. Lifshin, Scanning Electron Microscopy and X-Ray Microanalysis, New York: Plenum Press, 1992.

[8] P. Vandenabeele, Practical Raman Spectroscopy: An Introduction, Chichester: John Wiley and Sons Ltd, 2013.

[9] J. R. Ferraro, K. Nakamoto and C. W. Brown, Introductory Raman Spectroscopy, San Diego: Academic Press, 2003.

[10] P. J. Larkin, IR and Raman Spectroscopy, Oxford: Elsevier, 2011.

3. MD Models of Borosilicate Glasses

3.1 Materials Modelled

Prior to making MD models of vitrified HLW wasteforms, it was considered prudent to model borate and borosilicate glasses so that the results of the MD modelling methodology could be compared with MD models of similar glasses reported in the literature and experimental data. The results of MD models of B_2O_3, mixed alkali borosilicate and "MW" glass created using both Buckingham and BHM potentials are reported in this Chapter. All MD models reported in this Chapter were created using the DL_POLY Classic code [1]. The MW base glass is also a component of the wasteforms that will be modelled in Chapter 5.

3.2 Interatomic Potential Functions and Parameters

3.2.1 Buckingham Potential Parameters

The Buckingham potential has the form shown in **Equation (2.15)**. With the exception of the B-O interaction, all values of the parameters A, ρ and C used in this study were obtained from Teter [2] and are listed in **Table 3.1** below. Note that Teter [2] only provided parameters for cation-oxygen and oxygen-oxygen interactions (cation-cation interactions are considered negligible).

The Buckingham potential has the disadvantage that forces become very large at small values of r. This can cause instabilities in calculations. In order to prevent instabilities occurring the DL_POLY code was modified to include a fourth parameter. This additional parameter (designated $r_{\min}$) acts as a short range cut-off such that forces are not computed at values of r less than $r_{\min}$.

Parameters for the B-O interaction were derived manually using GULP. First, an initial set of parameters were obtained using a feature in GULP where interatomic potential parameters may be fitted to an input crystal structure. Using the input crystal structure of B_2O_3, an set of initial parameters for the B-O interaction were acquired. Energy minimisations were then performed on other crystal structures

containing boron, silicon, lithium and sodium using the acquired parameters. The GULP output for each crystal was then analysed and the energy minimisations were re-run with one of the parameters adjusted by 5 %. The changes in mean cation-oxygen bond length due to the adjusted parameter were noted for each input structure. This process was repeated for each B-O potential parameter A, ρ and C until the differences in mean bond length between the initial and final structures were considered reasonable (i.e. approximately 5 %).

Table 3.1: Buckingham potential parameters obtained from [2]. Note that the B-O interaction parameters were obtained from a manual procedure using GULP.

Atom 1	Charge (e)	Atom 2	Charge (e)	A (eV)	ρ (Å)	C (eV·Å^6)	r_{min} (Å)
O	-1.2	O	-1.2	1844.8	0.34365	192.58	1.60
Si	2.4	O	-1.2	13702.9	0.19382	54.68	1.00
B	1.8	O	-1.2	4300.0	0.18500	11.80	0.90
Na	0.6	O	-1.2	4383.8	0.24384	30.70	1.20
Li	0.6	O	-1.2	41051.9	0.15611	0.00	1.15

3.2.2 Born Huggins Mayer Potential Parameters

The BHM potential has the form shown in **Equation (2.16)**. The values of the parameters A, B, and σ were obtained from a previous study on mixed alkali borosilicate glasses for nuclear waste immobilisation by Connelly et al. [3] and are listed in **Table 3.2**. Note that the parameters C and D in the study by Connelly et al. [3] are equal to zero.

Table 3.2: BHM potential parameters obtained from [3].

Atom 1	Charge (e)	Atom 2	Charge (e)	A (eV)	B (Å^{-1})	σ (Å)
O	-2	O	-2	0.1105	2.86	2.84
Si	4	O	-2	0.2763	3.45	2.52
Si	4	B	3	0.663	3.45	1.82
Si	4	Na	1	0.3591	3.45	2.27
Si	4	Li	1	0.442	3.45	1.9
Si	4	Si	4	0.442	3.45	2.2
B	3	B	3	0.884	3.45	1.44
B	3	Na	1	0.5801	3.45	1.89
B	3	Li	1	0.663	3.45	1.52
Na	1	Na	1	0.2763	3.45	2.34
Na	1	Li	1	0.3591	3.45	1.97
Li	1	Li	1	0.442	3.45	1.6
Li	1	O	-2	0.2763	3.45	2.22
B	3	O	-2	0.4973	3.45	2.14
Na	1	O	-2	0.1933	3.45	2.59

3.2.3 GULP Results

The potential parameters listed in **Tables 3.1** and **3.2** above were used in the GULP program along with the crystal structures from the Inorganic Crystal Structure Database (ICSD) [4]. Changes made by GULP to the mean bond lengths and unit cell volumes using Buckingham and BHM potentials are listed in **Tables 3.3** and **3.4** respectively. Average cation-oxygen nearest neighbour distances (described in **Section 1.5.3**) were also calculated. A comprehensive set of GULP results using Buckingham and BHM potentials are presented in **Appendices A and B** respectively. Note that $Na_2B_4O_7$ has two B-O bond lengths, one for three-coordinated boron atoms and the other four-coordinated boron atoms. Changes to the mean bond lengths for three- and four-coordinated boron are denoted [B3] and [B4] respectively in **Tables 3.3** and **3.4**. It is worth mentioning that it was difficult to obtain a set of potential parameters for B-O that produced acceptable results in crystal structures containing three- and four-coordinated boron.

Table 3.3: Unit cell volume and mean bond length changes made by GULP using Buckingham potentials listed in Table 3.1.

Chemical name	Chemical formula	ICSD [4] reference	Unit cell volume change (%)	Mean bond length change (%)			
				B-O	Si-O	Na-O	Li-O
Diboron trioxide	B_2O_3	16021	13.21	0.73		-	-
Alpha quartz	SiO_2	16331	1.42	-	-1.85	-	-
		83849	1.68	-	-1.24	-	-
Lithium oxide	Li_2O	642216	-5.28	-	-	-	-5.28
		60431	-1.45	-	-	-	-0.49
Sodium oxide	Na_2O	644917	-5.59	-	-	-2.07	-
Sodium borosilicate	$NaBSiO_4$	39459	7.24	4.14	-2.45	5.62	-
Disodium boron oxide	$Na_2B_4O_7$	2040	6.01	[B3] 0.73 [B4] 2.70	-	3.16	-
Sodium dilithium borate	$NaLi_2BO_3$	62532	2.84	-0.72	-	0.80	1.51

Table 3.4: Unit cell volume and mean bond length changes made by GULP using BHM potentials listed in Table 3.2.

Chemical name	Chemical formula	ICSD [4] reference	Unit cell volume change (%)	Mean bond length change (%)			
				B-O	Si-O	Na-O	Li-O
Diboron trioxide	B_2O_3	16021	69.15	-1.46		-	-
Alpha quartz	SiO_2	16331	10.60	-	-1.85	-	-
		83849	10.88	-	-1.24	-	-
Lithium oxide	Li_2O	642216	-3.65	-	-	-	-3.65
		60431	0.24	-	-	-	-0.99
Sodium oxide	Na_2O	644917	-3.05	-	-	-1.24	-
Sodium borosilicate	$NaBSiO_4$	39459	20.77	1.38	-3.68	15.66	-
Disodium boron oxide	$Na_2B_4O_7$	2040	27.81	[B3] -2.19 [B4] 0.00	-	5.58	-
Sodium dilithium borate	$NaLi_2BO_3$	62532	13.63	-4.35	-	3.61	0.00

From **Table 3.3** and **Table 3.4** it can be seen that both the Buckingham and BHM potential parameters produce small changes (i.e. < 4 %) in the average bond length for Si-O in all the structures tested. The mean B-O and Li-O bond length changes range between 0.5 % and 6% and are considered reasonable. The changes for the mean Na-O bond lengths were considered reasonable in all crystals except $NaBSiO_4$ where the mean bond length increases substantially using BHM potentials.

It is acknowledged that some of the unit cell volumes changes are relatively large (> 10 %), in particular the results for B_2O_3, $NaBSiO_4$ and $Na_2B_4O_7$ when using BHM potentials. However, since the majority of mean bond length changes are considered reasonable, the potential parameters were considered fit for use in MD simulations.

3.3 B_2O_3 Glass Simulations

Two Molecular Dynamics (MD) simulations of B_2O_3 glass were created using the DL_POLY Classic code. The first simulation (designated B_2O_3 #1), made use of the Buckingham potential parameters listed in **Table 3.1** and the second (designated B_2O_3 #2), used the BHM potential parameters listed in **Table 3.2**.

3.3.1 B_2O_3 Glass Simulation Details

Each simulation consisted of 500 atoms (200 boron and 300 oxygen). In the B_2O_3 #1 simulation a time-step of 10^{-3} ps was used whereas in B_2O_3 #2 it was found necessary to use a time-step of 10^{-4} ps to maintain stable temperatures. An initial random configuration was generated by creating a 'box' containing the desired number of atoms at an experimentally determined density of 1.84 $g \cdot cm^{-3}$ [5]. It is worth noting that the same random configuration was used as the initial configuration for both models. In both simulations the initial configuration was equilibrated at 6000 K in the canonical (i.e. constant volume and temperature (NVT)) ensemble to remove the 'randomness' of the configuration. The atoms were then simulated at temperatures of 4000 K and then 2000 K before undergoing a rapid 'quench' phase from 2000 K to 300 K

(note that crystalline B_2O_3 has a melting point of 450 °C [i.e. 723 K] [6]). Following the quench phase, the atoms were simulated at 300 K. The duration of each 'temperature phase' in the B_2O_3 #1 and B_2O_3 #2 simulations are shown in **Tables 3.5** and **3.6** respectively. Quench rates of 2×10^{13} $K \cdot s^{-1}$ and 2×10^{14} $K \cdot s^{-1}$ were used in the B_2O_3 #1 and B_2O_3 #2 simulations respectively. It is recognised that the quench rates in the models were inconsistent. However it is not considered likely that this had any significant effect on the results. With the exception of the time steps, the same CONTROL file parameters were used in both models. As an example, the CONTROL file for the B_2O_3 # 1 300 K stage is shown in **Appendix C**.

Table 3.5: Heat treatment scheme for B_2O_3 #1.

Ensemble	Temperature (K)	Time-step length (ps)	Total number of time steps	Number of time steps without equilibration	Total duration (ps)
NVT	6000	10^{-3}	50 000	10 000	50
NVT	4000	10^{-3}	50 000	10 000	100
NVT	2000	10^{-3}	50 000	10 000	150
NVT	2000-300	10^{-3}	86 000	1 000	236
NVT	300	10^{-3}	50 000	10 000	286

Table 3.6: Heat treatment scheme for B_2O_3 #2.

Ensemble	Temperature (K)	Time-step length (ps)	Total number of time steps	Number of time steps without equilibration	Total duration (ps)
NVT	6000	10^{-4}	500 000	100 000	50
NVT	4000	10^{-4}	500 000	100 000	100
NVT	2000	10^{-4}	500 000	100 000	150
NVT	2000-300	10^{-4}	860 000	10 000	236
NVT	300	10^{-4}	500 000	100 000	286

3.3.2 B_2O_3 Glass Simulation Results

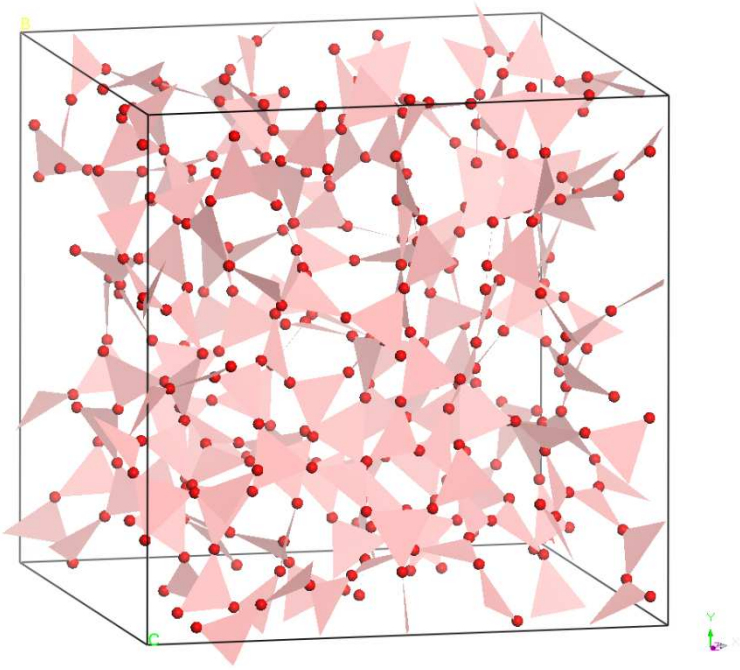

Figure 3.1: Visual representation of the B_2O_3 #1 glass MD model. Pink triangles represent boron atoms and red spheres are oxygen atoms.

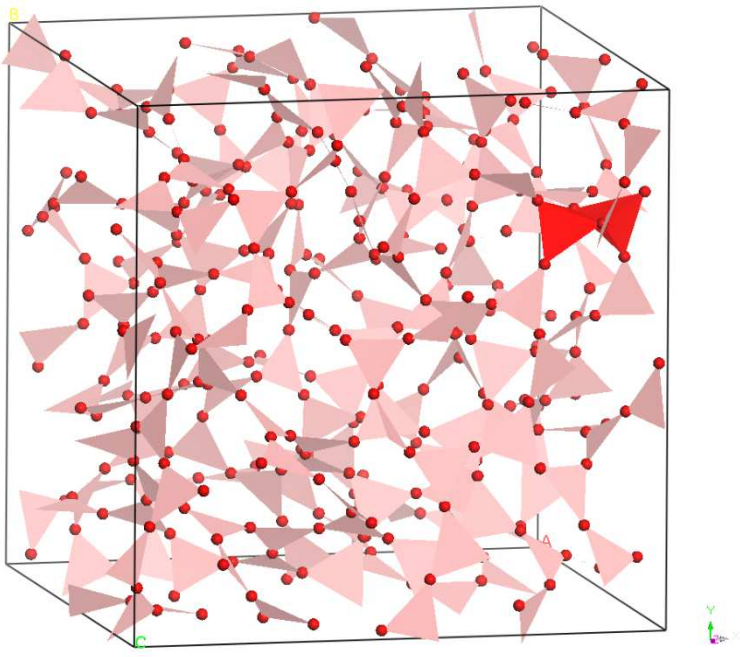

Figure 3.2: Visual representation of the B_2O_3 #2 MD glass model. Pink triangles represent boron atoms and red spheres are oxygen atoms. Boron tetrahedra are highlighted in red.

Inspection of **Figure 3.1** shows that all boron atoms are three coordinated whereas in **Figure 3.2** there are two four-coordinated boron atoms (highlighted in red). Note that four-coordinated boron is not expected in pure B_2O_3.

B_2O_3 Structure Factors

The Interactive Structure of Amorphous and Crystalline Systems (ISAACS) program [7] was used to calculate neutron diffraction pair distribution functions from the DL_POLY REVCON files at 300 K. The distribution functions were then used to calculate structure factors. The calculated structure factors were compared with structure factors reported from experimental neutron structure factors [8]. The structure factors are shown in **Figure 3.3**.

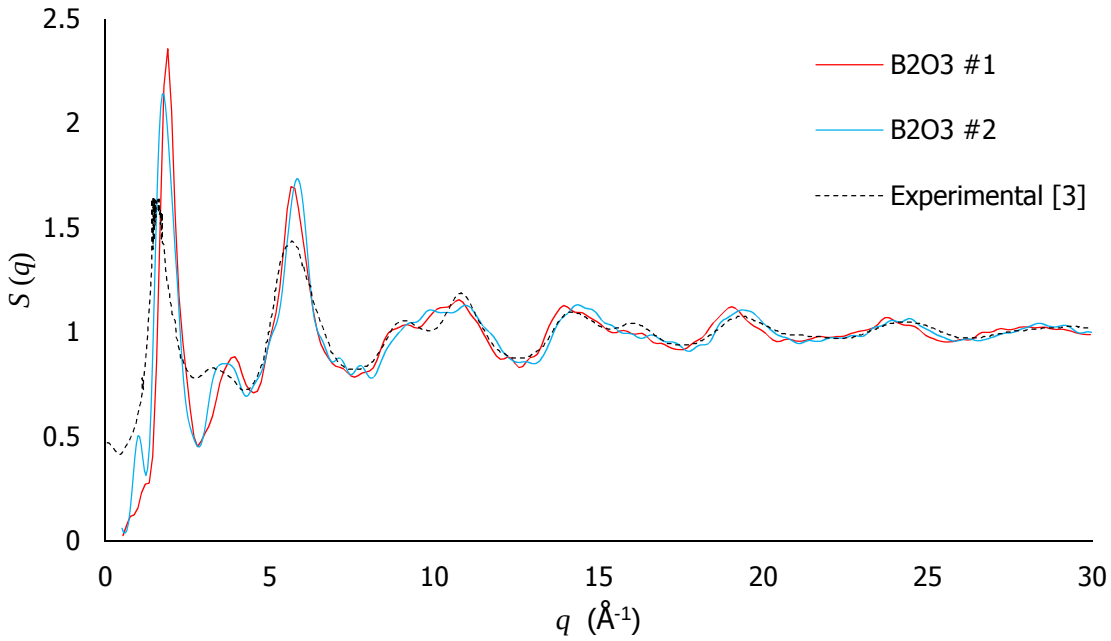

Figure 3.3: Neutron diffraction structure factors derived from MD models and experimental data [8].

Figure 3.3 shows that the structure factors obtained from the MD simulations are in general agreement with the experimental data. There is a slight difference between B_2O_3 #1 and B_2O_3 #2 in terms of the positions of the peaks in the neutron diffraction structure factor.

B_2O_3 Glass Radial Distribution Functions

The output of the radial distribution functions (RDFs) $g(r)$ for B_2O_3 #1 and B_2O_3 #2 are shown in **Figure 3.4** below.

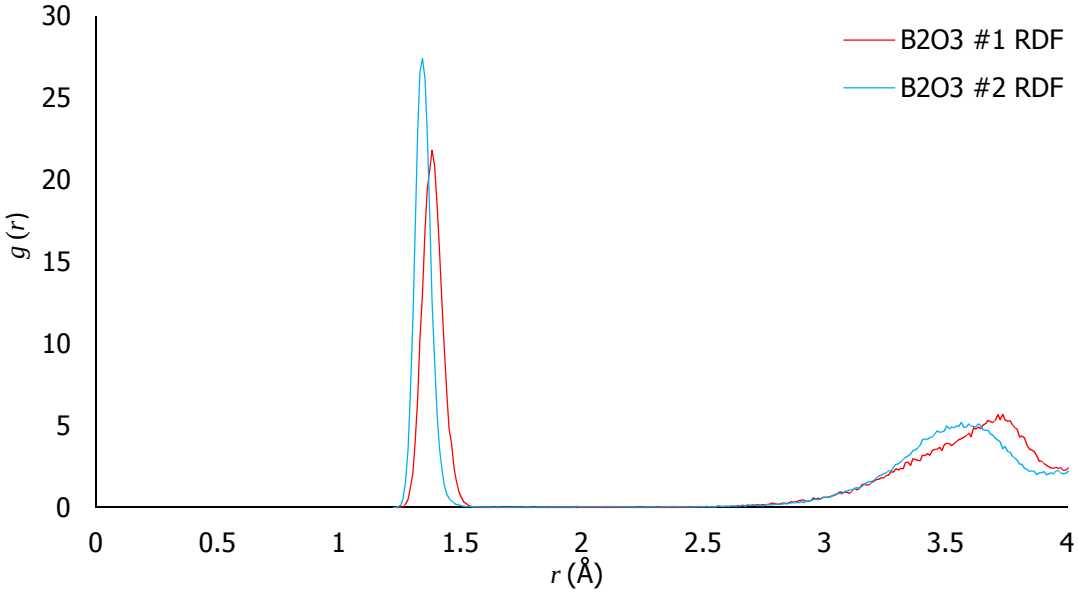

Figure 3.4: Radial distribution functions from simulations of B_2O_3 glass.

The average B-O nearest neighbour distances, $<d_{B\text{-}O}>$ found in the simulations of B_2O_3 in this study are presented in **Table 3.7** below and are compared with values from a previous MD study by Kashchieva et al. [5] and experimental data [9, 10].

Table 3.7: Average B-O nearest neighbour distances (σ represents standard deviations).

Reference data	$<d_{B\text{-}O}>$ (Å)	% difference between $<d_{B\text{-}O}>$ and simulation B_2O_3 #1	% difference between $<d_{B\text{-}O}>$ and simulation B_2O_3 #2
B_2O_3 #1 (this study)	1.39	N/A	2.97
σ (Å)	0.04		
B_2O_3 #2 (this study)	1.35	-2.89	N/A
σ (Å)	0.03		
MD Model Ref. [5]	1.371	-1.01	1.93
Experimental data Ref. [9]	1.366	-1.37	1.56
Experimental data Ref. [10]	1.370	-1.08	1.86

The values of $<d_{B\text{-}O}>$ found in the B_2O_3 #1 and B_2O_3 #2 simulations are both within one standard deviation of distances found in the MD study by Kashchieva et al. [5] and the experimentally determined distances in [9, 10].

B_2O_3 Glass Coordination Numbers

The cumulative coordination numbers $CN(r)$ for B-O for B_2O_3 #1 and B_2O_3 #2 are presented in **Figure 3.5** below.

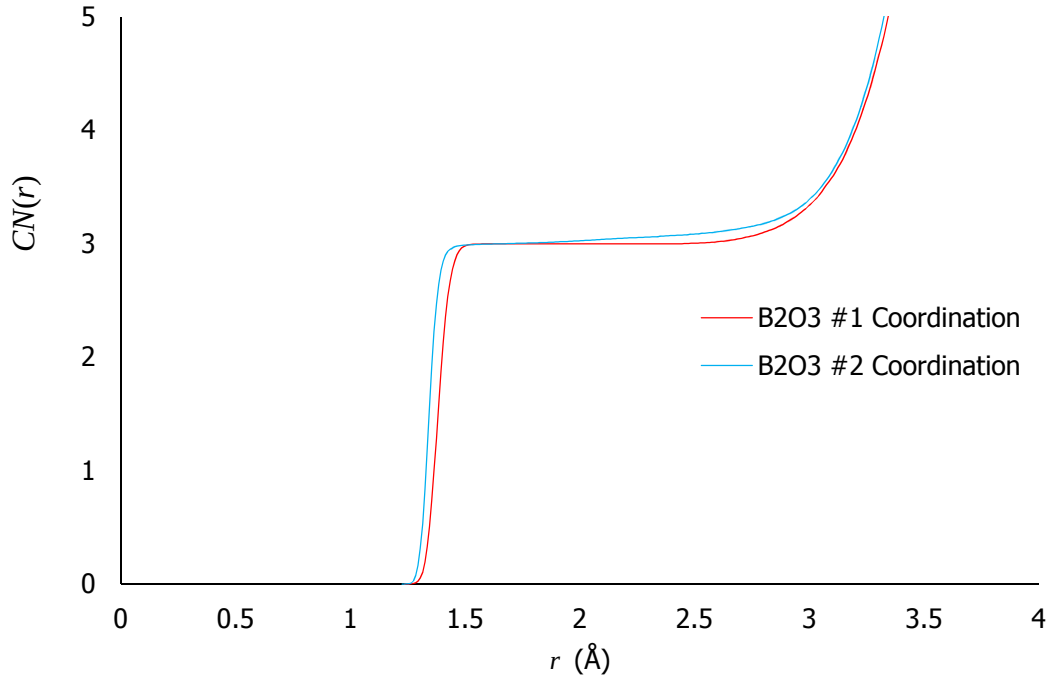

Figure 3.5: B-O coordination numbers predicted by MD simulations of B_2O_3 glass.

In B_2O_3 #1 the coordination number remains at a constant value of three in the range $1.5 < r < 2.4$ Å. This indicates that all boron atoms are three-coordinated to oxygen. However in B_2O_3 #2, the gradient momentarily becomes zero at $r \approx 1.5$ Å and then becomes slightly positive. This indicates that a small number of boron atoms have a coordination number of four for values of r between 1.5 and 2.4 Å. This is considered to be unrealistic in a model of B_2O_3.

B_2O_3 Glass Bond Angle Distributions

The bond angle distributions (BADs) for O-B-O for the B_2O_3 #1 and B_2O_3 #2 models are shown in **Figure 3.6** below.

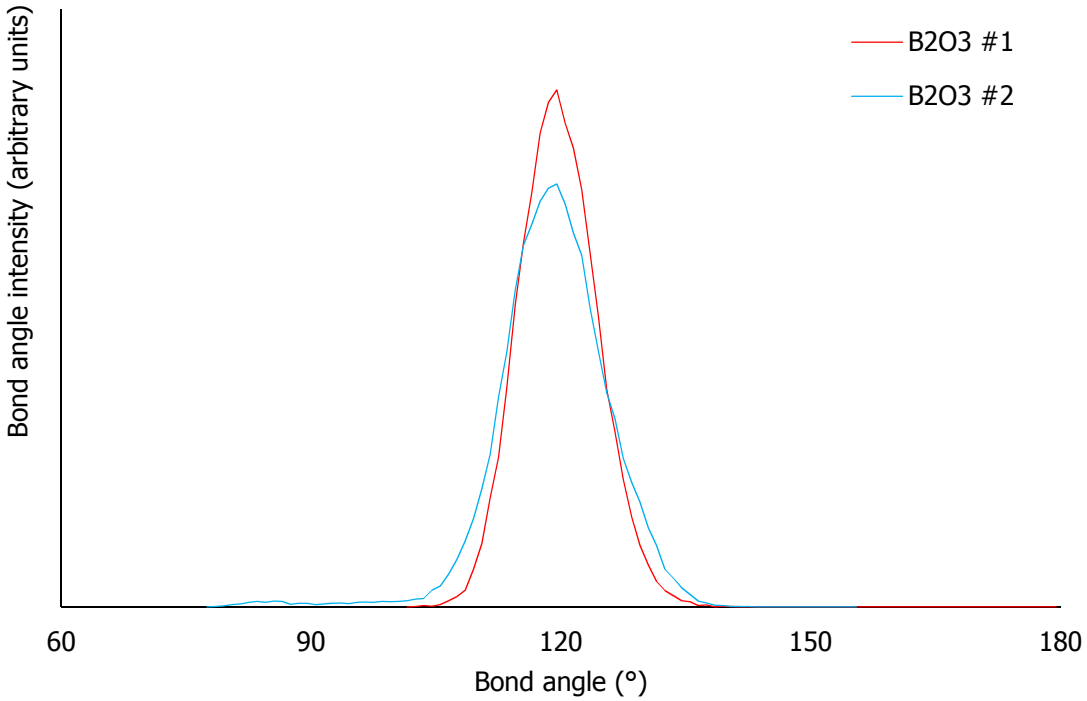

Figure 3.6: O-B-O bond angle distributions from simulations of B_2O_3 glass.

The average O-B-O bond angles were found to be 120° (σ = 5 °) for B_2O_3 #1 and 119° (σ = 6 °) for B_2O_3 #2. These results are consistent with what would be expected in a glass consisting of BO_3 triangular units.

B_2O_3 Glass Network connectivity results

As reported above, all boron atoms were found to be three-coordinated to oxygen. The Q^n analysis for B_2O_3 #1 showed that all structural units are Q^3 (or T^3) units as expected for a model of pure B_2O_3 glass. For B_2O_3 #2, 97 % of boron atoms were found to be three-coordinated to oxygen with the remaining 3 % being four-coordinated (which is unrealistic for pure B_2O_3).

3.4 Alkali Borosilicate Glass Simulations

In this part of the study, MD models of mixed alkali borosilicate (ABS) glasses were produced for comparison with a previous MD study of such glasses by Connelly et al. [3]. In the study by Connelly et al. [3], glasses with compositions of the form $K(SiO_2)\cdot B_2O_3\cdot R(M_2O)$ (where $K = SiO_2/B_2O_3$, $R = M_2O/B_2O_3$, and M is a monovalent cation species) were simulated using BHM-type two-body potentials to describe the forces between all the atomic species along with three-body potentials to describe the O-Si-O and Si-O-Si bond angles. In mixed alkali borosilicate glasses boron atoms may coordinate with three oxygen atoms to form planar BO_3 triangles (as expected in B_2O_3 glass), or, they may coordinate with four oxygen atoms to form BO_4 tetrahedrons.

3.4.1 Alkali Borosilicate Glass Simulation Details

In this work two models of a mixed alkali borosilicate (ABS) glass with the composition K = 3, R = 0.15 were created. Each model consisted of 180 silicon atoms, 549 oxygen atoms, 120 boron atoms, 9 sodium and 9 lithium atoms. The first model (designated ABS #1) used Buckingham potentials to describe the interactions between each atom type and oxygen only. The second model (designated ABS #2), used the two-body BHM potentials utilised by Connelly et al. [3]. The potential parameters used for ABS #1 and ABS #2 are shown in **Table 3.1** and **Table 3.2** respectively. It should be noted that no three-body potentials were used in either ABS #1 or ABS #2. The heat treatment scheme used for both ABS #1 and ABS #2 is shown in **Table 3.8**.

Some of the models created by Connelly et al. [3] made use of the constant temperature and pressure (NPT) ensemble with an external pressure of 62 kbar (= 61 katm) in order to increase the number of four-coordinated boron atoms. The ABS glass models reported in this work also use this technique in order to increase the number of four-coordinated boron atoms.

The same CONTROL file was used for both models and an example CONTROL file is shown in **Appendix C**.

Table 3.8: Heat treatment scheme for ABS #1 and ABS #2.

Ensemble	Temperature (K)	Pressure (katm)	Time-step length (ps)	Total number of time steps	Number of time steps with equilibration	Total duration (ps)
NVT	6000	0	10^{-3}	100 000	100 000	100
NPT	6000	61	10^{-3}	200 000	200 000	300
NVT	4000	61	10^{-3}	100 000	100 000	400
NPT	4000	61	10^{-3}	200 000	200 000	600
NVT	2000	61	10^{-3}	100 000	100 000	700
NPT	2000	61	10^{-3}	200 000	200 000	900
NVT	2000 - 300	61	10^{-3}	86 000	85 000	986
NPT	300	61	10^{-3}	200 000	150 000	1186

3.4.2 Alkali Borosilicate Glass Simulation Results

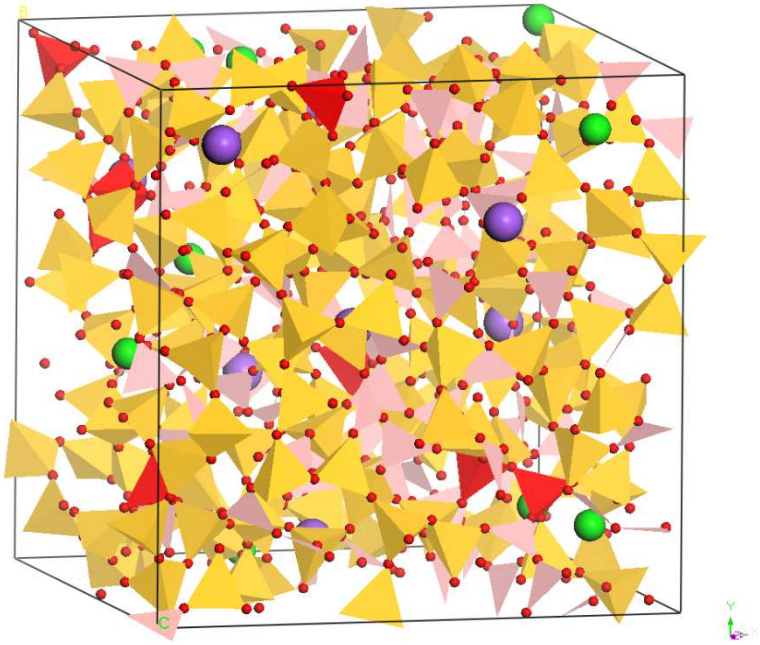

Figure 3.7: Visual representation of the ABS #1 glass MD model.

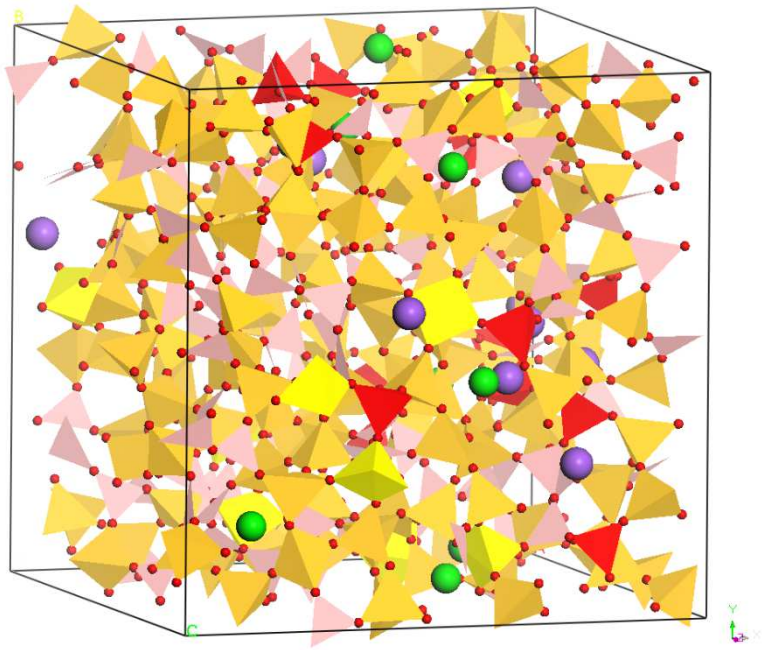

Figure 3.8: Visual representation of the ABS #2 glass MD model.

Table 3.9: Key for Figure 3.7 and Figure 3.8.

gold tetrahedra:	silicon (4-coordianted)	pink triangles:	boron (3-coordinated)
yellow polyhedra:	silicon (coordination > 4)	red polyhedra:	boron (coordination > 3)
green spheres:	lithium	purple spheres:	sodium
red spheres:	oxygen		

Inspection of **Figure 3.7** showed that all silicon atoms are four coordinated (as would be expected). However a small number silicon atoms with a coordination greater than four can be observed in **Figure 3.8**. Further inspection of **Figures 3.7** and **3.8** also revealed more four-coordinated boron atoms in the ABS #2 model.

ABS Glass Radial Distribution Functions

The RDFs obtained from the ABS #1 and ABS #2 simulations for each cation to oxygen are shown in **Figure 3.9** below. Solid lines are from ABS #1 and dashed lines are from ABS #2. The average cation-oxygen nearest neighbour distances $<d_{X\text{-}O}>$, are presented in **Table 3.10**. These distances are compared with those obtained in the MD study by Connelly et al. [3], an MD study of sodium silicate glasses by Pota et al [11] and experimentally obtained values for sodium-borate glasses, silicate glasses and sodium borosilicate glasses [12, 13, 14].

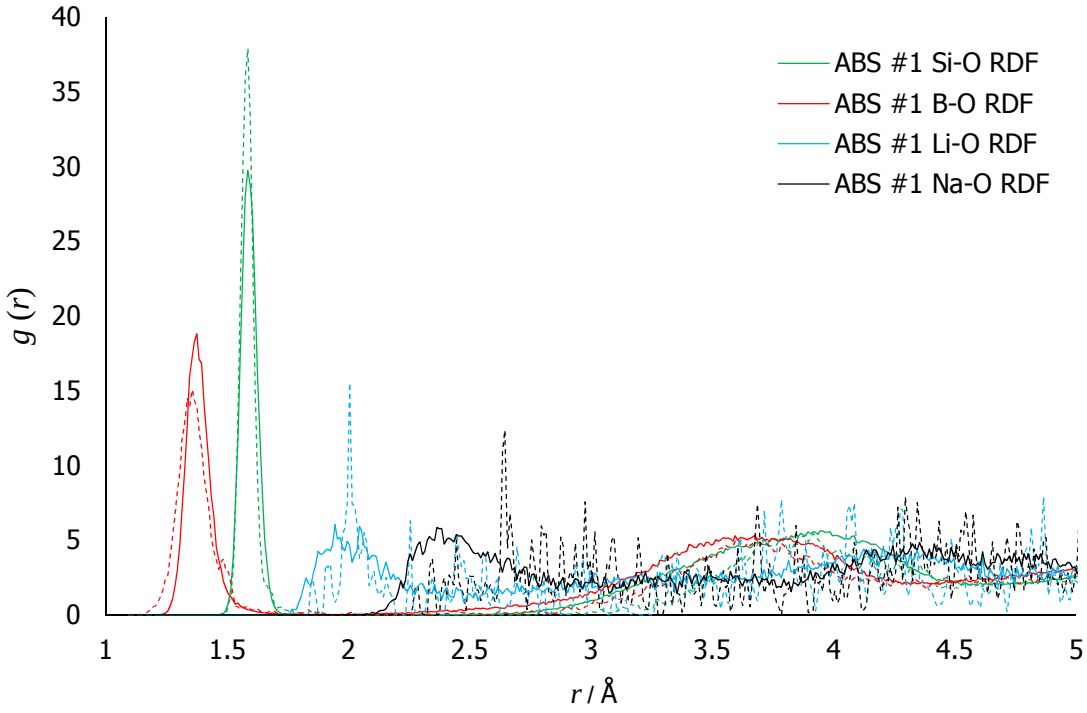

Figure 3.9: Radial distribution functions from simulations of mixed alkali borosilicate (K = 3, R = 0.15) glass. Solid lines are from ABS #1 and dashed lines are from ABS #2.

The B-O RDF for ABS #2 has a maxima occurring at 1.36 Å; close inspection of the B-O RDF reveals a second maxima occurring at 1.49 Å prior to the function approaching zero as illustrated in **Figure 3.10**. It is reasoned that the first maxima observed in the B-O RDF for ABS #2 corresponds to the average nearest neighbour distance for BO_3 triangular units ($<d_{B\text{-}O[3]}>$) and the second peak corresponds to the average nearest neighbour distance for BO4 tetrahedral units ($<d_{B\text{-}O[4]}>$). The value $<d_{B\text{-}O[4]}>$ reported in **Table 3.10** corresponds to the value of r at which the second maxima occurs in the ABS #2 B-O RDF. It is noted that no second maxima was observed in the B-O RDF curve for ABS #1. The study by Connelly et al. [3] also reports two bond lengths associated with the B-O interaction, one for three-coordinated boron (BO_3 triangular units) and the other for four-coordinated boron (BO_4 tetrahedral units). These bond lengths are also reported in **Table 3.10**.

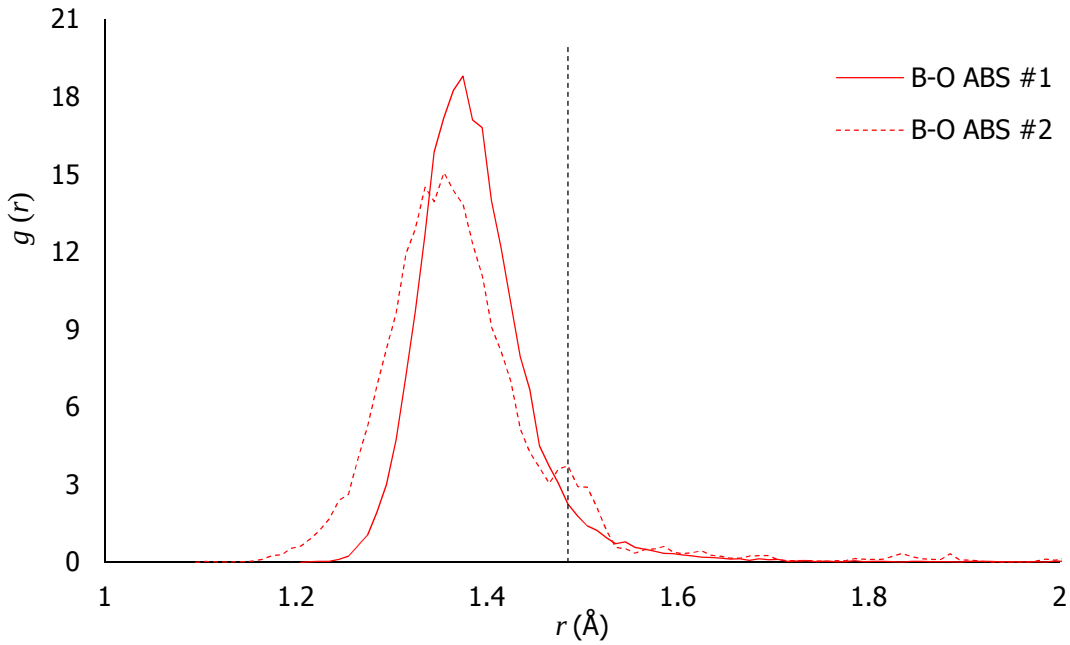

Figure 3.10: Radial distribution functions for B-O from simulations of mixed alkali borosilicate (K = 3, R = 0.15) glass.

Table 3.10: Average nearest neighbour distances from simulations ABS #1 and ABS #2 and the literature (σ represents standard deviation).

Reference data	$<d_{Si\text{-}O}>$ (Å)	$<d_{B\text{-}O\ [3]}>$ (Å)	$<d_{B\text{-}O\ [4]}>$ (Å)	$<d_{Li\text{-}O}>$ (Å)	$<d_{Na\text{-}O}>$ (Å)
ABS #1	1.59	1.39	-	2.08	2.57
σ (Å)	0.04	0.06	-	0.17	0.24
ABS #2	1.59	1.38	1.49	2.06	2.79
σ (Å)	0.04	0.05	0.13	0.12	0.25
Ref. [3]	1.58	1.34	1.46	2.07	2.82
Ref. [11]	1.62				2.34
Ref. [12]		1.37	1.42		
Ref. [13]	1.64				
Ref. [14]	1.62				

From the data in **Table 3.10** the Si-O, B-O and Li-O bond lengths from the ABS #1 and ABS #2 simulations are considered to be consistent with those from Connelly et al's simulation [3]. The ABS #1 simulation did not provide distinguishable bond lengths for three- and four-coordinated boron as ABS #2 did. The average Na-O distance in ABS #1 is considerably shorter than the Na-O distance predicted by Connelly et al's [3] model and ABS #2, however it is closer to the Na-O distance predicted by Pota et al [11].

ABS Glass Coordination Numbers

Plots of the coordination numbers $CN(r)$ for Si-O and B-O obtained from ABS #1 and ABS #2 are shown in **Figure 3.11** below.

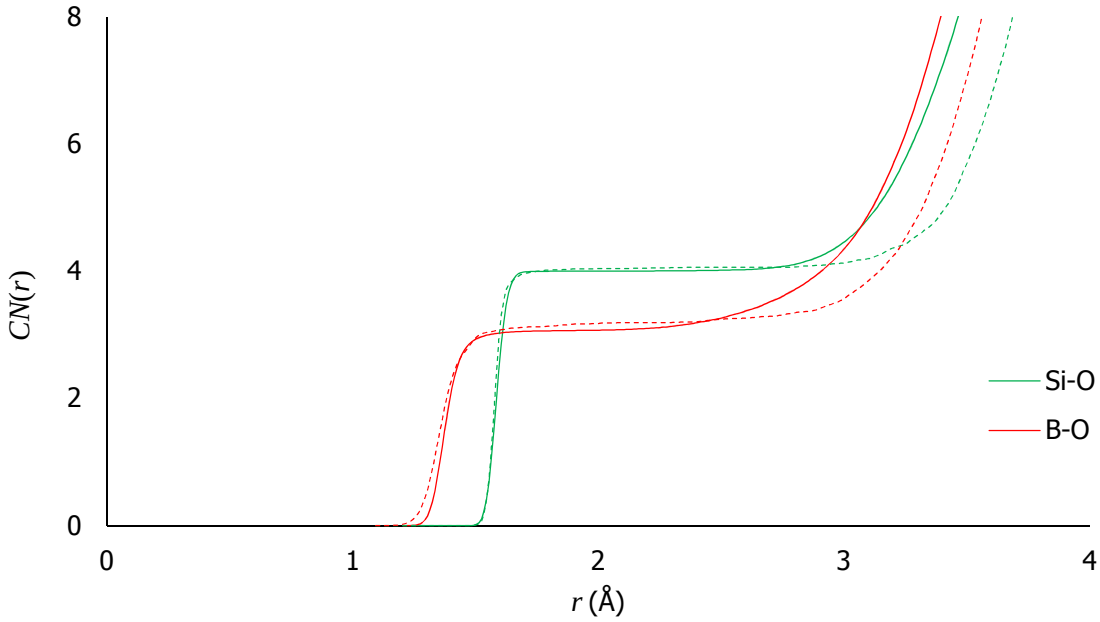

Figure 3.11: B-O and Si-O coordination numbers predicted by MD simulations of mixed alkali borosilicate (K = 3, R = 0.15) glass. Solid lines are from ABS #1 and dashed lines are from ABS #2.

In the study by Connelly et al. [3], the fraction of four-coordinated boron (B4) atoms predicted by MD simulations were compared with experimental values obtained by Roderick et al. using Nuclear Magnetic Resonance (NMR) Spectroscopy [15]. For the composition K = 3, R = 0.15, the fraction of B4 atoms found in the experimental study by Roderick et al. [15] was ~ 0.18. In the study by Connelly et al. [3], the B4 fraction was found to be ~ 0.17 when using the NPT ensemble with an applied pressure of 62 kbar. However, the resulting change in volume (density) is not reported. In this study, the fraction of four-coordinated boron was found to be 0.19 when using the same ensemble, pressure and BHM potentials (ABS #2). However when performing the same simulation with Buckingham potentials (ABS #1), the B4 fraction was found to be ~ 0.08.

All silicon atoms were found to be four-coordinated to oxygen in the ABS #1 simulation whereas 95% of the silicon atoms were four-coordinated to oxygen in the ABS #2 simulation (the remaining 5% being 5 coordinated which is considered unrealistic). It is considered likely that the use of a three-body potential would have restricted the silicon atoms to four-coordinating with oxygen as shown in the study by Connelly et al. [3]. The three-body potentials used by Connelly et al. [3] to constrain O-Si-O and Si-O-Si bond angles were not applied in this study since this required further amendment to the DL_POLY source code.

ABS Glass Bond Angle Distributions

The bond angle distributions from the simulations of ABS glass are shown in **Figure 3.12** and the average bond angles are reported in **Table 3.11**.

From the data in **Table 3.11**, both the ABS #1 and ABS #2 models produced average O-Si-O bond angles of 109 ° indicating the presence of SiO_4 tetrahedra. Both models also produced average O-B-O angles which are close to the value of 120° which would be expected for BO_3 triangular units. However, the average O-B-O angle for ABS #2 is slightly lower than ABS #1. On close inspection of **Figure 3.12**, a local maxima can be observed at 107° due to the presence of four-coordinated boron atoms.

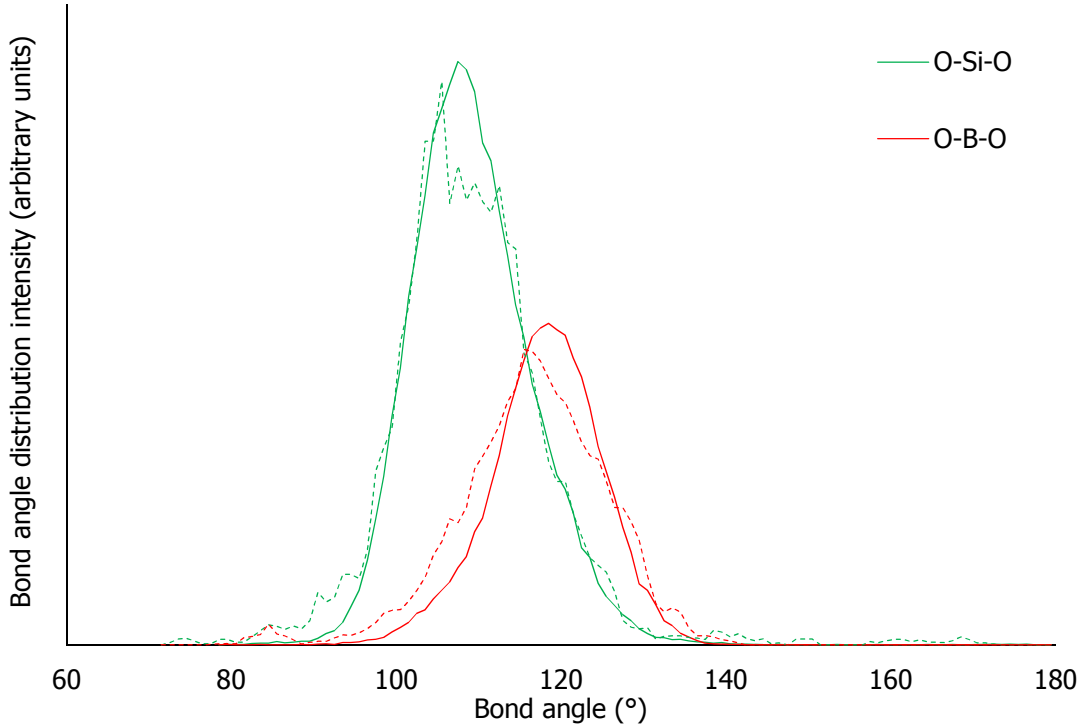

Figure 3.12: Bond angle distributions from simulations of mixed alkali borosilicate (K = 3, R = 0.15) glass. Solid lines are from ABS #1 and dashed lines are from ABS #2.

Table 3.11: Average bond angles from simulations of alkali borosilicate (K = 3, R = 0.15) glass (σ is the standard deviation).

Model	<O-Si-O>	<O-B-O>
ABS #1	109°	118°
σ	7°	7°
ABS #2	109°	116
σ	9°	9°

ABS Glass Network Connectivity Analysis Results

The Q^n analysis results for the ABS glass simulations are shown in **Table 3.12** below. Uncertainties were derived by assuming a counting accuracy of ±1 atom in each Q^n group.

Table 3.12: Network connectivity analysis for simulations of alkali borosilicate (K = 3, R = 0.15) glass. Uncertainties were derived assuming a counting accuracy of ± 1 atom in each Q^n group.

Model	Network former	Fraction of atoms in Q^n group					Average Q^n
		Q^0	Q^1	Q^2	Q^3	Q^4	
ABS #1	Si	2.8 % ± 0.6 %	7.2 ± 0.6 %	32.8 % ± 0.6 %	38.3 % ± 0.6 %	18.9 % ± 0.6 %	2.63
ABS #2	Si	0.6 % ± 0.6 %	7.8 % ± 0.6 %	32.2 % ± 0.6 %	41.6 % ± 0.6 %	17.8 % ± 0.6 %	2.68
ABS #1	B	28.3% ± 0.8 %	44.2% ± 0.8 %	23.3% ± 0.8 %	4.2% ± 0.8 %	0.0% ± 0.8 %	1.03
ABS #2	B	25.0% ± 0.8 %	40.8% ± 0.8 %	25.8% ± 0.8 %	7.6% ± 0.8 %	0.8% ± 0.8 %	1.18

The data in **Table 3.12** shows that there is very little difference in silicon connectivity between the two models. The ABS #2 model has a slightly higher average boron connectivity than ABS #1. This is most likely because of the higher number of four-coordinated boron in the ABS #2 model.

3.5 MW Glass Simulations

In a similar vein the to the simulations of K=3, R=0.15 glass, MD studies of the mixed alkali borosilicate glass composition used for immobilisation of nuclear waste (known as MW glass) were made using BHM and Buckingham potentials. MW glass is a mixed alkali borosilicate glass with composition K = 3.26, R = 1.12 (60.61 mol % SiO_2, 18.57 mol % B_2O_3, 10.53 mol % Na_2O and 10.29 mol % Li_2O) [16]. It is worth making clear that the glass modelled is "full lithium" MW glass and not the "MW-½Li" mixture described in **Chapter 1**. The results of the simulations are compared with those from an additional study by Connelly et al [17] in which full Lithium MW glass is modelled (denoted as FLi).

3.5.1 MW Glass Simulation Details

The MW glass simulations consisted of 147 silicon, 480 oxygen, 90 boron, 52 sodium and 50 lithium atoms. The first model (designated MW #1) used Buckingham potentials to describe the interactions between each atom type and oxygen only. The second model (designated MW #2), used the BHM potentials utilised by Connelly et al. [3]. The potential parameters used for MW #1 and MW #2 are shown in **Table 3.1** and **Table 3.2** respectively. It should be noted that no three-body potentials were applied in either simulation. The heat treatment scheme used in the models is shown in **Table 3.13** below.

Table 3.13: Heat treatment scheme for MW #1 and MW #2.

Ensemble	Temperature (K)	Pressure (katm)	Time-step length (ps)	Total number of time steps	Number of time steps with equilibration	Total duration (ps)
NVT	6000	0	5×10^{-4}	100 000	100 000	100
NPT	6000	61	5×10^{-4}	200 000	150 000	300
NVT	4000	61	5×10^{-4}	100 000	100 000	400
NPT	4000	61	5×10^{-4}	200 000	150 000	600
NVT	2000	61	5×10^{-4}	100 000	100 000	700
NPT	2000	61	5×10^{-4}	200 000	150 000	900
NVT	2000 - 300	61	5×10^{-4}	86 000	85 000	986
NVT	300	61	5×10^{-4}	100 000	100 00	1086
NPT	300	61	5×10^{-4}	200 000	150 000	1286

3.5.2 MW Glass Simulation Results

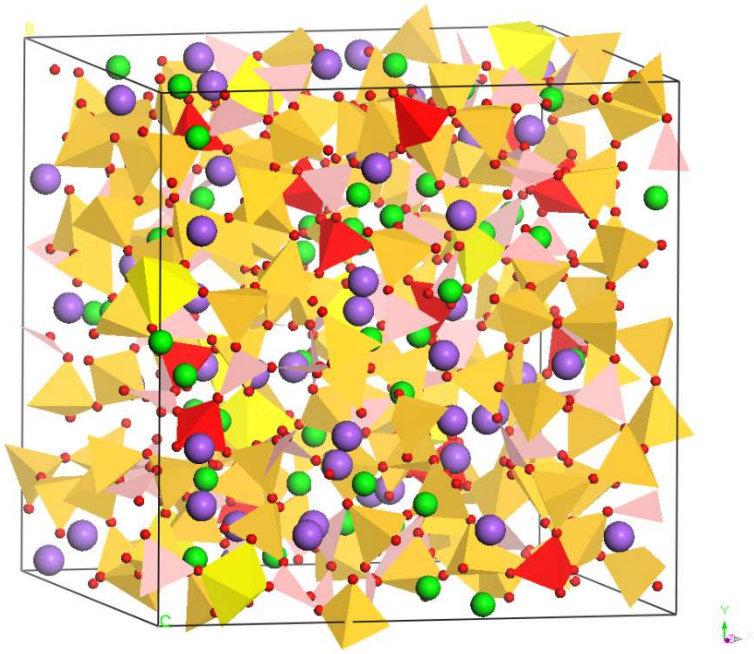

Figure 3.13: Visual representation of the MW #1 glass MD model.

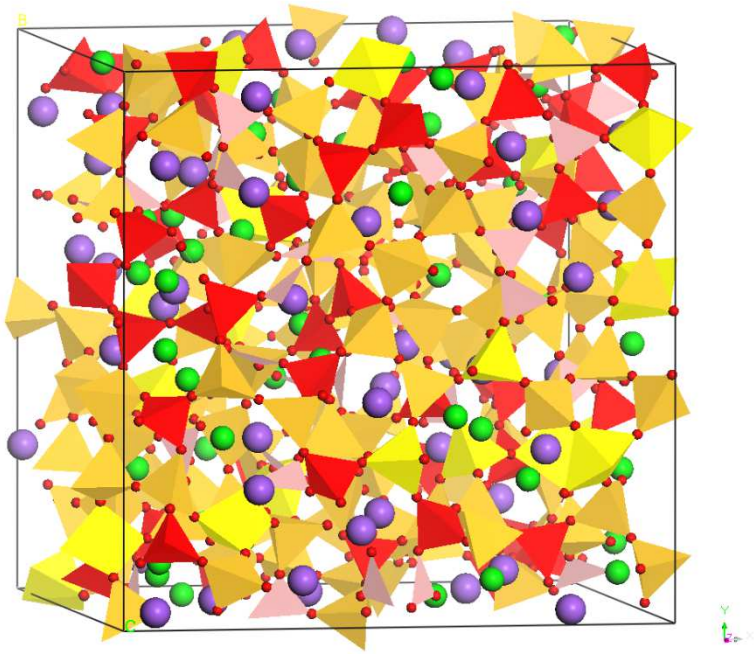

Figure 3.14: Visual representation of the MW #2 glass MD model.

Table 3.9: Key for Figure 3.13 and Figure 3.14.

gold tetrahedra:	silicon (4-coordianted)	pink triangles:	boron (3-coordinated)
yellow polyhedra:	silicon (coordination > 4)	red polyhedra:	boron (coordination > 3)
green spheres:	lithium	purple spheres:	sodium
red spheres:	oxygen		

From inspection of **Figures 3.13** and **3.14** is it immediately obvious that the number of silicon atoms with a coordination number greater than four and the number of boron atoms with coordination number greater than three are substantially higher in the MW #2 model. These features are discussed in further detail below.

MW Glass Radial Distribution Functions

The RDFs obtained from the MW #1 and MW #2 simulations are displayed in **Figure 3.15**. The average cation-oxygen nearest neighbour distances are presented in **Table 3.14**. From **Figure 3.15** it can be seen that the first band in the MW #2 B-O RDF contains two maxima. It is supposed that the first maxima corresponds to the bond lengths of the BO_3 triangular units and the second maxima is due to the bond lengths of the BO_4 tetrahedral units. The value of $\langle d_{B\text{-}O[4]} \rangle$ reported in **Table 3.14** corresponds to the value of r at the second maxima in the first band of the MW #2 B-O RDF.

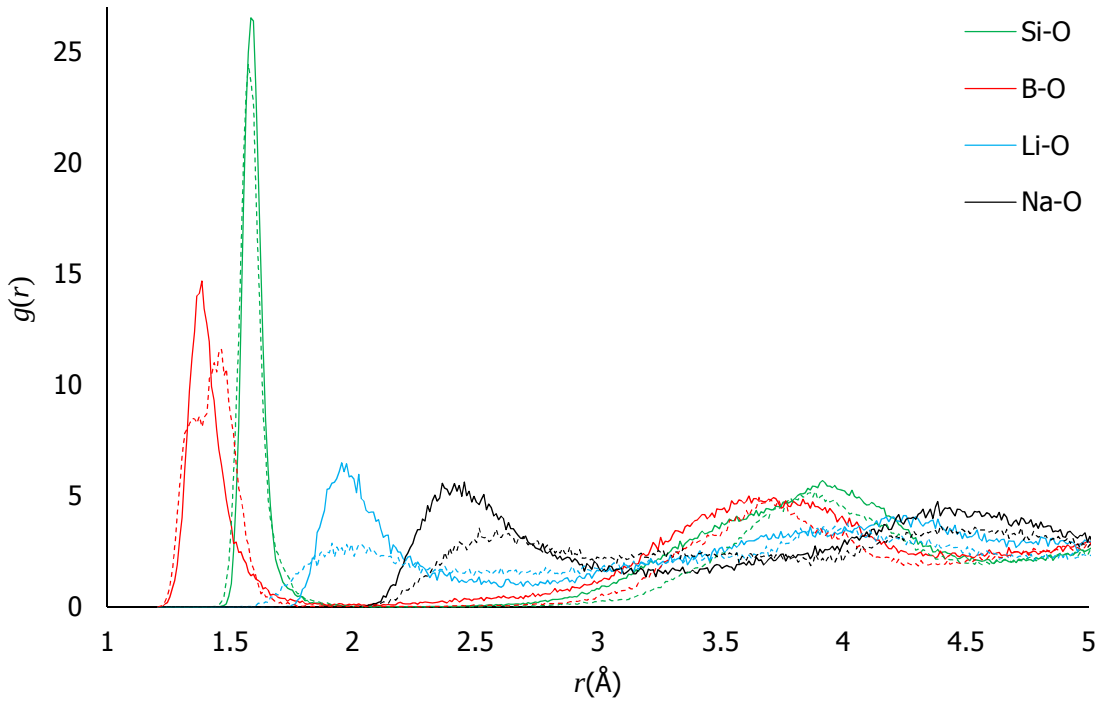

Figure 3.15: Radial distribution functions from simulations of MW glass. Solid lines are from MW #1 and dashed lines are from MW #2.

Table 3.14: Average cation-oxygen nearest neighbour distances.

Reference data	$<d_{Si-O}>$ (Å)	$<d_{B-O\ [3]}>$ (Å)	$<d_{B-O\ [4]}>$ (Å)	$<d_{Li-O}>$ (Å)	$<d_{Na-O}>$ (Å)
MW #1	1.60	1.42	N/A	2.03	2.52
σ (Å)	0.05	0.09	-	0.13	0.20
MW #2	1.59	1.38	1.47	2.00	2.61
σ (Å)	0.06	0.04	0.05	0.16	0.24
FLi-A Ref. [17]	1.57	1.43	-	2.05	2.82
σ (Å)	0.000	0.007	-	0.012	0.006

The Si-O, B-O and bond Li-O lengths from the MW #2 simulation are broadly consistent with those from Connelly et al's simulation [17]. There are however noticeable differences between the Na-O distances reported by Connelly and the results of MW #2. As with the ABS glass simulations, the Na-O distance observed in MW #1 is closer to the value determined by Pota et al [11] than MW #2. It is acknowledged that the standard deviations for the Na-O and Li-O bond lengths are relatively large when compared with the Si-O and B-O and Connelly et al's [17] results. This is due to the larger disorder in Li and Na sites in the glass structure.

MW Glass Coordination Numbers

Plots of the cumulative coordination numbers for Si-O and B-O obtained from MW #1 and MW #2 are shown in **Figure 3.16** below.

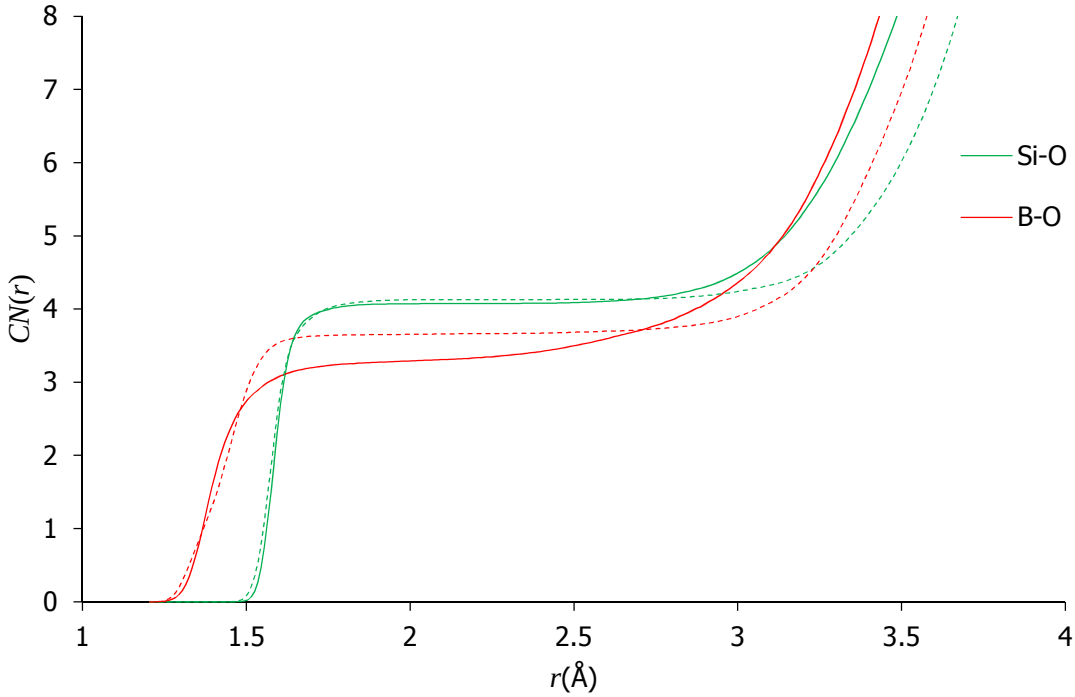

Figure 3.16: B-O and Si-O coordination numbers predicted by MD simulations of MW glass. Solid lines are from MW #1 and dashed lines are from MW #2.

Analysis of the cumulative coordination number functions show that at a distance of 2.0 Å, approximately 29% and 66% of boron atoms were four-coordinated in the MW #1 and MW #2 simulations respectively. In the MW #1 simulation, 92% of silicon atoms were found to be four-coordinated and in the MW #2 simulation, 87% were four-coordinated. The remaining silicon atoms were five-coordinated which is considered unrealistic for SiO_4. A three-body potential to control the O-Si-O bond angle may have been beneficial in both models in order to restrict the Si-O coordination to four.

MW Glass Bond Angle Distributions

The bond angle distributions from the simulations of MW glass are shown in **Figure 3.17** and the average bond angles found in the simulations are reported in **Table 3.15**.

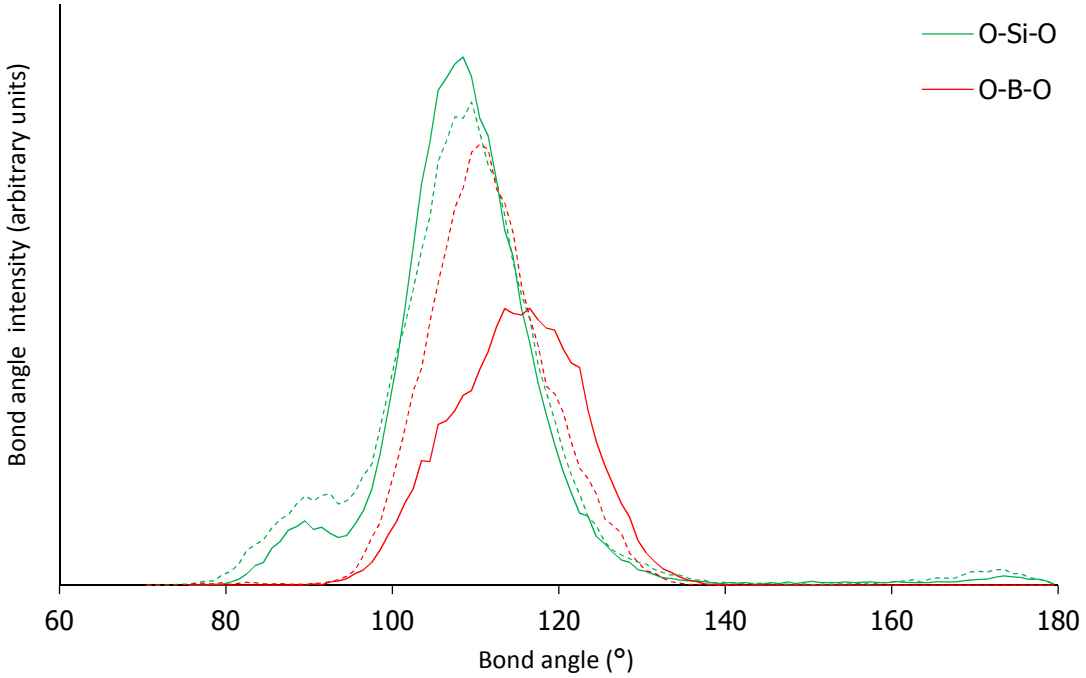

Figure 3.17: Bond angle distributions from simulations of MW glass. Solid lines are from MW #1 and dashed lines are from MW #2.

Table 3.15: Average bond angles from simulations of MW glass (σ is the standard deviation).

Model	<O-Si-O>	<O-B-O>
MW #1	109°	115°
σ	11°	8°
MW #2	109°	112°
σ	13°	8°

The mean O-Si-O bond angle was found to be 109° in both models indicating that the majority of silicon atoms were forming SiO_4 tetrahedral units. The mean O-B-O angles were found to be 115° and 112° in MW #1 and MW #2 respectively. These results are consistent with the coordination number functions shown in **Figure 3.16**.

Network Connectivity Analysis Results

The Q^n analysis results for the MW glass simulations are shown in **Table 3.16** below. Note that 2.7 % of the Si atoms in both models were found to be Q^5 units. Such units are considered to be unrealistic and have therefore been counted as Q^4 units in **Table 3.16**.

Table 3.16: Network connectivity analysis for simulations of MW glass. Uncertainties were derived assuming a counting accuracy of ± 1 atom in each Q^n group.

Model	Network former	Fraction of atoms in Q^n group					Average Q^n
		Q^0	Q^1	Q^2	Q^3	Q^4	
MW #1	Si	2.7 % ± 0.7 %	20.4 ± 0.7 %	23.1 % ± 0.7 %	36.7 % ± 0.7 %	17.1 % ± 0.7 %	2.45
MW #2	Si	4.8 % ± 0.7 %	10.9 % ± 0.7 %	30.6 % ± 0.7 %	32.7 % ± 0.7 %	21.0 % ± 0.7 %	2.68
MW #1	B	33.3 % ± 1.1 %	44.4 % ± 1.1 %	20.0 % ± 1.1 %	2.2 % ± 1.1 %	0.0 % ± 1.1 %	0.91
MW #2	B	17.8 % ± 1.1 %	44.4 % ± 1.1 %	31.1 % ± 1.1 %	5.6 % ± 1.1 %	1.1 % ± 1.1 %	1.28

Table 3.16 shows that the average connectivity is somewhat higher for both silicon and boron in MW #2 than MW #1. This can be attributed to the higher number of five-coordinated silicon and four-coordinated boron atoms in MW #2. To explain this further, **Table 3.17** below shows the coordination number of oxygen atoms with respect to silicon and boron. As an example to assist with interpreting information in **Table 3.17**, it was found in the MW #1 model that 48.9 % (± 0.2 %) of oxygen atoms were connected to one silicon atom.

Table 3.17: Oxygen connectivity analysis for simulations of MW glass.

Model	Network former	Fraction of oxygens with network formers connected			Average number connected
		0 connected	1 connected	2 connected	
MW #1	Si	(13.2 ± 0.2) %	(48.9 ± 0.2) %	(37.9 ± 0.2) %	1.25
MW #2	Si	(12.9 ± 0.2) %	(47.8 ± 0.2) %	(39.3 ± 0.2) %	1.26
MW #1	B	(46.7 ± 0.2) %	(44.8 ± 0.2) %	(8.5 ± 0.2) %	0.62
MW #2	B	(43.5 ± 0.2) %	(44.5 ± 0.2) %	(12.0 ± 0.2) %	0.69

It can be seen from **Table 3.17** that the average O-Si coordination number is marginally higher in MW #2 due to the higher amount of five-coordinated silicon. The average B-O coordination number is higher in MW #2 due to the significantly higher amount of four-coordinated boron. Oxygen atoms connected to two silicon atoms are Si-O-Si bridging oxygens and provide connectivity. **Table 3.17** shows that there is a slightly higher number of Si-O-Si bridging oxygens in MW #2 compared to MW #1 and a significantly higher number of B-O-B bridging oxygens. These effects result in higher average silicon and boron connectivities in MW #2.

3.6 Chapter 3 Discussion

The purpose of the work presented in this Chapter was to establish a set of suitable interatomic potentials for modelling alkali borosilicate glasses used for vitrification. This was carried out by comparing the results of simulations using Buckingham potential parameters provided by Teter [2] ('glass #1') and BHM potentials from the literature [3] ('glass #2'). Comparisons showed little difference in Si-O, B-O and Li-O bond lengths between the glass #1 and glass #2 simulations. There were however more significant differences noticed between Na-O bond lengths and the number of four-coordinated boron atoms. The Na-O distances observed in the glass #1 simulations were closer to the value determined in the MD study of sodium silicate glass by Pota et al [11]. The number of four-coordinated boron atoms is considerably higher in the glass #2 simulations. Comparison between the results of the ABS simulations and experimental data suggest that the number of four-coordinated boron atoms is more realistically reproduced in the glass #2 models (i.e. using BHM potentials).

Overall it is concluded that the Buckingham potential parameters from Teter used to simulate the Si-O, Na-O and Li-O interactions can reproduce structural features with reasonable accuracy. However, it is judged that the Buckingham potential parameters used for the B-O interaction could benefit from further refinement in order to more accurately model boron coordination numbers.

3.7 Chapter 3 References

[1] W. Smith, T. R. Forester and I. T. Todorov, *The DL_POLY Classic User Manual,* vol. 16, Daresbury, United Kingdom: Daresbury Laboratory, 2006, pp. 1911-1918.

[2] D. M. Teter, *Private communication,* 1999.

[3] A. J. Connelly, K. P. Travis, R. J. Hand and N. C. Hyatt, "Composition-structure relationships in simplified nuclear waste glasses: 1. Mixed alkali borosilicate glasses," *J. Am. Ceram. Soc.,* vol. 94, pp. 151-159, 2011.

[4] FIZ Karlsruhe - Leibniz-Insitut für Informationsinfrastruktur GmbH, "Inorganic Crystal Structure Database," Eggenstein-Leopoldshafen.

[5] E. Kashchieva, B. Shivachev and Y. Dimitriev, "Molecular dynamics studies of vitreous boron oxide," *J. Non-Cryst. Solids,* vol. 351, pp. 1158-1161, 2005.

[6] D. L. Perry, Handbook of Inorganic Compunds, London: Boca Raton, Fla. : CRC ; London : Taylor & Francis distributor, 2011.

[7] S. Le Roux and V. Petkov, "ISAACS - interactive structure analysis of amorphous and crystalline systems," *J. Appl. Cryst.,* vol. 43, pp. 181-185, 2010.

[8] A. K. Soper, "Boroxol rings from diffraction data on vitreous boron oxide," *J. Phys: Condens. Mat.,* vol. 23, p. 365402, 2011.

[9] P. A. V. Johnson, A. C. Wright and R. N. Sinclair, "A neutron diffraction investigation of the structure of vitreous boron trioxide," *J. Non-Cryst. Solids,* vol. 50, pp. 281-311, 1982.

[10] R. L. Mozzi and B. E. Warren, "The structure of vitreous boron oxide," *J. Appl. Cryst.,* vol. 3, pp. 251-257, 1970.

[11] M. Pota, A. Pedone, G. Malavasi, C. Durante, M. Cocchi and M. C. Menziani, "Molecular dynamics simulations of sodium silicate glasses: Optimization and limits of the computational procedure," *Comp. Mater. Sci,* vol. 47, pp. 739-751, 2010.

[12] J. Biscoe and B. E. Warren, "X-ray diffraction study of soda-boric oxide glass," *J. Am. Ceram. Soc.,* vol. 21, no. 8, pp. 287-293, 1938.

[13] L. Cormier, S. Creux, L. Galoisy, G. Calas and P. Gaskell, "Medium range order around cations in silicate glasses," *Chem. Geol.,* vol. 128, pp. 77-91, 1996.

[14] M. Fabian, E. Svab, G. Meszaros, Z. Revay, T. Proffen and E. Veress, "Network structure of multi-component sodium borosilicate glasses by neutron diffraction," *J. Non Cryst. Solids,* vol. 353, no. 18-21, pp. 2084-2089, 2007.

[15] J. M. Roderick, D. Holland, A. P. Howes and C. R. Scales, "Density-strcuture relations in mixed alkali borosilicate glasses by Si-29 and B-11 MAS-NMR," *J. Non-Cryst. Solids,* pp. 746-751, 2001.

[16] D. Holland, B. G. Parkinson, M. M. Islam, A. Duddridge, J. M. Roderick, A. P. Howes and C. R. Scales, "NMR inights into wasteforms for the vitrification of high-level nuclear waste," *Appl. Magn. Reson.,* vol. 32, pp. 483-497, 2007.

[17] A. J. Connelly, K. P. Travis, R. J. Hand and N. C. Hyatt, "Composition-Structure Relationships in Simplified Nuclear Waste Glasses: 2. The Effect of ZrO2 Additions," *J. Am. Ceram. Soc.,* vol. 94, no. 1, pp. 78-85, 2011.

4. Experimental Studies of Vitrified Wasteforms

4.1. Samples Studied

In this work, samples of simulated vitrified HLW forms and their base glasses (i.e. glasses with no simulated waste additives) were studied using experimental techniques including Raman spectroscopy, scanning electron microscopy (SEM) and helium pycnometry. The samples were donated by the National Nuclear Laboratory (NNL) Vitrification Test Rig (VTR) at Sellafield.

4.1.1. Base Glass Compositions

As mentioned in **Section 1**, the base glass mixture that is currently used for the vitrification of HLW is an alkali borosilicate glass known as MW-½Li which, according to Harrison [1], has the composition: 63.4 wt. % SiO_2, 22.5 wt. % B_2O_3, 11.4 wt. % Na_2O and 2.74 wt. % Li_2O.

As also mentioned in **Section 1**, a base glass for the incorporation of Post Operational Clean Out (POCO) waste which contains high amounts of insoluble molybdenum, is being developed. The base glass mixture for this experimental wasteform is known as "Ca/Zn-½Li". From the information provided by NNL [2], Ca/Zn-½Li has the nominal composition: 48.7 wt. % SiO_2, 23.9 wt. % B_2O_3, 8.7 wt. % Na_2O, 2.2 wt. % Li_2O, 4.3 wt. % Al_2O_3, 6.1 wt. % CaO and 6.1 wt. % ZnO.

Photographs of MW-½Li and Ca/Zn-½Li glass ingots are shown in **Figure 4.1 (a)** and **(b)** respectively.

(a) **(b)**

Figure 4.1: Photographs of: (a) MW-½Li and (b) Ca/Zn-½Li glass ingots. Note the yellow tint in the MW-½Li glass ingot due to iron impurities.

4.1.2. Simulated Vitrified High Level Wasteforms

Four different simulated vitrified HLW wasteform ingots known as "Low Magnox", "High Magnox", "MW + POCO" and "Ca/Zn + POCO" were provided by NNL. Photographs of the samples provided are shown in **Figure 4.2 (a), (b), (c)** and **(d)**. Compositional data for each sample was also provided and is shown in **Table 4.1** below [3].

"Low Magnox" is composed of MW base glass with a relatively low (when compared with other simulated vitrified wasteforms) mass of simulated waste oxides added. From **Table 4.1** below, Low Magnox is composed of approximately 83 wt. % MW glass and 17 wt. % waste oxides. High Magnox is composed of MW glass with a higher waste loading than Low Magnox glass. From **Table 4.1** below, High Magnox is composed of approximately 64 wt. % MW glass and 36 wt. % waste oxides. MW + POCO is composed of the MW base glass with simulated Post Operational Clean Out (POCO) waste oxides added. **Table 4.1** below shows that MW + POCO is composed of approximately 64 wt. % MW glass and 36 wt. % POCO waste oxides. Ca/Zn + POCO is composed of the Ca/Zn base glass mixture described in **Section 4.1.1** above with simulated POCO waste oxides added. From **Table 4.1** below, Ca/Zn + POCO is composed of approximately 59 wt. % Ca/Zn base glass and 41 wt. % simulated POCO waste oxides.

(a)

(b)

(c)

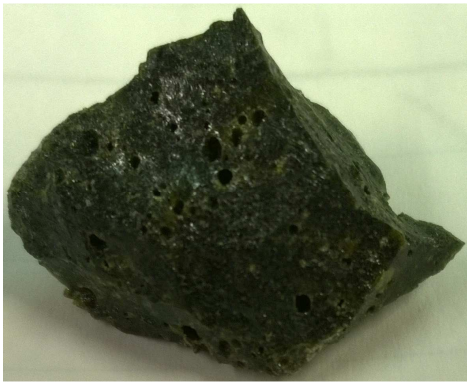

(d)

Figure 4.2: Photographs of: (a) Low Magnox, (b) High Magnox, (c) MW + POCO and Ca/Zn + POCO wasteform ingots.

Table 4.1: Nominal compositions of simulated vitrified waste samples provided by NNL [3].

Oxide	Low Magnox (wt. %)	High Magnox (wt. %)	MW + POCO (wt. %)	Ca/Zn + POCO (wt. %)
Al_2O_3	2.60	7.00	3.90	4.70
BaO	0.26	0.75	0.88	1.60
B_2O_3	18.30	14.00	13.40	14.20
CaO	-	-	-	3.70
CeO_2	0.71	1.70	1.80	1.20
Cr_2O_3	0.43	1.00	0.81	0.58
Cs_2O	0.63	1.60	2.10	1.40
Fe_2O_3	2.10	4.80	3.60	2.40
Gd_2O_3	<0.1	0.19	3.70	1.60
La_2O_3	0.38	0.92	0.94	0.64
Li_2O	3.00	3.30	3.50	2.90
MgO	3.00	7.20	3.90	2.10
MoO_3	0.80	2.30	5.50	11.60
Na_2O	10.30	7.40	8.00	5.30
Nd_2O_3	1.10	2.70	2.80	1.90
NiO	0.28	0.68	0.56	0.35
Pr_2O_3	0.35	0.85	0.88	0.63
RuO_2	0.45	0.99	0.31	0.50
SiO_2	51.70	39.00	38.70	29.00
Sm_2O_3	0.25	0.58	0.66	0.45
SrO	0.18	0.43	0.59	0.55
TeO_2	<0.1	0.25	0.32	0.21
$Y2O_3$	0.12	0.27	0.37	0.25
ZnO	-	-	-	3.70
ZrO_2	0.87	2.20	3.90	6.20
Total [1]	97.80	100.10	101.10	97.70
wt. % Base glass [2]	83.30	63.70	63.60	58.80
wt. % waste oxides	16.70	36.30	36.40	41.20

[1] It is recognised that the compositions provided in **Table 4.1** do not summate to 100 however, other than [3], there is no alternative data source available that provides the compositions of these glasses.

[2] Base glass wt. % quoted includes the total Li_2O content of the simulated wasteform (i.e. Li_2O in the MW-½Li and Ca/Zn-½Li glass mixtures plus simulated HLW feed).

4.2 X-ray Fluorescence Spectroscopy Results

XRF spectroscopy results were obtained using the method described in **Section 2.3.2**. The results are presented in **Table 4.2** below rounded to the nearest whole per cent. Note that compounds with a presence less than 0.5% have not been recorded. It is recognised that the XRF results do not exactly match the nominal compositions provided in **Table 4.1**. This is because the standard options on the XRF analysis software are not suitable for bulk powder samples. Better results would require expertise in calibration and settings of analysis software and such expertise was not easily available. Nevertheless, the qualitative trends in the XRF results can be matched to the quantitative differences in composition shown in **Table 4.1.**

Table 4.2: XRF results.

Oxide	MW-½Li (compound %)	Low Magnox (compound %)	High Magnox (compound %)	MW + POCO (compound %)	Ca/Zn-½Li (compound %)	Ca/Zn + POCO (compound %)
Na_2O	12	10	5	5	6	1
MgO	-	3	7	3		2
Al_2O_3	1	3	8	4	6	4
SiO_2	87	69	46	41	64	30
P_2O_5	-	-	1	1	-	1
CaO	-	-	-	-	11	5
Cr_2O_3	-	1	1	1	-	1
Fe_2O_3	-	4	8	5	-	4
NiO	-	1	1	1	-	1
ZnO	-	-	-		12	6
SrO	-	-	1	1	-	1
Y_2O_3	-	-	-	1	-	-
ZrO_2	-	2	6	10	-	14
MoO_3	-	1	5	11	-	22
RuO_2	-	1	1	-	-	-
Cs_2O	-	1	2	2	-	2
BaO	-	-	-	1	-	2
La_2O_3	-	-	1	1	-	-
CeO_2	-	1	2	2	-	1
Pr_2O_3	-	1	-	-	-	-
Nd_2O_3	-	2	4	4	-	2
Gd_2O_3	-	-		4	-	2
Total	**100**	**100**	**99**	**98**	**99**	**101**

Note that only compounds with presence ≥ 0.5 % have been recorded.

4.3 Helium Pycnometry and Density Determination

In order to create MD models of simulated vitrified wasteforms, it was necessary to determine the density of each wasteform. The volume of each simulated wasteform sample was determined using the method described in **Section 2.2.2** and the mass of each sample was measured using a top pan balance. The density of each sample was then calculated and the results are shown in **Table 4.3** below.

Table 4.3: Experimentally determined densities of the four simulated wasteforms described Section 4.1.

Sample	Volume (cm^{-3})	Mass (g)	Density ($g \cdot cm^{-3}$)
Low Magnox	4.100 ± 0.006	10.660 ± 0.003	2.600 ± 0.004
High Magnox	1.552 ± 0.011	5.049 ± 0.002	3.253 ± 0.042
MW+POCO	3.579 ± 0.011	10.606 ± 0.001	2.963 ± 0.013
Ca/Zn+POCO	2.119 ± 0.008	6.576 ± 0.001	3.103 ± 0.012

4.4 Scanning Electron Microscopy Imaging

Backscattered electron (BSE) and secondary electron (SE) images of the simulated vitrified wasteforms described in **Section 4.1.2** were obtained using the method outlined in **Section 2.4.6**.

4.4.1 Low Magnox SEM Images

Figures 4.3-**4.6** below show SEM images of a small (mm size) sample of Low Magnox glass. All figures were taken with an accelerating voltage of 20 kV. **Figures 4.3** and **4.4** were taken at low magnification to provide millimetre scale SE and BSE SEM images of the sample, whereas **Figures 4.5** and **4.6** were taken at greater magnification and show evidence of phase separation in the glass.

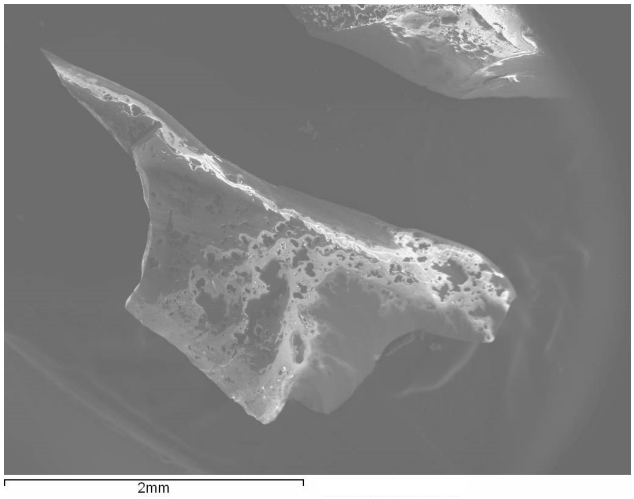

Figure 4.3: SE SEM image of a Low Magnox sample (taken with a sample chamber pressure of <1 Pa).

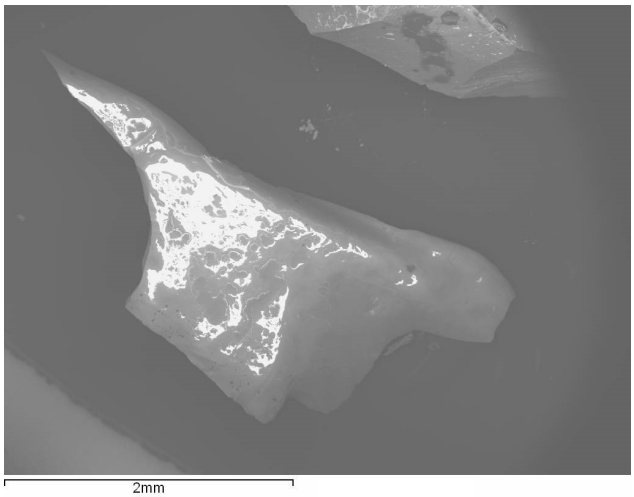

Figure 4.4: BSE SEM image of a Low Magnox sample (taken with a sample chamber pressure of <1 Pa).

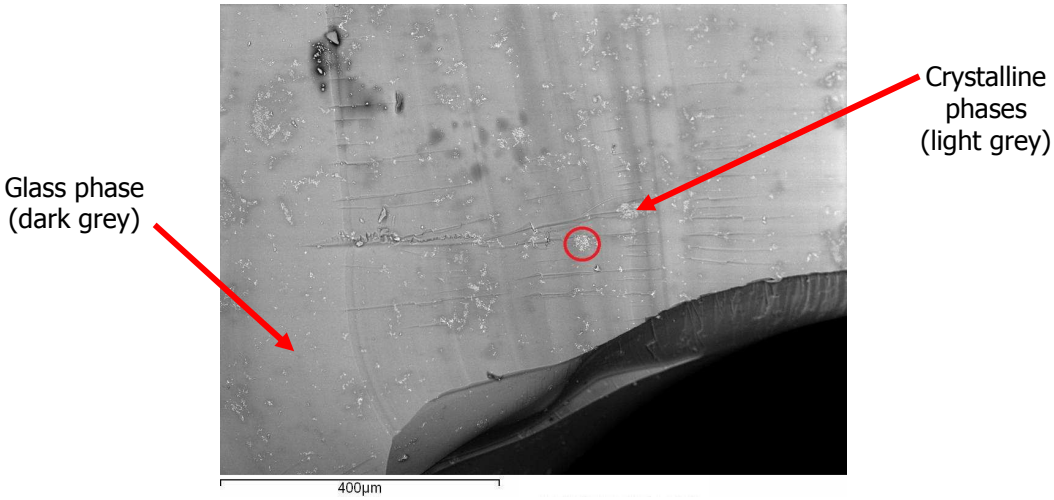

Figure 4.5: BSE SEM image of a Low Magnox sample showing crystalline inclusions (taken with a sample chamber pressure of 25 Pa). The area circled is shown at greater magnification in Figure 4.6.

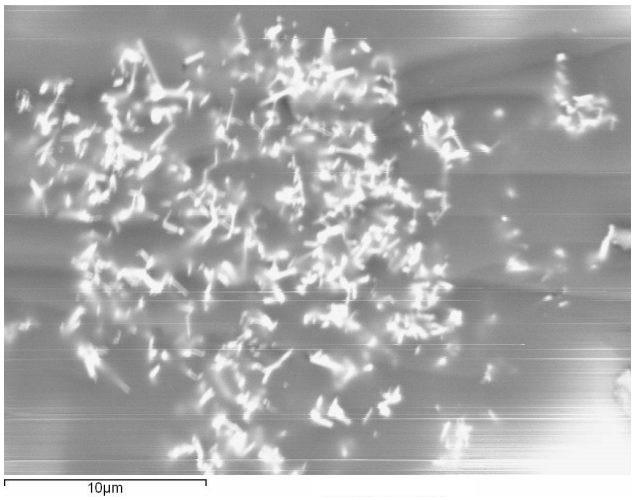

Figure 4.6: BSE SEM image of crystalline phases in Low Magnox (taken with a sample chamber pressure of 25 Pa). Note that image quality is affected by charge build-up.

4.4.2 High Magnox SEM Images

Figures 4.7-4.10 below show SEM images of a High Magnox glass sample using a 20 kV accelerating voltage. **Figures 4.7** and **4.8** were taken at low magnification to provide millimetre scale SE and BSE images of the sample. **Figures 4.9** and **4.10** were taken at greater magnification and show evidence of phase separation.

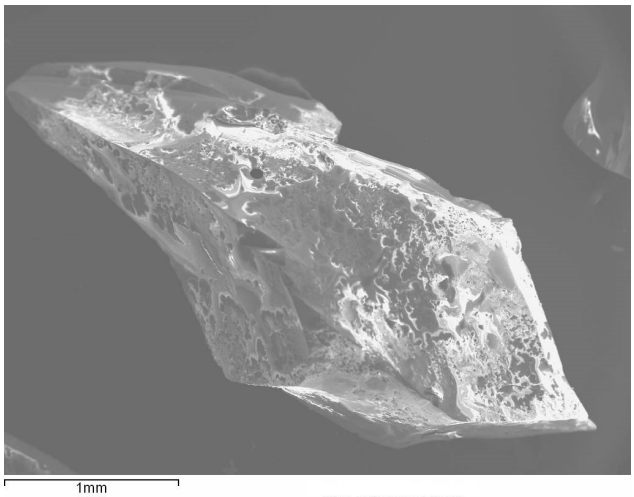

Figure 4.7: SE SEM image of a High Magnox sample (taken with a sample chamber pressure of <1 Pa).

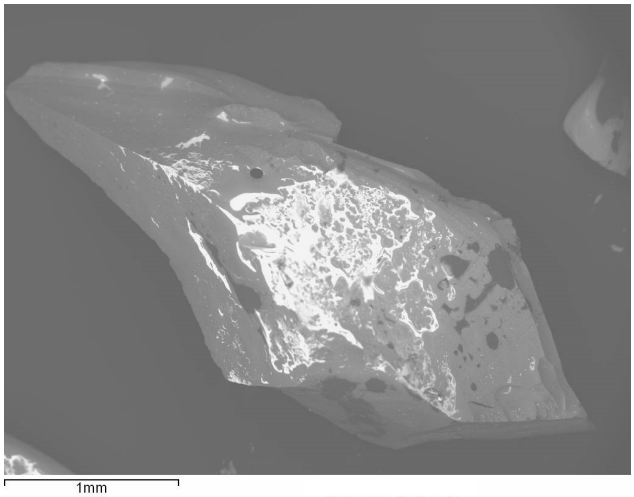

Figure 4.8: BSE SEM image of a High Magnox sample (taken with a sample chamber pressure of <1 Pa).

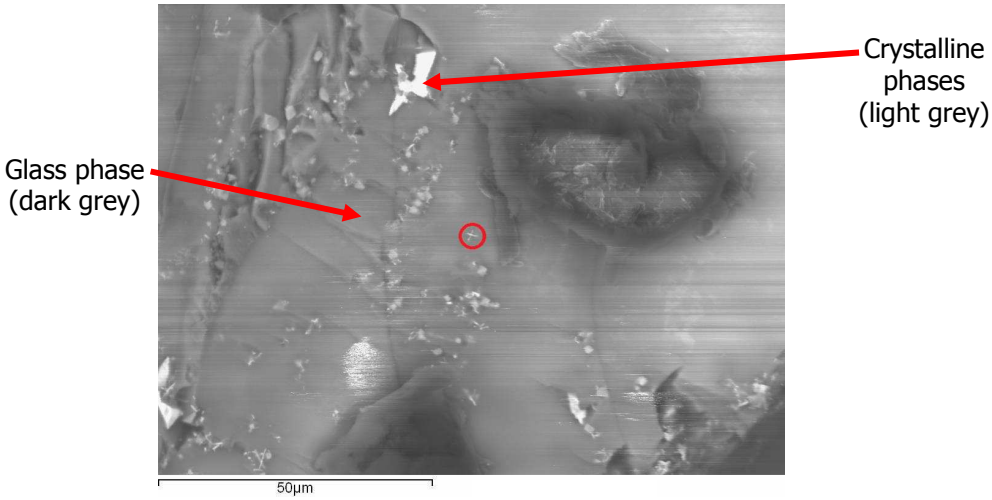

Figure 4.9: BSE SEM image of a High Magnox sample showing crystalline inclusions (taken with a sample chamber pressure of 25 Pa). The area circled is shown at greater magnification in Figure 4.10.

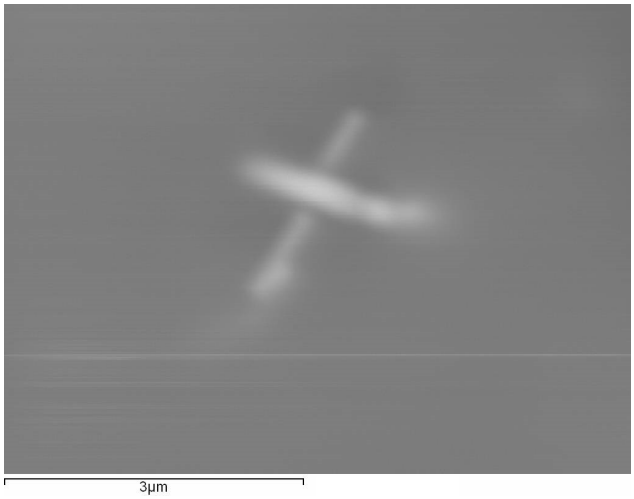

Figure 4.10: BSE SEM image of crystalline phases in High Magnox (taken with a sample chamber pressure of 25 Pa).

4.4.3 MW+ POCO SEM Images

As for Low and High Magnox, **Figures 4.11-4.13** below show SEM images of a mm size sample of MW + POCO. All figures were taken with an accelerating voltage of 20 kV. **Figures 4.11** and **4.12** were taken at low magnification to provide millimetre scale SE and BSE SEM images of the sample. **Figure 4.13** was taken at greater magnification and shows evidence of phase separation.

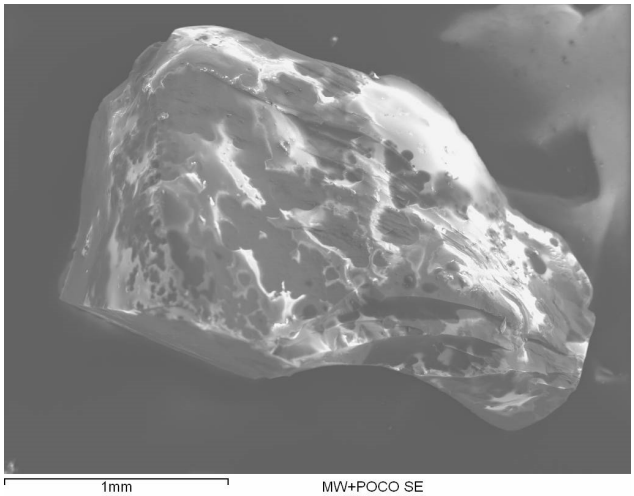

Figure 4.11: SE SEM image of a MW + POCO sample (taken with a sample chamber pressure of <1 Pa).

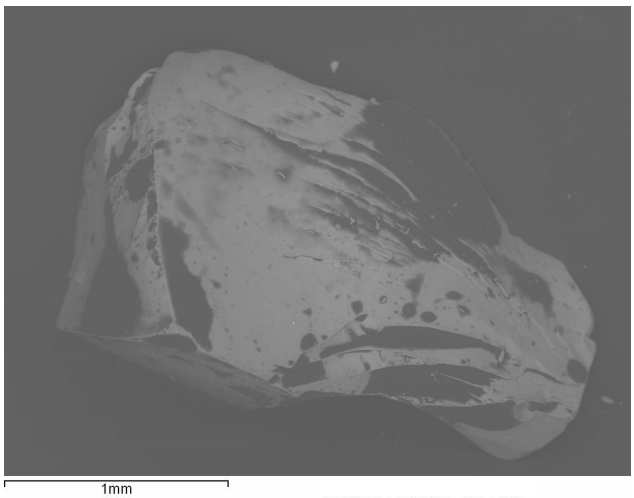

Figure 4.12: BSE SEM image of a MW+POCO sample (taken with a sample chamber pressure of 25 Pa).

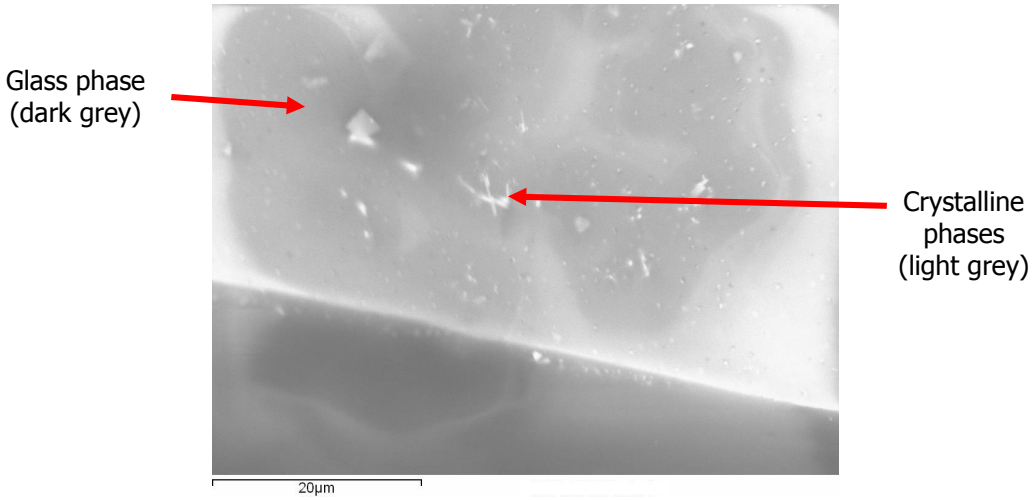

Figure 4.13: BSE SEM image of a MW + POCO sample showing crystalline inclusions (taken with a sample chamber pressure of 25 Pa).

4.4.4 Ca/Zn + POCO SEM Images

Similarly for Low Magnox, High Magnox and MW + POCO, **Figures 4.14–4.16** below show SEM images from a Ca/Zn + POCO sample. All figures were taken with an accelerating voltage of 20 kV. **Figures 4.14** and **4.15** were taken at low magnification to provide millimetre scale SE and BSE images of the sample. **Figure 4.16** was taken at greater magnification and clearly shows evidence of phase separation.

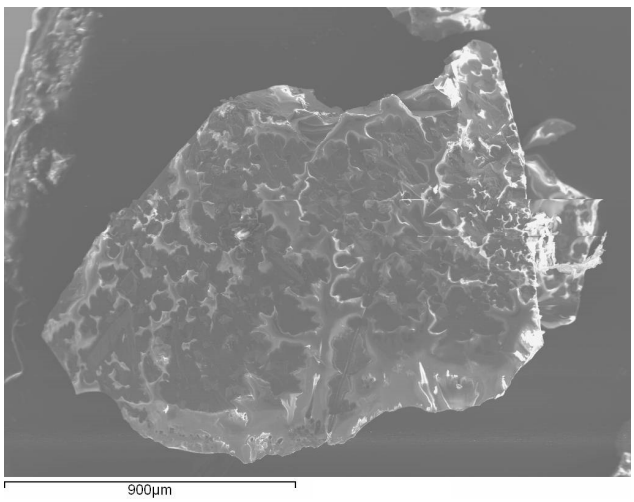

Figure 4.14: SE SEM image of a Ca/Zn + POCO sample (taken with a sample chamber pressure of <1 Pa).

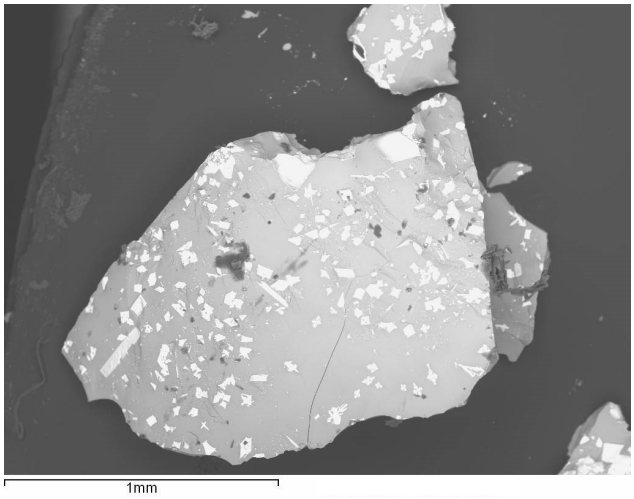

Figure 4.15: BSE SEM image of a Ca/Zn + POCO sample (taken with a sample chamber pressure of 25 Pa).

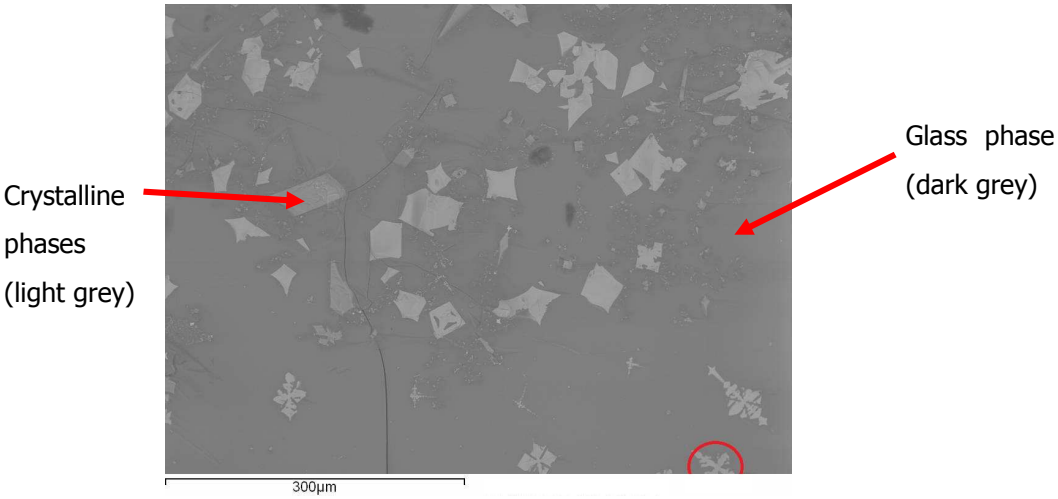

Figure 4.16: BSE SEM image of a Ca/Zn + POCO sample showing crystalline inclusions (taken with a sample chamber pressure of 25 Pa).

4.5 Energy Dispersive X-ray Spectroscopy Results

Energy Dispersive X-ray (EDX) spectra from the simulated vitrified wasteform samples were obtained as described in **Section 2.4.6**.

4.5.1 Glass Phase EDX Results

For the glass phases, EDX spectral data were obtained from at least three different locations which were believed to be amorphous regions in each sample (see images in **Section 4.4** for examples). The average per cent composition was then reported for each oxide species. The results are presented in **Table 4.4** below. Note that the results are rounded to the nearest whole per cent and compounds with a presence of less than 0.5 % have not been recorded.

Table 4.4: EDX results from glass phases. Note that only compounds with presence ≥ 0.5 % have been recorded in this table.

Oxide	MW-½Li (compound %)	Low Magnox (compound %)	High Magnox (compound %)	MW + POCO (compound %)	Ca/Zn-½Li (compound %)	Ca/Zn + POCO (compound %)
Na_2O	15	13	11	14	12	11
MgO	-	4	9	6	-	4
Al_2O_3	-	3	8	5	6	7
SiO_2	85	74	53	49	67	50
CaO	-	-	-	-	8	2
Cr_2O_3	-	-	1	-	-	1
Fe_2O_3	-	3	4	3	-	3
ZnO	-	-	-	-	7	4
ZrO_2	-	-	4	6	-	6
MoO_3	-	-	3	7	-	2
RuO_2/ Ru_2O_3	-	3	-	-	-	1
Cs_2O	-	-	3	2	-	3
BaO	-	-	-	-	-	1
CeO_2/ Ce_2O_3	-	-	-	2	-	1
Nd_2O_3	-	-	4	2	-	2
Gd_2O_3	-	-	-	4	-	2
Total	**100**	**100**	**100**	**100**	**100**	**100**

4.5.2 Low Magnox Crystalline Phase EDX Results

EDX data was obtained for the crystalline phases shown in **Figure 4.17** and **Figure 4.18** below. The EDX results for these phases are shown in **Table 4.5**.

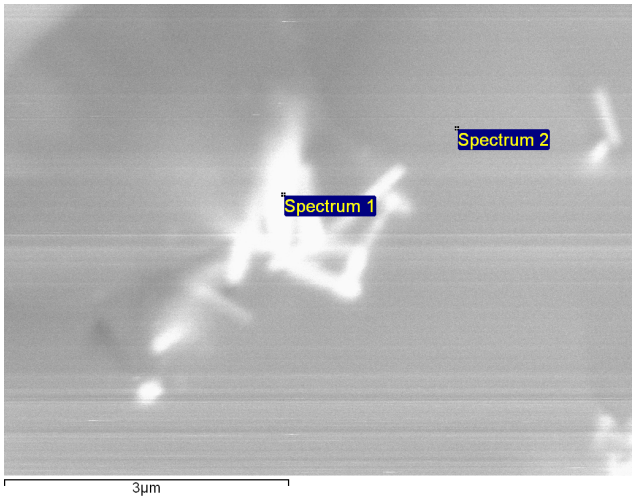

Figure 4.17: BSE SEM images of Low Magnox showing locations at which EDX data were taken.

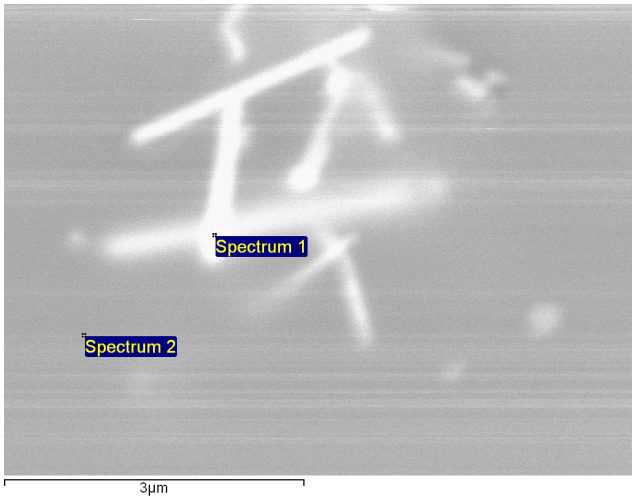

Figure 4.18: BSE SEM images of Low Magnox showing locations at which EDX data were taken.

Table 4.5: EDX results from crystalline phases in Low Magnox.

Oxide	Spectrum 1 **Figure 4.17** (compound %)	Spectrum 1 **Figure 4.18** (compound %)
Na_2O	8	10
MgO	2	3
Al_2O_3	2	2
SiO_2	43	48
Cr_2O_3	1	1
Fe_2O_3	2	2
RuO_2/Ru_2O_3	42	34
Total	**100**	**100**

The spectra obtained from the locations designated Spectrum 2 in **Figure 4.17** and Spectrum 2 in **Figure 4.18** were consistent with those of glass phases. The data in **Table 4.5** suggests that the phases shown in **Figures 4.17** and **4.18** are crystals consisting mainly of RuO_2/Ru_2O_3 (SiO_2 is assumed to be from the surrounding glass phase).

4.5.3 High Magnox Crystalline Phase EDX Results

EDX data was obtained for the crystalline phases shown in **Figure 4.19** and **Figure 4.20** below. The EDX results for these phases are shown in **Table 4.6**.

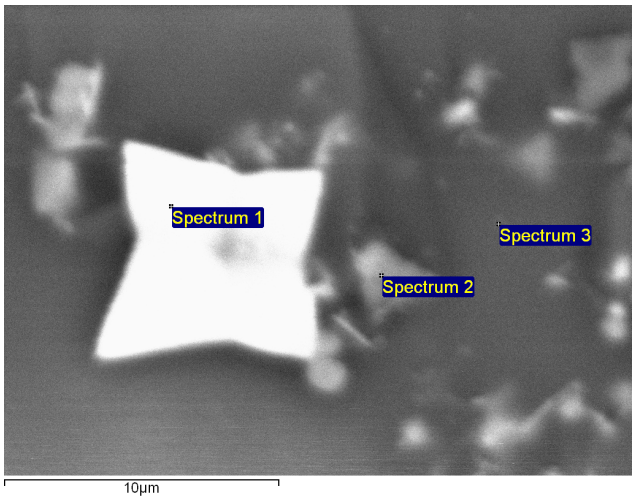

Figure 4.19: BSE SEM images of High Magnox showing locations at which EDX data were taken.

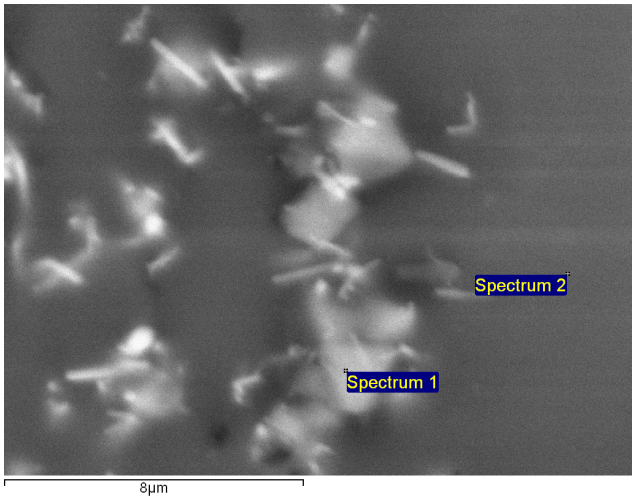

Figure 4.20: BSE SEM images of High Magnox showing locations at which EDX data were taken.

Table 4.6: EDX results from crystalline phases in High Magnox.

Oxide	Spectrum 1 **Figure 4.19** (compound %)	Spectrum 2 **Figure 4.19** (compound %)	Spectrum 1 **Figure 4.20** (compound %)
Na_2O	-	4	3
MgO	1	8	11
Al_2O_3	1	4	4
SiO_2	5	19	9
Cr_2O_3	-	22	22
Fe_2O_3	-	28	34
NiO	-	12	15
ZrO_2	12	-	-
RuO_2/Ru_2O_3	-	2	2
Cs_2O	-	1	-
CeO_2/Ce_2O_3	81	-	-
Total	**100**	**100**	**100**

The spectra from the sites designated Spectrum 3 in **Figure 4.19** and Spectrum 2 in **Figure 4.20** are consistent with those from glass phases. From the data in **Table 4.6** it can be deduced that the relatively large polygon-shaped phase observed in **Figure 4.19** is made up of CeO_2 and ZrO_2. Spectrum 2 from **Figure** 4.19 and Spectrum 1 from **Figure 4.20** show evidence of iron and chromium phases. These results are consistent with the findings of Short [4] who also found evidence of Ce/Zr and $(Mg,Ni)(Fe,Al,Cr)_2O_4$ phase separation in UK vitrified HLW.

4.5.4 MW + POCO Crystalline Phase EDX Results

EDX data was obtained for the crystalline phase shown in **Figure 4.21** below. The EDX results for this phase are presented in **Table 4.7**.

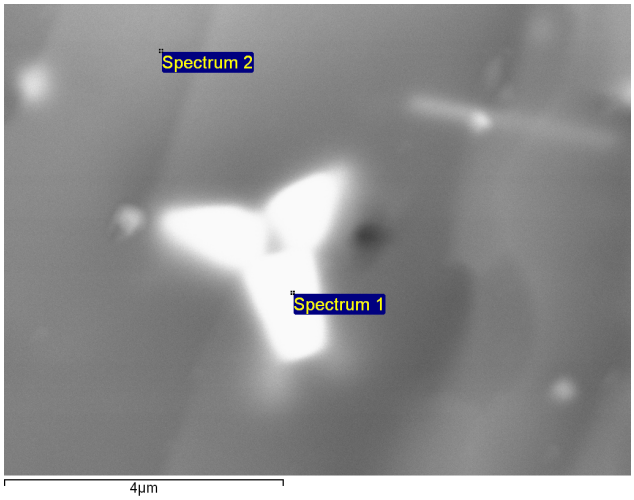

Figure 4.21: BSE SEM image of MW + POCO glass showing a location at which EDX data was taken.

Table 4.7: EDX results from crystalline phases in MW + POCO glass.

Oxide	Spectrum 1 **Figure 4.21** (compound %)
Na_2O	3
MgO	2
Al_2O_3	1
SiO_2	15
Fe_2O_3	1
ZrO_2	15
CeO_2 / Ce_2O_3	53
Gd_2O_3	10
Total	**100**

The spectrum from the site designated Spectrum 2 in **Figure 4.21** is consistent with that of glass phases. The data in **Table 4.7** provides evidence of Ce, Zr and Gd phase separation. This result is consistent with Short [4] who reported evidence of Ce combining with Zr and rare earth elements to form separate phases in UK vitrified HLW. Note that Gd was not present in the Low or High Magnox wasteforms.

4.5.5 Ca/Zn + POCO Crystalline Phase EDX Results

EDX data was obtained for the crystalline phase shown in **Figure 4.22** and **Figure 4.23** below. The EDX results for these phases are shown in **Table 4.8**.

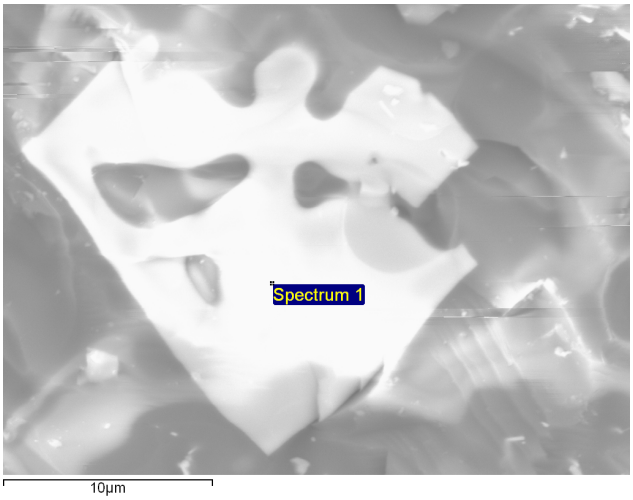

Figure 4.22: BSE SEM image of Ca/Zn + POCO glass showing location at which EDX data were taken.

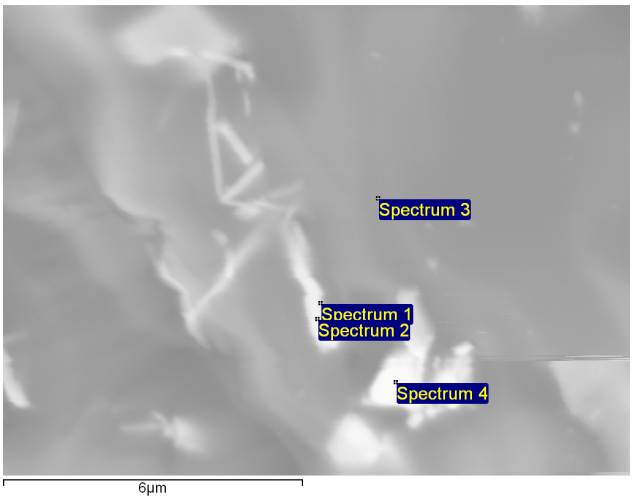

Figure 4.23: BSE SEM image of Ca/Zn + POCO glass showing locations at which EDX data were taken.

Table 4.8: EDX results from crystalline phases in Ca/Zn + POCO glass.

Oxide	Spectrum 1 **Figure 4.22** (compound %)	Spectrum 2 **Figure 4.23** (compound %)	Spectrum 4 **Figure 4.23** (compound %)
Na_2O	1	7	7
MgO	-	3	2
Al_2O_3	-	5	4
SiO_2	-	32	23
CaO	15	2	1
Cr_2O_3	-	-	1
Fe_2O_3	-	2	1
ZnO	-	3	2
SrO	2	-	-
ZrO_2	-	4	-
MoO_3	76	-	-
RuO_2/Ru_2O_3	-	38	60
Cs_2O	-	2	-
Nd_2O_3	4	-	-
Gd_2O_3	2	2	-
Total	**100**	**100**	**100**

From the data in **Table 4.8** it can be deduced that the relatively large phase in depicted in **Figure 4.22** is a $CaMoO_4$ crystalline phase. The relatively smaller, thinner phases shown in **Figure 4.23** appear to consist of RuO_2/Ru_2O_3.

4.5.6 EDX Results Summary

A summary of the phases found from SEM EDX are presented in **Table 4.9** below. The results show evidence of spinel [$(Mg,Ni)(Fe,Al,Cr)_2O_4$], Ru, Ce/Zr and Ce/Gd phase formation in wasteforms based on MW glass. Evidence of Ru and $CaMoO_4$ were found in the wasteform based on the Ca/Zn glass. These results are consistent with those reported by Short [4].

Table 4.9: Summary of EDX results.

	Wasteforms			
	Low Magnox	High Magnox	MW+POCO	Ca/Zn+POCO
Base glass				
MW	✓	✓	✓	
Ca/Zn				✓
Crystal phases				
$(Mg,Ni)(Fe,Al,Cr)_2O_4$		✓		
RuO_2/Ru_2O_3	✓			✓
Ce/Zr		✓	✓	
Ce/Gd			✓	
$CaMoO_4$				✓

4.6 Raman Spectroscopy Results

Raman spectra were obtained for the base glasses and simulated vitrified wasteform samples described in **Section 4.1** using the method described in **Section 2.5.4**.

The Raman spectra acquired from the MW-½Li and Ca/Zn-½Li base glass compositions were then compared with the Raman spectra of glasses with similar compositions to found in the literature.

The Raman spectra from the simulated vitrified wasteform samples (i.e. Low Magnox, High Magnox, MW + POCO and Ca/Zn + POCO) were compared with the spectra from the base glass compositions (MW-½Li and Ca/Zn-½Li).

Raman spectra of crystalline materials found in the SEM EDX experiments (see **Table 4.9**) and of glasses with compositions similar to those of the vitrified wasteforms, were obtained from the literature. The spectra from these materials were also compared with the spectra from the simulated vitrified wasteform samples.

4.6.1 Base Glass Raman Spectroscopy Results

Table 4.10 lists the peaks of the bands observed in each of the Raman spectra acquired in this work and those obtained from the literature used for comparison purposes.

The Raman spectra obtained from the MW-½Li and Ca/Zn-½Li base glass compositions are shown in **Figure 4.24** below along with digitised Raman spectra of alkali borosilicate glasses obtained from the literature. The curve designated "MW" in **Figure 4.24** shows the spectrum from a previous study of MW glass by Parkinson et al. [5] where MW glass has the composition 60.6 mol % SiO_2, 18.6 mol % B_2O_3, 10.53 mol % Na_2O and 10.29 mol % Li_2O (i.e. a glass with a lithium content approximately twice that of MW-½Li). The curve designated "6NBS" in **Figure 4.24** is the Raman spectra from a glass with composition 60 mol % SiO_2, 20 mol % B_2O_3 and 20 mol % Na_2O obtained by Osipov et al. [6]. This data was selected as it has a similar silicon, boron and alkali oxide content to MW-½Li.

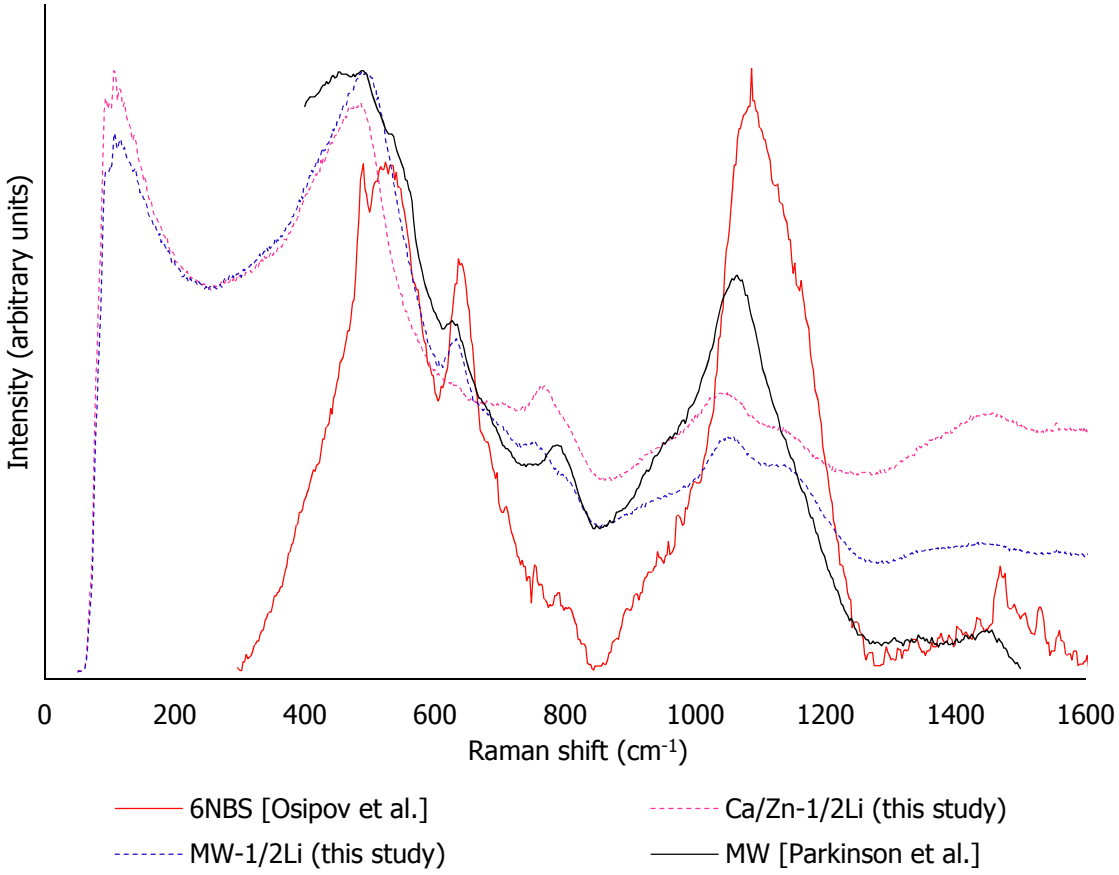

Figure 4.24: Raman spectra of MW-½Li, Ca/Zn-½Li, 6NBS [6] and MW glass [5].

From the data provided in **Table 4.10**, the bands in the Raman spectra obtained from both MW-½Li and Ca/Zn-½Li in this study are generally consistent with the bands observed by Parkinson et al. [5] for MW. The only major exception to this is the position of the peak observed between the range 750–800 cm^{-1} which appears at 754, 767 and 750 cm^{-1} for MW-½Li, Ca/Zn-½Li and 6NBS respectively and at 791 cm^{-1} for MW observed by Parkinson et al. [5]. Overall, it is considered that the Raman spectra acquired from MW-½Li and Ca/Zn-½Li in this study are consistent with the spectra obtained from glasses of similar composition from the literature.

Table 4.10: Raman spectra band peaks obtained from this study and the literature.

Sample / data	300–399 (cm^{-1})	400–599 (cm^{-1})	600–699 (cm^{-1})	700–899 (cm^{-1})	900–999 (cm^{-1})	1000–1099 (cm^{-1})	1100–1199 (cm^{-1})	1200–1399 (cm^{-1})	1400–1600 (cm^{-1})
MW-½Li	-	488	632	754	-	1058	1137	-	1434
Low Magnox	328	486	627	774	944	1040	-	1226	-
High Magnox	319	472	679	-	924	1024	-	1230	1330
MW+ POCO									
Ca/Zn-½Li	-	486	627	767	-	1050	1128	-	1451
Ca/Zn + POCO									
MW [5]	-	489	626	791	-	1061	-	-	-
6NBS [6]	-	520	635	750	940	1085	1150		1475

4.6.2 Low and High Magnox Raman Spectroscopy Results

The Raman spectra obtained from Low and High Magnox are compared with the base glass composition MW-½Li in **Figure 4.25** below.

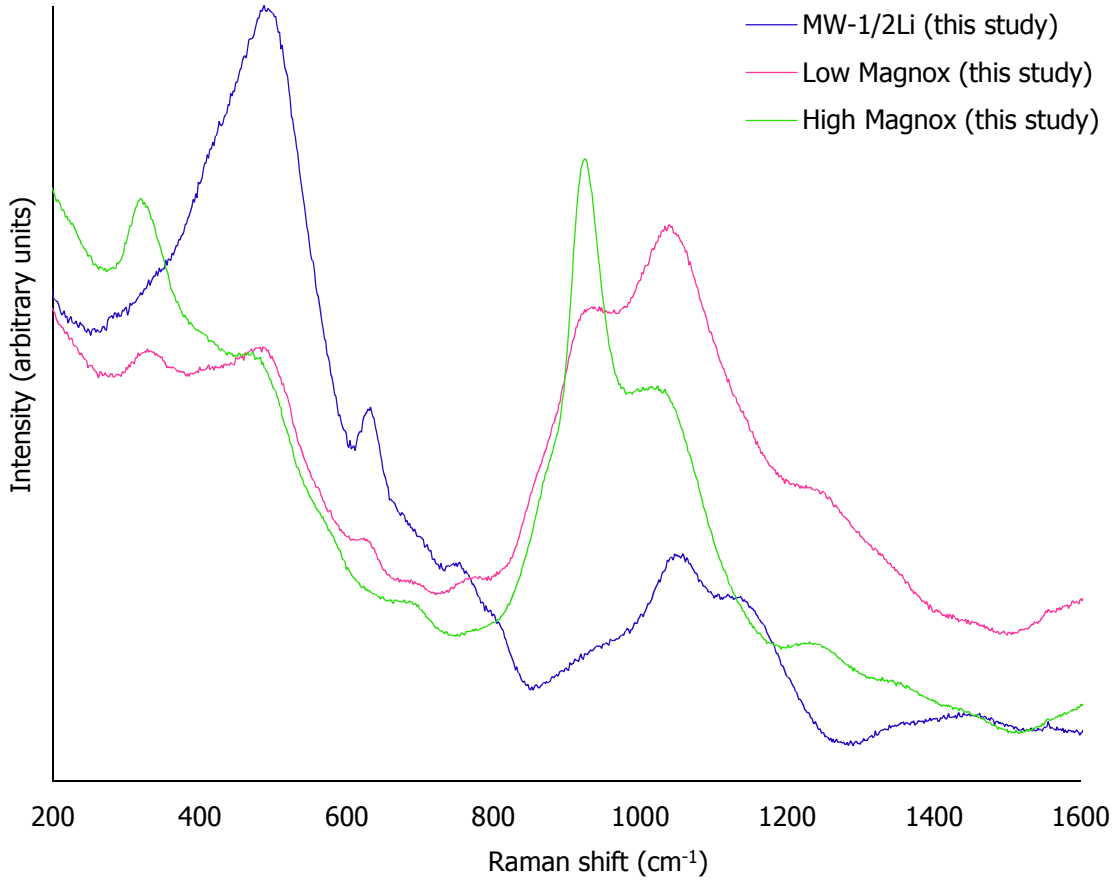

Figure 4.25: Raman spectra of MW-½Li, Low Magnox and High Magnox.

From observation of **Figure 4.25** and the data provided in **Table 4.10**, both Low Magnox and High Magnox have peaks in their Raman spectra at similar positions to MW-½Li. As expected, there are clearly bands present in the Low and High Magnox spectra that are not present in the MW-½Li spectra due to the presence of simulated waste elements.

The two most prominent bands that can be seen in Low and High Magnox but not in MW-½Li occur in the regions 320–300 cm^{-1} and 920–945 cm^{-1}. From the XRF and EDX results reported in **Sections 4.2** and **4.5**, both Low and High Magnox both contain molybdenum and neodymium, it was therefore considered

appropriate to obtain Raman spectra from alkali borosilicate glasses containing molybdenum and neodymium from the literature.

A recent study by Chouard et al. [7] shows the Raman spectra from a soda-lime aluminoborosilicate glass containing Mo (designated Mo glass), with composition 57.95 mol % SiO_2, 10.45 mol % B_2O_3, 5.11 mol % Al_2O_3, 16.49 mol % Na_2O, 8.40 mol % CaO and 1.61 mol % MoO_3 [‡]. Spectra from Mo glass and those from Low and High Magnox are shown in **Figure 4.26**.

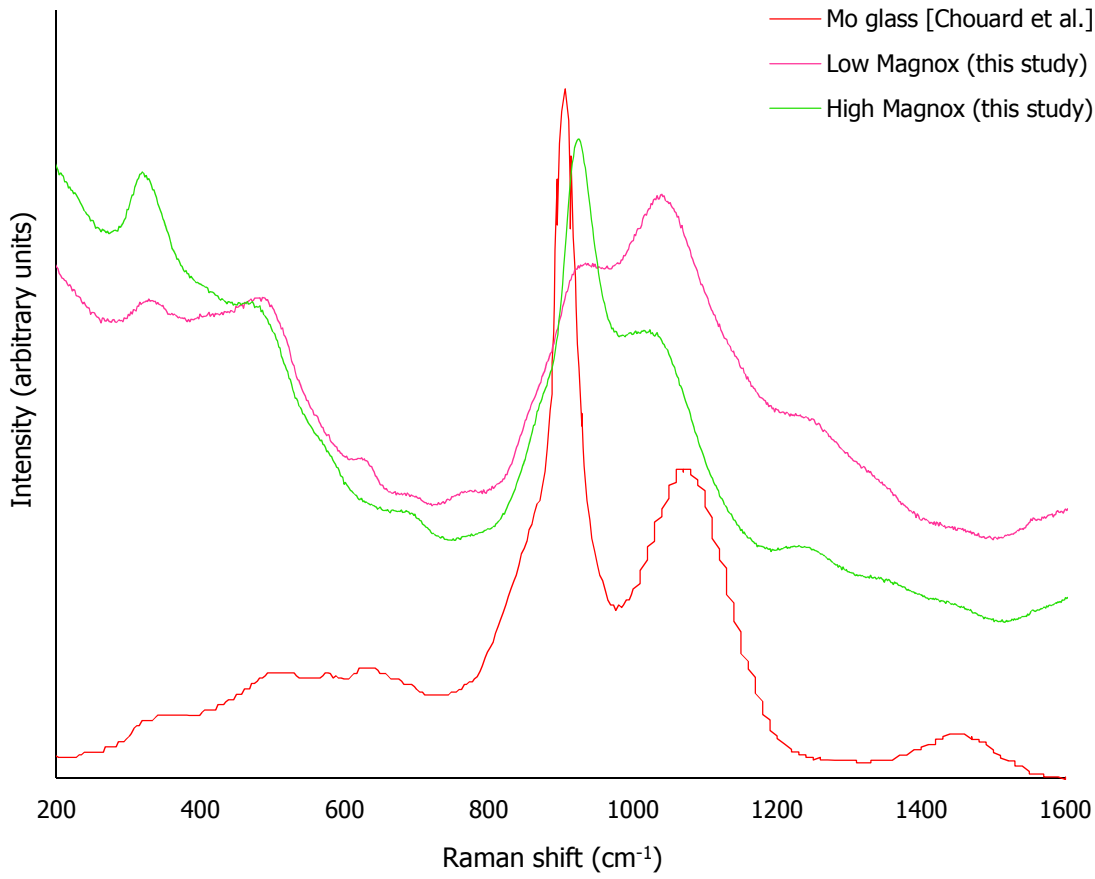

Figure 4.26: Raman spectra of Low Magnox and High Magnox with the spectrum of a soda-lime aluminosilicate glass containing Mo [7].

[‡] It is recognised that the total mol % value exceeds 100.00 however, this data has been taken directly from [7].

According to Chouard et al. [7], the peak observed between 905 – 910 cm^{-1} in the spectrum from Mo glass are due symmetric stretching of MoO_4 tetrahedra in a glassy environment. The spectra from Low and High Magnox have peaks at similar values, yet these peaks are not present in either MW-½Li or Ca/Zn-½Li. It is therefore considered reasonable to conclude that MoO_4 tetrahedra exist in a glass environment in the Low and High Magnox samples. Chouard et al. [7] also tell us that the bands found in the Mo glass spectrum between 1040–1070 cm^{-1} and 1430–1450 cm^{-1} are due to the presence of SiO_4 tetrahedra. Bands at similar positions can be seen in the spectra from MW-½Li, Ca/Zn-½Li, Low Magnox and High Magnox.

4.6.3 MW + POCO Raman Spectroscopy Results

Figure 4.27 below shows the spectra obtained from MW-½Li glass and MW + POCO.

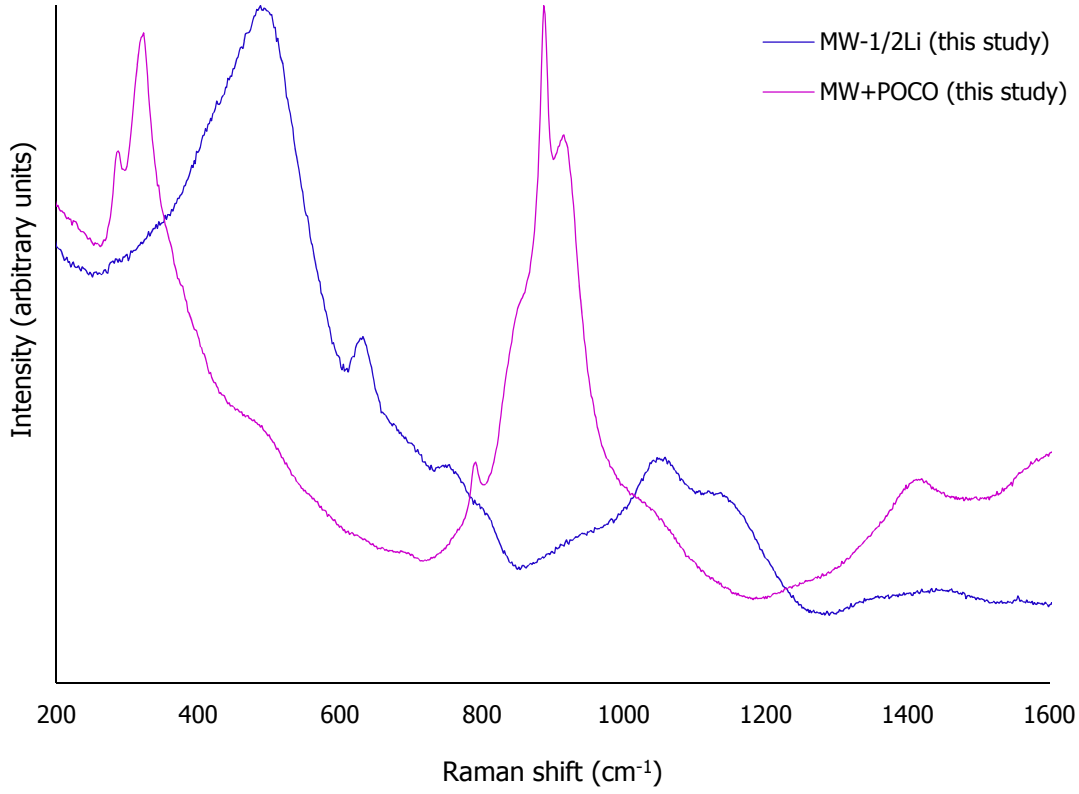

Figure 4.27: Raman spectra of MW-½Li and MW + POCO.

From **Figure 4.27** it can be seen that the spectrum from MW + POCO contains a number of narrow bands that are not present in MW-½Li. Since narrow bands are typical of crystalline materials, it was considered appropriate to compare the spectra from MW + POCO with spectra of crystalline phases expected to be found in the glasses.

It is well known that the presence of Mo in alkali borosilicate glasses gives rise to the formation of alkali molybdate phases such as Na_2MoO_4 (a component of yellow phase) [4, 8]. Since MW + POCO contains a relatively high amount of Mo, it was considered appropriate to compare the Raman spectrum of Na_2MoO_4 with that of MW + POCO.

The Raman spectrum from crystalline Na_2MoO_4 was acquired from the study by Chouard et al. [7] (the same study that provided the spectra for Mo glass described above). The Raman spectra of Na_2MoO_4 and MW + POCO over the range 200-1200 cm^{-1} are shown in **Figure 4.28** below.

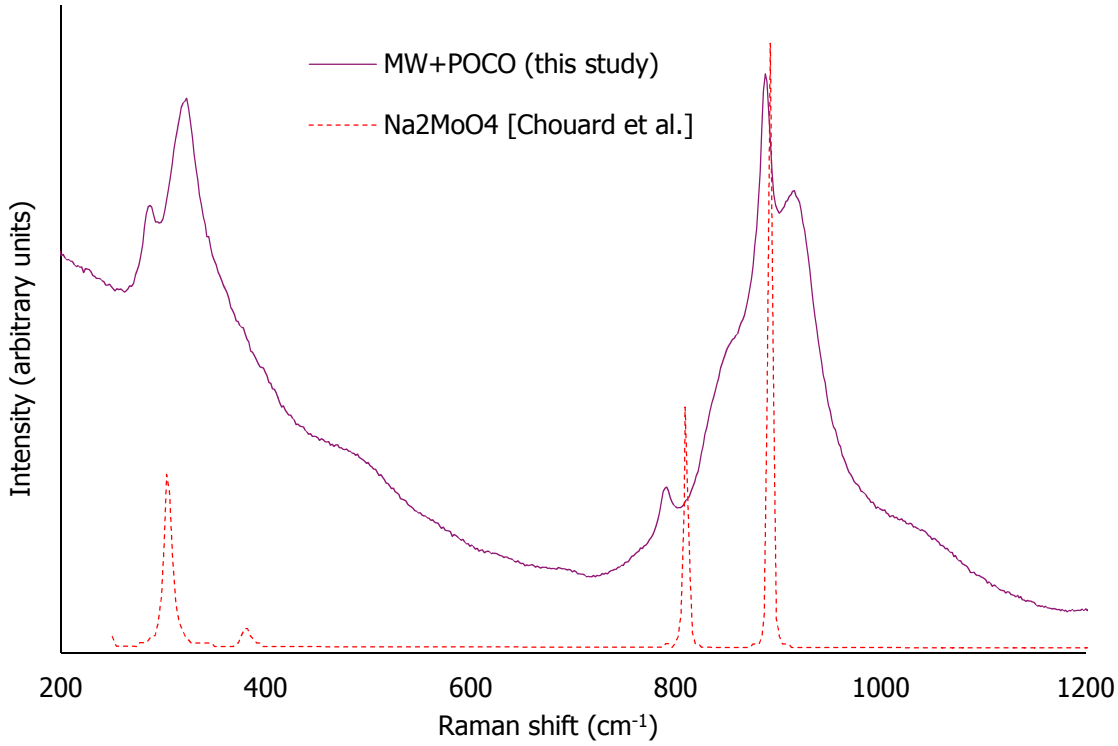

Figure 4.28: Raman spectra of MW + POCO and Na_2MoO_4 [7].

According to Luz-Lima et al. [9], the peaks in the bands of the Na_2MoO_4 spectrum occur at 305, 383, 811 and 894 cm^{-1} (which is consistent with the spectrum of Na_2MoO_4 acquired from Chouard et al. [7]), and are respectively due to the symmetric bending, asymmetric bending, asymmetric stretching and symmetric stretching of MoO_4 tetrahedra.

The Raman spectrum from MW + POCO contains bands with peaks at 287, 320, 791, 887, 912 and 1412 cm^{-1}. It is considered plausible that the peaks occurring at 287, 791 and 887 cm^{-1} in the spectrum from MW + POCO are due to the presence of Na_2MoO_4 phases in the glass. These bands are slightly broader and red shifted to lower values of wavenumber (higher wavelength) when compared to crystalline Na_2MoO_4. A study on the environment of molybdenum in vitrified nuclear wasteforms by Short et al [10] suggests that charge balancing of MoO_4 tetrahedra may be carried out by relatively heavy elements such as lanthanides. It is therefore suggested that both the broadening and shifting of the MoO_4 bands in **Figure 4.28** might be due to the presence of lanthanides (e.g. Gd and Nd) and that this may indicate the presence of phases such as $Na(Nd,Gd)(MoO_4)_2$.

It was also expected that due to its Mo content, MW + POCO would contain MoO_4 in a glass environment as found in the Low and High Magnox samples. The Raman spectrum of Mo glass acquired from Chouard et al. [7] is compared with the spectrum from MW + POCO in **Figure 4.29** below.

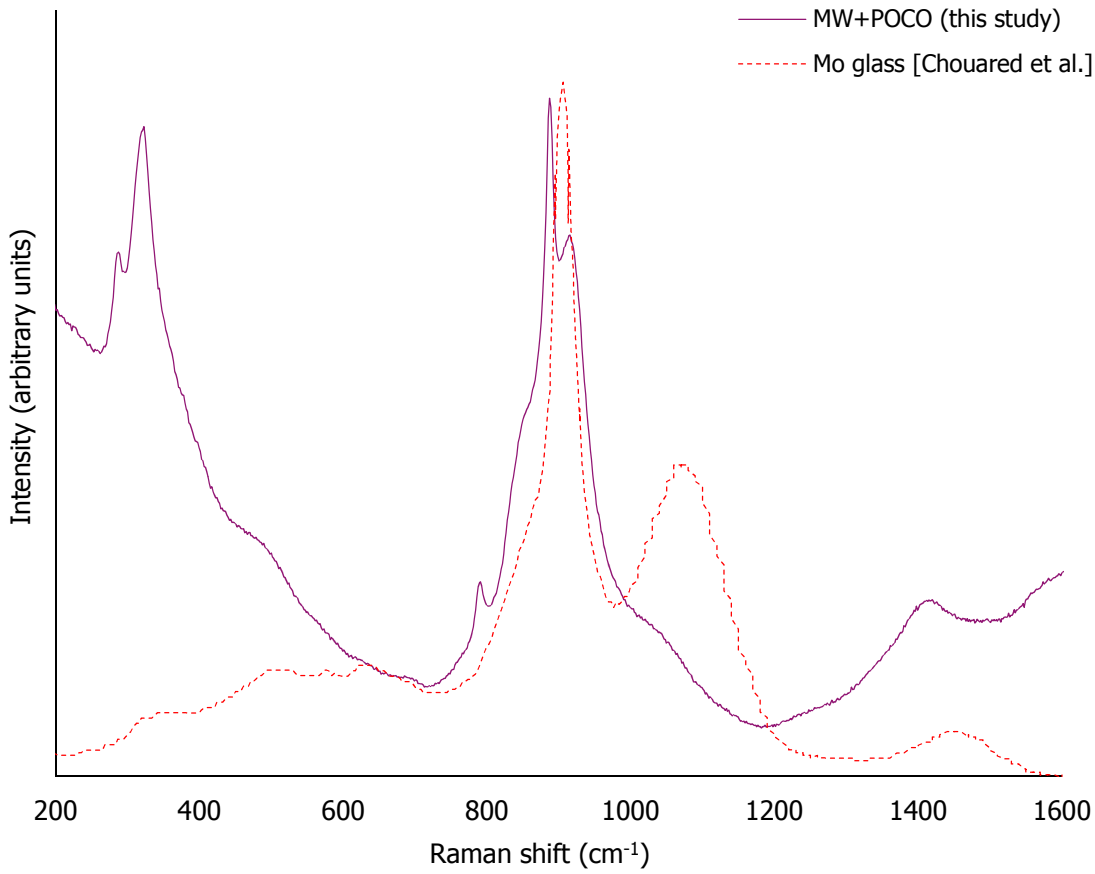

Figure 4.29: Raman spectra of MW + POCO and spectra of soda-lime aluminosilicate glass containing Mo [7].

Similarly for Low and High Magnox, the band with a peak occurring at 912 cm^{-1} in the MW + POCO spectrum is thought to be due the presence of MoO_4 tetrahedra in a glass environment. It is therefore suggested that MW + POCO contains MoO_4 units in crystalline phases and in the glass network.

The spectra from Low and High Magnox indicate the presence of MoO_4 tetrahedra in amorphous form but show no evidence of crystalline Mo-containing phases whereas the spectrum of MW+POCO suggests the presence of Mo in crystalline and amorphous forms. From **Table 4.1**, the Mo content of MW + POCO is (by weight) more than twice that of High Magnox and more than five times that of Low Magnox. This suggests that increasing Mo content results in the likelihood of crystal phase formation in the glass.

4.6.4 Ca/Zn + POCO Raman Spectroscopy Results

The Raman spectroscopy results from Ca/Zn + POCO were unique in that each site scanned produced a different spectrum. The spectra obtained from Ca/Zn + POCO are shown in **Figure 4.30** below.

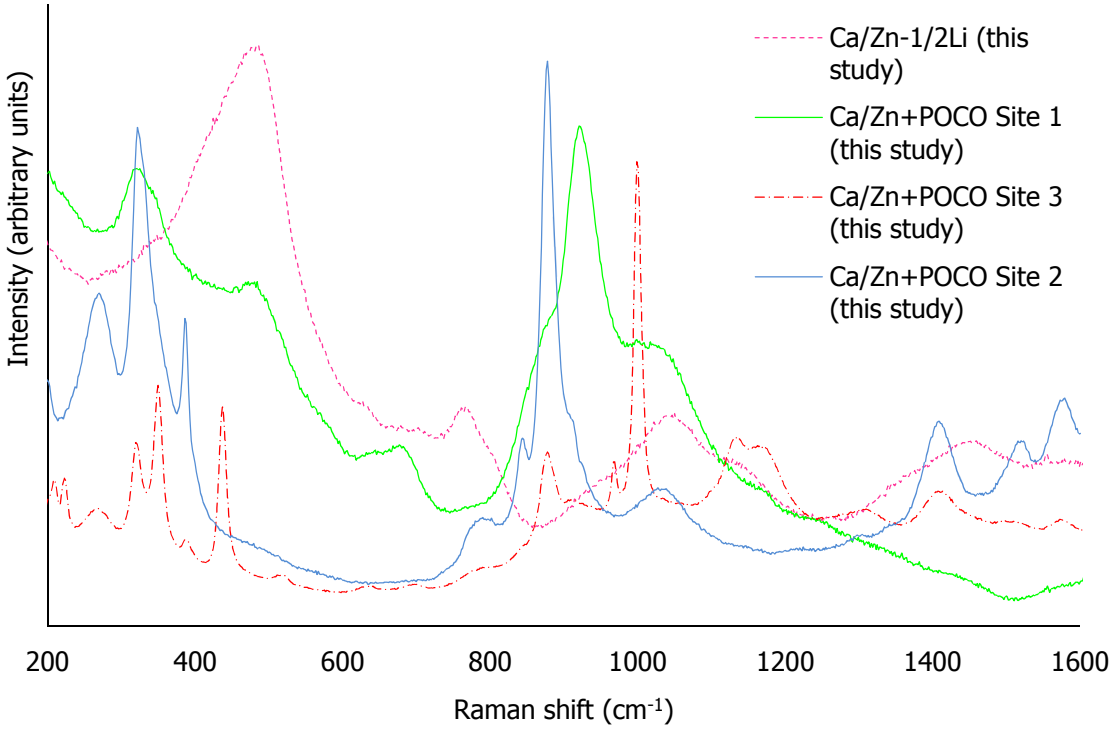

Figure 4.30: Raman spectra of Ca/Zn + POCO and Ca/Zn-½Li.

From the EDX data presented in **Section 4.4** it was expected that Ca/Zn + POCO would contain crystalline $CaMoO_4$ phases, therefore the spectra from Ca/Zn + POCO sites 2 and 3 were compared with the spectra from crystalline $CaMoO_4$ obtained from the RRUFF database [11] in **Figure 4.31** below.

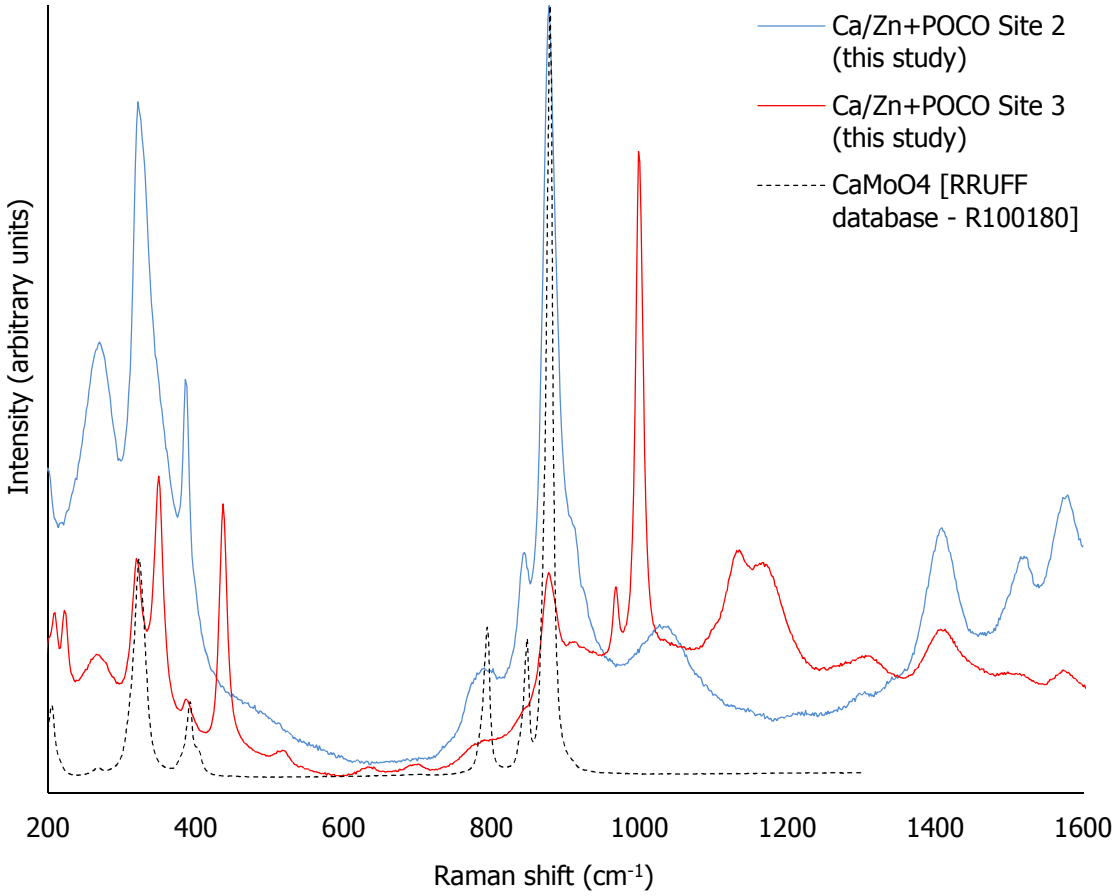

Figure 4.31: Raman spectrum of Ca/Zn + POCO sites 2 and 3 compared with the spectrum from crystalline $CaMoO_4$ [11].

From **Figure 4.31** it can be seen that the spectra from Ca/Zn + POCO sites 2 and 3 have bands at similar positions to those found in the spectrum from crystalline $CaMoO_4$. This observation is considered to confirm the presence of $CaMoO_4$ phases deduced from the EDX results presented in **Section 4.4**. From **Figure 4.31** it can also be seen that the spectrum from Ca/Zn + POCO site 3 contains bands of relatively high intensity with peaks at 437, 967 and 999 cm^{-1} and bands of low intensity with peaks at 517, 634 and 697 cm^{-1} which cannot be seen in the spectra from Ca/Zn + POCO sites 1 and 2 or crystalline $CaMoO_4$.

The EDX results in **Section 4.4** indicate the presence of RuO_2 phases in the sample. It was therefore considered appropriate to compare the spectra from Ca/Zn + POCO site 3 with Raman spectra from RuO_2 in the literature. To this

end, Raman spectra from RuO_2 crystals and "nanorods" were obtained from a study by Chen et al. [12] and compared with the spectra from Ca/Zn + POCO site 3 as shown in **Figure 4.32** below.

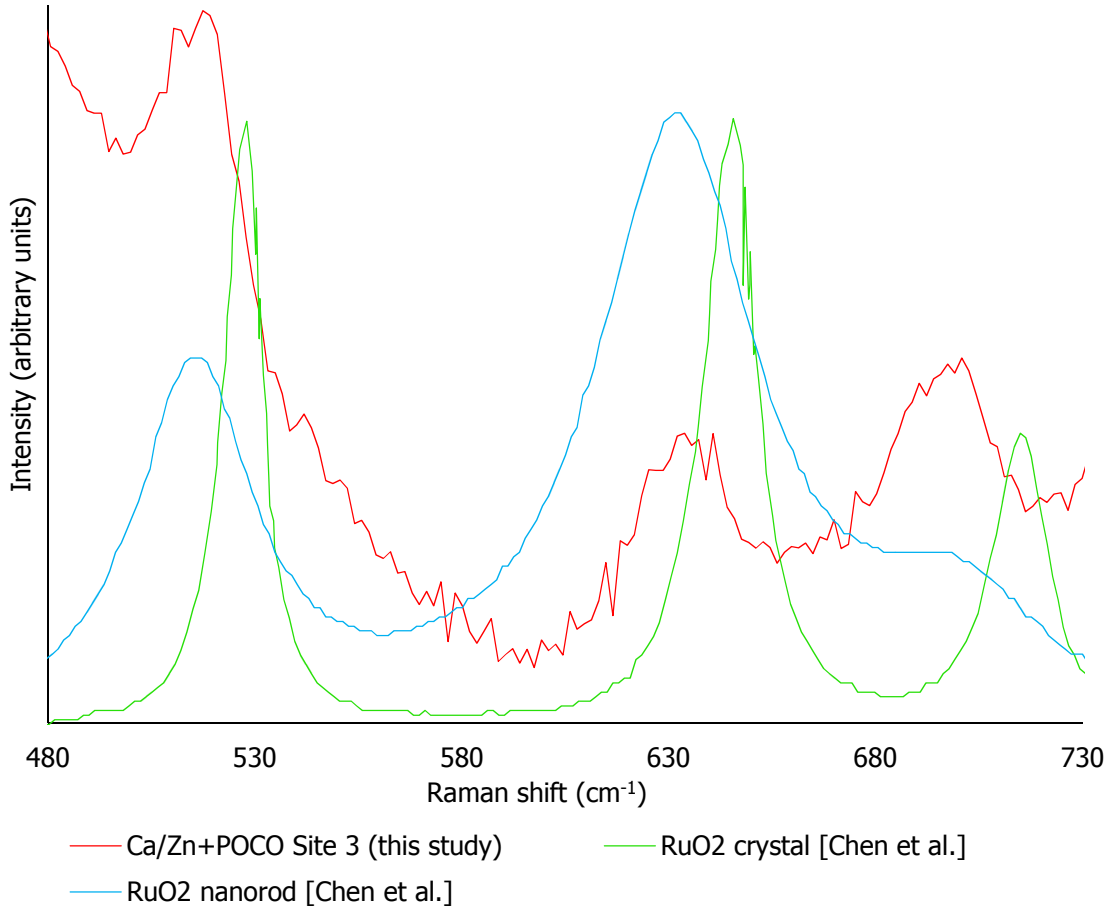

Figure 4.32: Raman spectrum of Ca/Zn + POCO site 3 compared with the spectra from RuO_2 crystals and nanorods [12].

According to Chen et al. [12] the bands in the spectrum for crystalline RuO_2 have peaks at 528, 646 and 716 cm^{-1}. The digitised spectrum of RuO_2 nanorods by Chen et al. [12] show that the bands have peaks at 516, 632 and 690 cm^{-1} which are considered to be consistent with the peaks observed at 517, 634 and 697 cm^{-1} in the Ca/Zn + POCO site 3 spectrum.

As for Low and High Magnox and MW + POCO, the spectrum from Ca/Zn + POCO site 1 contains a relatively broad band with a peak at 921 cm^{-1}. This band was expected to be due to the presence of MoO_4 tetrahedra in the glass network. To

confirm this, the spectra from Ca/Zn + POCO site 1 was compared with the spectra of Mo glass acquired from Chouard et al. [7] as shown in **Figure 4.33**.

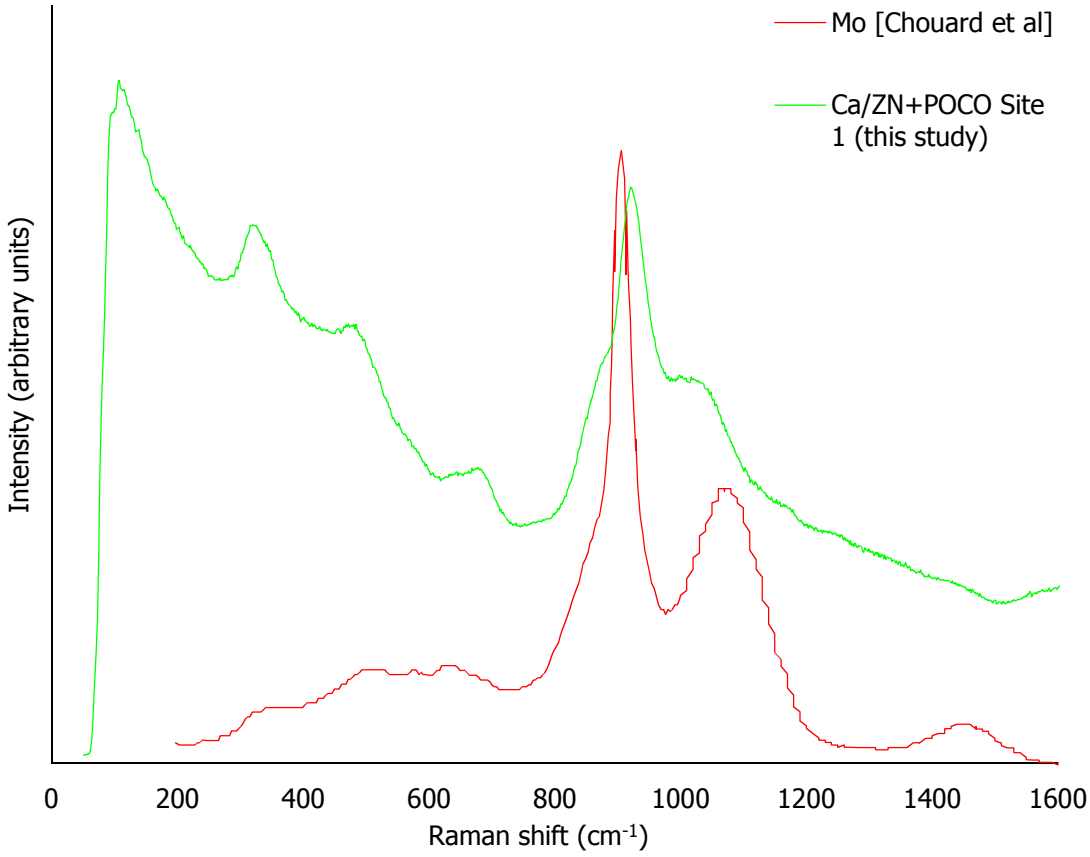

Figure 4.33: Raman spectra of Ca/Zn + POCO site 1 and soda-lime aluminosilicate glass containing Mo [7].

The spectra shown in **Figure 4.33** suggests that Ca/Zn + POCO contains MoO_4 units in the glass network.

The Raman spectroscopy data presented in this chapter suggest that MW + POCO and Ca/Zn + POCO contain MoO_4 units in both amorphous and crystalline forms. For MW + POCO, the evidence presented suggests that MoO_4 tetrahedra exist in crystalline phases such as $Na(Nd,Gd)(MoO_4)_2$ whereas in Ca/Zn + POCO, MoO_4 is found in $CaMoO_4$. It is worth noting that the spectra from monoclinic (M) ZrO_2 [13] was compared with the spectra from the vitrified wasteforms, however no agreement was found (see **Figure 4.34** and **Figure 4.35**).

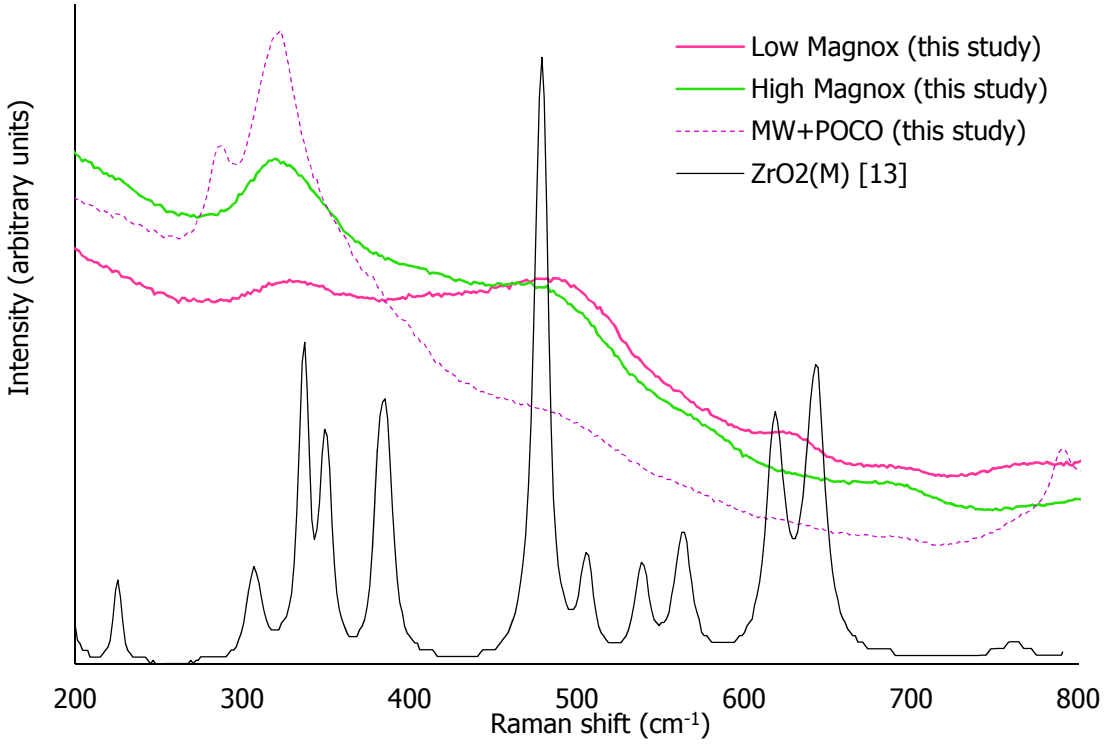

Figure 4.34: Raman spectra of Low Magnox, High Magnox, MW + POCO and monoclinic ZrO_2 [13].

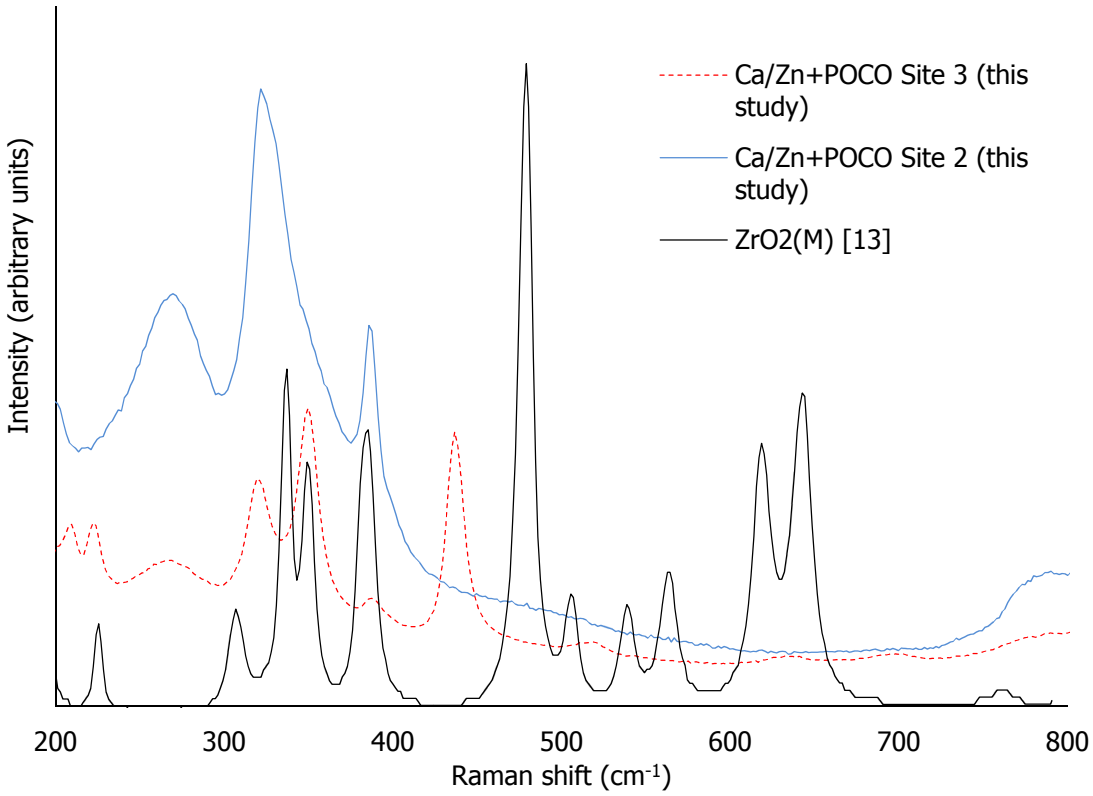

Figure 4.35: Raman spectra of Ca/Zn + POCO and monoclinic ZrO_2 [13].

4.7 Chapter 4 Discussion

The XRF results show inconsistencies between the nominal compositions (see **Table 4.1**) and SEM EDX data. In SEM EDX, spectra are taken from specific target areas on the samples whereas in XRF, an average spectra over each sample in powder form was obtained.

SEM images of the vitrified wasteforms show evidence of phase separation. SEM EDX spectra showed evidence of separate spinel [$(Mg,Ni)(Fe,Al,Cr)_2O_4$], Ru, Ce/Zr, Ce/Gd and $Na(Nd,Gd)(MoO_4)_2$ phases in wasteforms based on MW glass and evidence of Ru and $CaMoO_4$ phase separation in the wasteform based on Ca/Zn glass. These results are consistent with those reported by Short [4].

Raman spectroscopy from each simulated vitrified wasteform sample showed evidence of MoO_4 in a glass environment. Evidence of $Na(Nd,Gd)(MoO_4)_2$ and $CaMoO_4$ crystals were found in the Raman spectra of MW + POCO and Ca/Zn + POCO respectively. The Raman spectra of Ca/Zn + POCO also revealed the presence of RuO_2 crystals.

4.8 Chapter 4 References

[1] M. T. Harrison, "Vitrification of High Level Waste in the UK," *Procedia Materials Science,* vol. 7, pp. 10-15, 2014.

[2] M. T. Harrison, Private communication, 2014.

[3] R. J. Short, *Private communication,* 2013.

[4] R. Short, "Phase separation and crystallisation in UK HLW vitrified products," *Procedia Materials Science,* vol. 7, pp. 93-100, 2014.

[5] B. G. Parkinson, D. Holland, M. E. Smith, A. P. Howes and C. R. Scales, "The effect of C2O2 additions on HLW wasteform glasses," *J. Non-Cryst. Solids.,* vol. 32, pp. 483-497, 2007.

[6] A. A. Osipov, L. M. Osipova and V. E. Eremyashev, "Structure of alkali borosilicate glasses and melts according to raman spectroscopy data," *Glass Phys. Chem.,* vol. 39, pp. 105-112, 2013.

[7] N. Chouard, D. Caurant, O. Majerus, J. L. Dussossoy, K. S, D. Pytalev, R. Baddour-Hadjean and J. P. Pereira-Ramos, "Effect of MoO3, Nd2O3 and RuO2 on the crystallisation of soda-lime borosilicate glasses," *J. Mater. Sci.,* vol. 50, pp. 219-241, 2015.

[8] S. Schuller, O. Pinet, A. Grandjean and T. Blisson, "Phase separation and crystallization of borosilicate glass enriched in MoO3, P2O5, ZrO2, CaO," *J. Non-Cryst. Solids,* vol. 354, pp. 296-300, 2008.

[9] C. Luz-Lima, G. D. Saraiva, A. G. Souza Filho, W. Paraguassu, P. T. C. Freire and J. Mendes Filho, "Raman spectroscopy study of Na2MoO4·2H2O and Na2MoO4 under hydrostatic pressure," *J. Raman Spectrosc.,* vol. 41, p. 576–581, 2010.

[10] R. J. Short, R. J. Hand, N. N. Hyatt and G. Mobus, "Environment and oxidation state of molybdenum in simulated high level waste glass compositions," *J. Nucl. Mater.,* vol. 340, pp. 179-186, (2005).

[11] R. T. Downs, "The RRUFF Project: an integrated study of the chemistry, crystallography, Raman and infrared spectroscopy of minerals.," in *Program and Abstracts of the 19th General Meeting of the International Mineralogical Association*, Kobe, Japan, 2006.

[12] R. S. Chen, C. C. Chen, Y. S. Huang, C. T. Chia, H. P. Chen, D. S. Tsai and K. K. Tiong, "A comparative study of microstructure of RuO2 nanorods via Raman scattering and field emission scanning electron microscopy," *Solid State Commun.,* vol. 131, pp. 349-353, 2004.

[13] A. Gazzoli, G. Mattei and M. Valigi, "Raman and X-ray investigations of the incorporation of Ca2+ and Cd2+ in the ZrO2 structure," *J. Raman Spectrosc.,* vol. 38, no. 7, pp. 824-831, 2007.

5. MD Models of Simplified Vitrified High Level Wasteforms

5.1. Materials Modelled

In addition to the experimental studies of vitrified HLW forms presented in **Chapter 4**, MD simulations of "simplified" Low Magnox, High Magnox and MW + POCO were created and the results are presented in this Chapter. Although it was initially intended to model Ca/Zn glass and Ca/Zn + POCO wasteforms, this was not possible within the time constraints of the project due to the lack of a potential function for Zn-O that was compatible with the partial charges used for other cation-oxygen interactions.

Each simulation reported in this Chapter was created using the DL_POLY Classic code [1]. Initially, each material was modelled using only two-body potentials to describe the cation-oxygen interactions, however this resulted in molybdenum having a coordination number of six. These models are labelled '#1' below. The Raman spectroscopy results presented in **Section 4.6** and the findings of Short et al. [2] suggest the presence of MoO_4 tetrahedra in the simulated vitrified wasteforms, therefore, a coordination number of four was expected. To resolve this, a second model of each material was made with an additional three-body potential to control the O-Mo-O bond angles. These models are labelled '#2' below. In order to make models of glasses that could be run with the computing resources and time available, only the nine oxides with the highest mole fraction were included. This was necessary since including oxides at low concentrations would require large numbers of base glass atoms to be included which, in turn, would have resulted in impractical computation times. Therefore, the wasteform compositions modelled in this work are referred to as "simplified" Low Magnox, High Magnox and MW + POCO.

5.2. Simulation Details

5.2.1. Atomic Compositions

The atomic composition of the vitrified wasteform models were calculated by taking the compositional data provided in **Table 4.1** and calculating the composition in terms of mole fraction x_i for each oxide using the equation:

$$x_i = \frac{\frac{w_i}{M_i}}{\sum_{i=1}^{N} \frac{w_i}{M_i}} \quad \textbf{(5.1)}$$

where N is the total number of oxides and w_i and M_i are the mass fraction and molar mass of oxide i respectively. The constituent oxides were then ranked in terms of mole fraction (the oxide with the highest mole fraction having the highest rank). The numbers of each type of atom were determined by calculating the number of moles n_i of each oxide i that would be present in one gram of each simplified wasteform as per **Equation (5.2)**:

$$n_i = \frac{w_i}{M_i} \quad \textbf{(5.2)}$$

If oxide i is composed of A_i cations and B_i oxygen anions, the number of atoms a_i in n_i moles of substance is:

$$a_i = n_i N_A (A_i + B_i) \quad \textbf{(5.3)}$$

where N_A is Avogadro's constant.

Equation (5.3) allows the number of cations and oxygen anions in n_i moles of substance to be determined. The fraction of atoms in oxide i as a fraction of all the atoms in the simulation b_i is given by:

$$b_i = \frac{a_i}{\sum_{i=1}^{N} a_i} = \frac{n_i (A_i + B_i)}{\sum_{i=1}^{N} n_i (A_i + B_i)} \quad \textbf{(5.4)}$$

In order to run the MD simulations on standard desktop computers, it was necessary to make the total number of atoms small (~ 2000). If the total number of atoms in the simulation is N_T, the product of N_T and atomic fraction $b_{i.}$ for a particular oxide gives the total number of atoms due to that oxide, that is:

$$k_i(A_i + B_i) = b_i \cdot N_T \qquad \textbf{(5.5)}$$

where k_i is the number of oxide i "units" present in the simulation.

Since the number of each atom type must be an integer, there are rounding errors associated with the process described above. Generally, using a higher value of N_T reduces the rounding error; however, this also results in a larger number of atoms to be simulated and thus a greater computing time. For the simulations reported in this work, a target value of N_T = 2000 atoms was used. The atomic composition of each model is shown in **Table 5.1** below.

Table 5.1: Atomic compositions of simplified Low Magnox, High Magnox and MW + POCO MD models.

Atom	Low Magnox	High Magnox	MW + POCO
O	1178	1168	1169
Si	339	282	294
B	206	174	176
Na	130	104	118
Li	80	96	108
Mg	29	77	44
Al	20	60	34
Fe	10	26	20
Zr	3	8	14
Mo	2	7	17
Total	1997	2002	1994

For each model, an initial (random) configuration of atoms was generated by creating a 'box' containing all the atoms in the simulation at a user specified density. Initially the densities used for the simulations were the experimentally determined densities reported in **Section 4.3**, however, this led to instabilities in the High Magnox and MW + POCO models. In order to resolve this issue, the volume of the High Magnox and MW + POCO simulation boxes were increased by 10 % to allow for the fact that many heavier elements in the glass were not included in the model (therefore the simplified model densities are expected to be lower than the experimental wasteform densities). The densities used in the simulations are shown in **Table 5.2** below.

Table 5.2: Densities used for the MD simulations of Low Magnox, High Magnox and MW + POCO.

Composition	Nominal measured density ($g \cdot cm^{-3}$)	Simulation density ($g \cdot cm^{-3}$)	Percent difference (simulation/measured)
Low Magnox	2.600	2.600	0.00 %
High Magnox	3.252	2.956	-9.09 %
MW + POCO	2.964	2.695	-9.09 %

5.2.2. Two-Body Potential Parameters

The Buckingham potential function **Equation (2.15)** was used to describe the two-body interaction between each cation and oxygen. In a similar vein to work carried out by Mountjoy et al. [3], Buckingham potential functions for cation-cation interactions were not used because cations do not come into close contact in oxide materials, and at longer distances the cation-cation interaction is quite weak. Note however that the electrostatic repulsion between cations due to the Coulomb potential is included. The potential parameters used to simulate each cation-oxygen interaction were provided by Teter [4] except for B-O and Mo-O which were derived manually using the procedure described in **Section 3.2.1**. The potential parameters are listed in **Table 5.3** below.

Table 5.3: Buckingham potential parameters.

Atom 1	Charge (e)	Atom 2	Charge (e)	A (eV)	ρ (Å)	C (eV·Å6)	r_{min} (Å)
O	-1.2	O	-1.2	1844.8	0.34365	192.58	1.60
Si	2.4	O	-1.2	13702.9	0.19382	54.68	1.00
B	1.8	O	-1.2	4300.0	0.18500	11.80	0.90
Na	0.6	O	-1.2	4383.8	0.24384	30.70	1.20
Li	0.6	O	-1.2	41051.9	0.15611	0.00	1.15
Mg	1.2	O	-1.2	7063.5	0.21090	19.21	0.78
Al	1.8	O	-1.2	12201.4	0.19563	32.00	0.90
Fe	1.8	O	-1.2	19952.3	0.18254	4.66	0.56
Zr	2.4	O	-1.2	17943.4	0.22663	127.65	1.00
Mo	3.6	O	-1.2	5700.0	0.22900	30.00	0.86

5.2.3. Three-Body Potential Parameters

In the second of the two models of each wasteform (labelled #2), a three-body potential was applied to O-Mo-O configurations to encourage the formation of 109.47° angles (i.e. encouraging the formation of MoO_4 tetrahedra). The three body potential applied was the screened harmonic type described by **Equation (2.17)**. The potential parameters applied are shown in **Table 5.4** below, where r_{max} is a cut-off distance.

Table 5.4: Three body potential parameters for O-Mo-O

K (eV)	θ_0 (°)	ρ_1 (Å)	ρ_2 (Å)	r_{max} (Å)
100.00	109.47	1.00	1.00	3.00

5.2.4. Heat Treatment Scheme

The simulations of Low Magnox, High Magnox and MW + POCO were subject to the heat treatment scheme shown in **Table 5.5** below. Each stage of the scheme was simulated in the NVT (constant volume and temperature) ensemble with an external pressure of 0 kbar. Note that in stage 4, a quench rate of 2×10^{13} K·s^{-1} was used (therefore this stage was not strictly carried out in the NVT ensemble).

Table 5.5: Heat treatment scheme for simplified Low Magnox, High Magnox and MW + POCO.

Stage	Temperature (K)	Time-step length (ps)	Total number of steps	Number of steps with equilibration	Total duration (ps)
1	6 000	10^{-3}	200 000	150 000	200
2	4 000	10^{-3}	200 000	150 000	400
3	2 000	10^{-3}	200 000	150 000	600
4	2 000 - 300	10^{-3}	86 000	85 000	686
5	300	10^{-3}	300 000	150 000	986

5.2.5. GULP Results

The potential parameters listed in **Table 5.3** above were input into the GULP program for crystal structures obtained from the Inorganic Crystal Structure Database (ICSD) [5]. The crystal structures tested are listed in **Table 3.3** (**Section 3.2.3**) and **Table 5.6** below. Changes made to the mean cation-oxygen bond lengths ($<d_{X\text{-}O}>$) and unit cell volumes are also reported in **Tables 3.3** and **5.6**. A comprehensive set GULP results are presented in **Appendix A**. For every structure tested, the cation-oxygen coordination numbers were found to be same in the input and output structures.

Table 5.6: Crystal structures obtained from [5] **tested using GULP.**

Chemical name	Chemical formula	ICSD [5] reference	Unit cell volume change (%)	Mean cation-oxygen bond length change (%)	
Magnesium oxide	MgO	88058	-2.93	-0.95	Mg-O
Aluminium oxide	Al_2O_3	51687	1.67	1.05	Al-O
Iron (III) oxide	Fe_2O_3	82902	-1.66	-0.99	Fe-O
Zirconium oxide	Zr_2O	80046	-1.73	0.47	Zr-O
Molybdenum trioxide (orthorhombic)	MoO_3	35076	-13.52	7.58	Mo-O
Molybdenum trioxide (monoclinic)	MoO_3	80577	-12.65	< 0.01	Mo-O
Disodium molybdate(VI)	Na_2MoO_4	151971	-3.38	7.24	Mo-O
				-2.96	Na-O
Calcium molybdate (powellite)	$CaMoO_4$	22351	2.51	13.82	Mo-O
				-3.70	Na-O

From the tables in **Appendix A**, the addition of a three-body potential to control the O-Mo-O bond angle increases the size of the unit cells of calcium molybdate and disodium molybdate. However, viewing the calcium and disodium molybdate crystals in Materials Studio software showed that the O-Mo-O bonds making up the MoO_4 tetrahedral units in these crystals do not form 109.47° angles. It is therefore not surprising that the application of a three-body potential to make the O-Mo-O triplets form 109.47° angles distorts the unit cells. The three-body potential was not applied to MoO_3 as this does not contain MoO_4 tetrahedral units. It is recognised that the Mo-O two-body potential parameters might be further improved through manual adjustment using GULP, however this was not possible due to time constraints on the project.

5.3. Simplified Vitrified Wasteform Simulation Results

5.3.1. Simplified Low Magnox Simulation Results

Results of simplified Low Magnox MD simulations are presented below. Two models were created. In the Low Mag #1 model, only the two-body Buckingham potential and the parameters presented in **Table 5.3** were used. In Low Mag #2, the same two-body potentials plus a three-body potential to control the O-Mo-O bond angle were used (see **Section 5.2.3**). Both simulations were made up of the number of atoms listed in **Table 5.1** above. Visual representations of the Low Mag #1 and Low Mag #2 models are presented in **Figures 5.1** and **5.2** respectively.

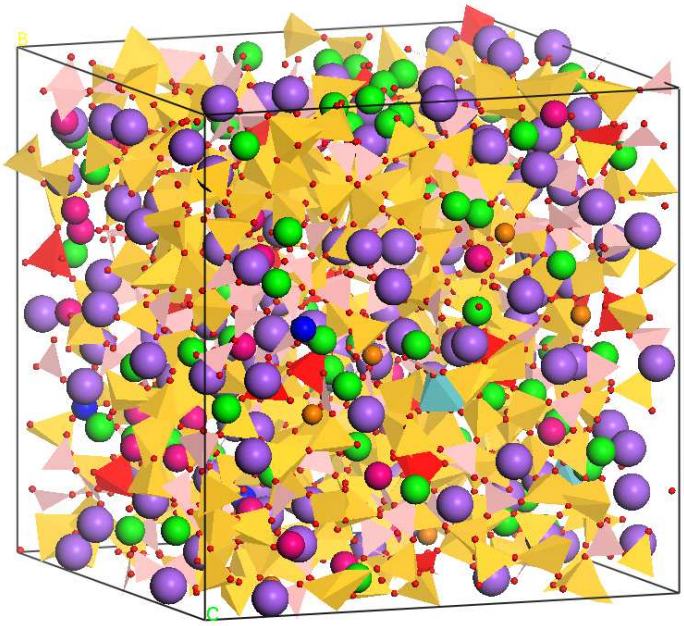

Figure 5.1: Visual representation of the Low Mag #1 MD model.

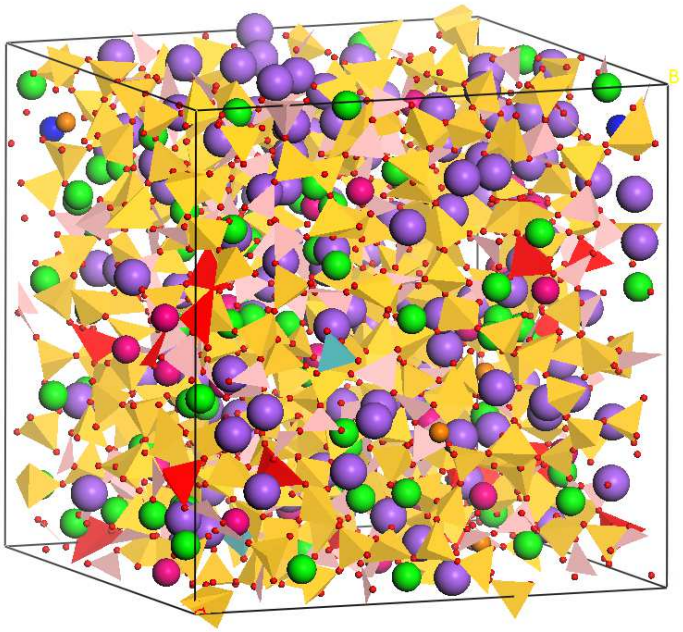

Figure 5.2: Visual representation of the Low Mag #2 MD model.

Table 5.7: Key for Figure 5.1 and Figure 5.2.

gold tetrahedra:	silicon	light blue polyhedra:	molybdenum
small red spheres:	oxygen	pink triangles/tetrahedra:	boron
red polyhedra:	aluminium	purple spheres:	sodium
orange spheres:	iron	pink spheres:	magnesium
dark blue spheres:	zirconium	green spheres:	lithium

Figure 5.1 shows two MoO_6 octahedra amongst the glass network in the Low Mag #1 model. **Figure 5.2** shows two MoO_4 tetrahedra amongst the glass network in the Low Mag #2 model. The observations from **Figure 5.2** are consistent with what was observed in Raman spectroscopy (see **Section 4.6.2**).

Radial Distribution Functions (Low Magnox)

The RDF $g(r)$ for each cation to oxygen obtained from the Low Magnox simulations are shown in **Figure 5.3** below. The RDFs are designated "X-O" where X is a cation species (e.g. the curve labelled "Fe-O" in **Figure 5.3** is the iron-oxygen RDF). The average element-oxygen nearest neighbour distances $<d_{X\text{-}O}>$, are presented in **Table 5.8**.

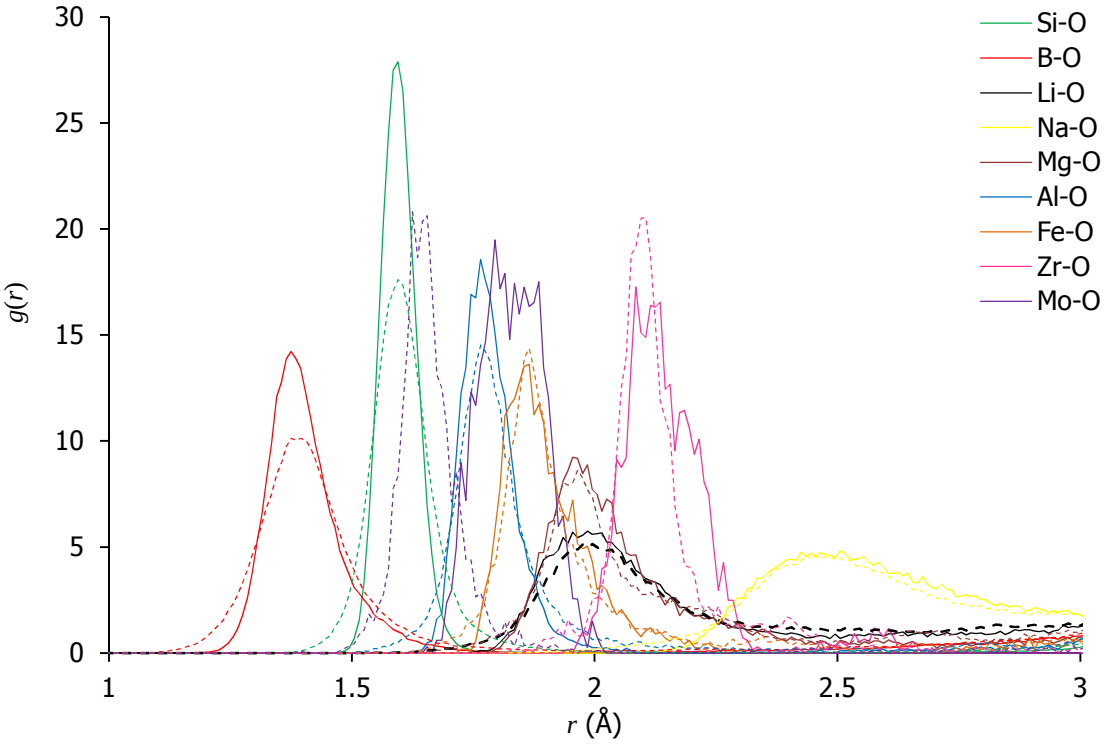

Figure 5.3: RDFs predicted by MD simulations for simplified Low Magnox. Solid lines are from Low Mag #1 and dashed lines are from Low Mag #2.

Table 5.8: Average element-oxygen nearest neighbour distances from simulations of simplified Low Magnox (σ is the standard deviation).

Model	Nearest neighbour distances $<d_{X\text{-}O}>$ (Å)								
	Si-O	B-O	Li-O	Na-O	Mg-O	Al-O	Fe-O	Zr-O	Mo-O
Low Mag #1	1.60	1.41	2.06	2.63	2.07	1.78	1.90	2.14	1.83
σ (Å)	0.04	0.08	0.15	0.24	0.18	0.06	0.09	0.07	0.06
Low Mag #2	1.61	1.41	2.13	2.64	2.04	1.81	1.92	2.15	1.66
σ (Å)	0.08	0.12	0.23	0.29	0.16	0.15	0.15	0.15	0.06

The average Si-O bond length was found to be 1.60 Å and 1.61 Å in the both simulations of simplified Low Magnox. These values are consistent with the Si-O bond lengths predicted by the simulations of ABS and MW glass (using Buckingham potentials) reported in Chapter 3 (i.e. 1.59 Å).

The average B-O bond length was found to be 1.41 Å in both Low Magnox simulations. This is slightly higher than the values of 1.38 Å and 1.39 Å found in the simulations of ABS and MW glass using Buckingham potentials reported in **Chapter 3**.

The average Zr-O bond length was found to be 2.14 Å and 2.15 Å in Low Mag #1 and Low Mag #2 respectively. These values are somewhat shorter than the average value of 2.18 Å predicted by MD models of 'full Li' MW glass containing zirconium created by Connelly et al. [6]. It should be noted that only three zirconium atoms were included in the Low Magnox simulations and therefore the results have limited statistical validity.

From **Figure 5.3** and the data in **Table 5.8** it can clearly be seen that the application of a three-body potential to the O-Mo-O bond angle has a profound effect on the Mo-O RDF; it makes the average nearest oxygen neighbour distance shorter and produces a smother, albeit wider, distribution curve. An extended X-ray absorption fine structure (EXAFS) spectroscopy study of alkali borosilicate glasses containing Mo by Calas et al. [7] reports a mean Mo-O bond length of 1.78 Å (in MoO_4 units). The average Mo-O distances were found to be 1.83 Å and 1.66 Å in Low Mag #1 and Low Mag #2 respectively. However, it

should be noted that only two molybdenum atoms were included in the Low Magnox simulations and therefore the results have limited statistical validity. It is thought that the significant differences in Mo-O distance between the two MD models and experimental data are due to the Mo-O two-body potential parameters.

Coordination Numbers (Low Magnox)

The coordination numbers $CN(r)$ for silicon and boron from the models of simplified Low Magnox are shown in **Figure 5.4** below. The cumulative coordination numbers for molybdenum are shown in **Figure 5.5**

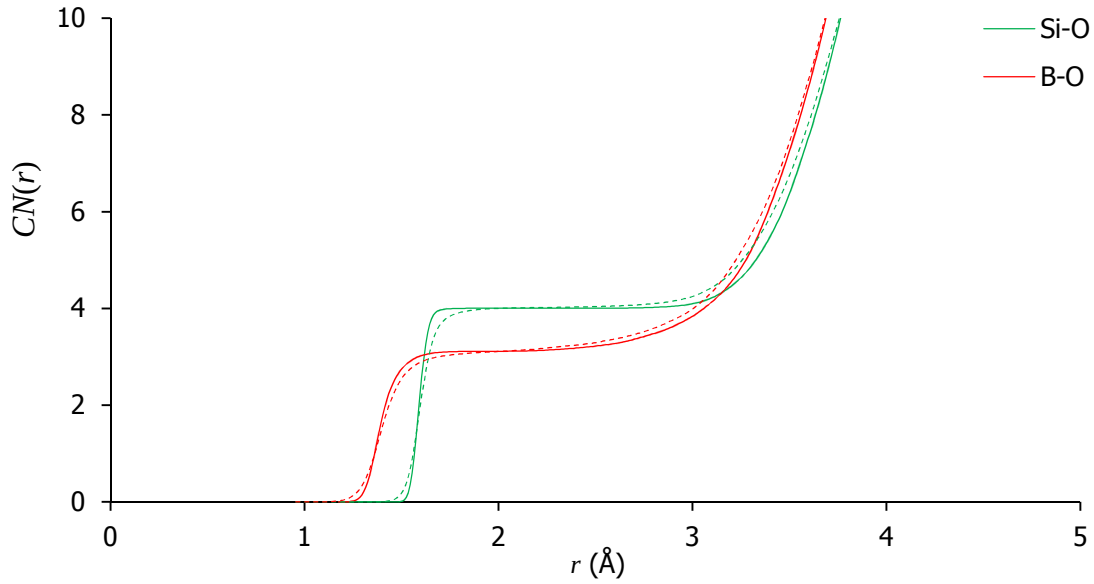

Figure 5.4: Coordination numbers for Si-O and B-O from simulations of simplified Low Magnox. Solid lines are from Low Mag #1 and dashed lines are from Low Mag #2.

In the Low Mag #1 simulation, 99 % of silicon atoms were found to be four-coordinated to oxygen and in the Low Mag #2 simulation, 98 % were found to be four-coordinated. The remaining silicon atoms were calculated to be five-coordinated (which is considered unrealistic). In the Low Mag #1 simulation, 89 % of the boron atoms were found to be three-coordinated and 11 % four-coordinated. In the Low Mag #2 simulation, the boron atoms were found to be: 87 % three-coordinated, 11 % four coordinated and 2 % two-coordinated

(with two-coordinated boron being considered unrealistic). It is concluded that the O-Mo-O three-body potential has negligible effect on silicon or boron coordination.

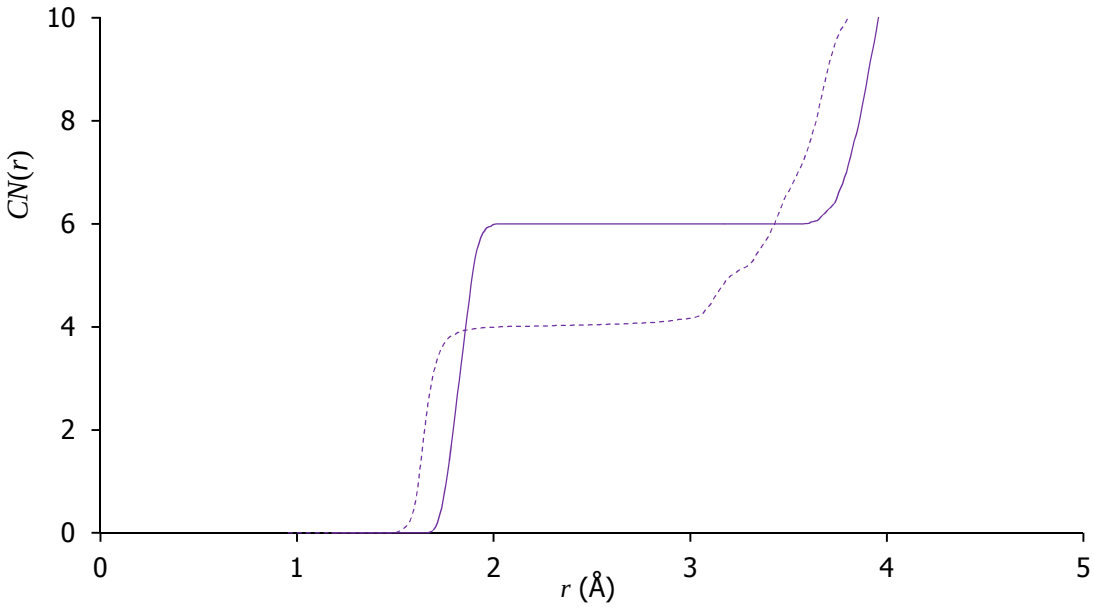

Figure 5.5: Coordination number for Mo-O from simulations of simplified Low Magnox. The solid line is from Low Mag #1 and the dashed line is from Low Mag #2.

Figure 5.5 clearly shows how the three-body potential influences the Mo-O coordination number. Without the three-body potential applied, the Mo-O coordination number sharply rises to six and remains at six in the range r = 2.00-3.58 Å. With the three-body potential applied, the molybdenum coordination reaches a value of four at r = 2.01 Å and continues to rise slowly to a value of 4.17 until, at around r = 3.00 Å, the coordination number gradient begins to rise rapidly. This steep rise is due to the three-body potential switching off at the user defined value of 3.00 Å.

Bond Angle Distributions (Low Magnox)

The bond angle distributions (BADs) for O-Si-O, O-B-O and O-Mo-O from the Low Magnox simulations are shown in **Figure 5.6** below. The average bond angles found in the simulations are reported in **Table 5.9**.

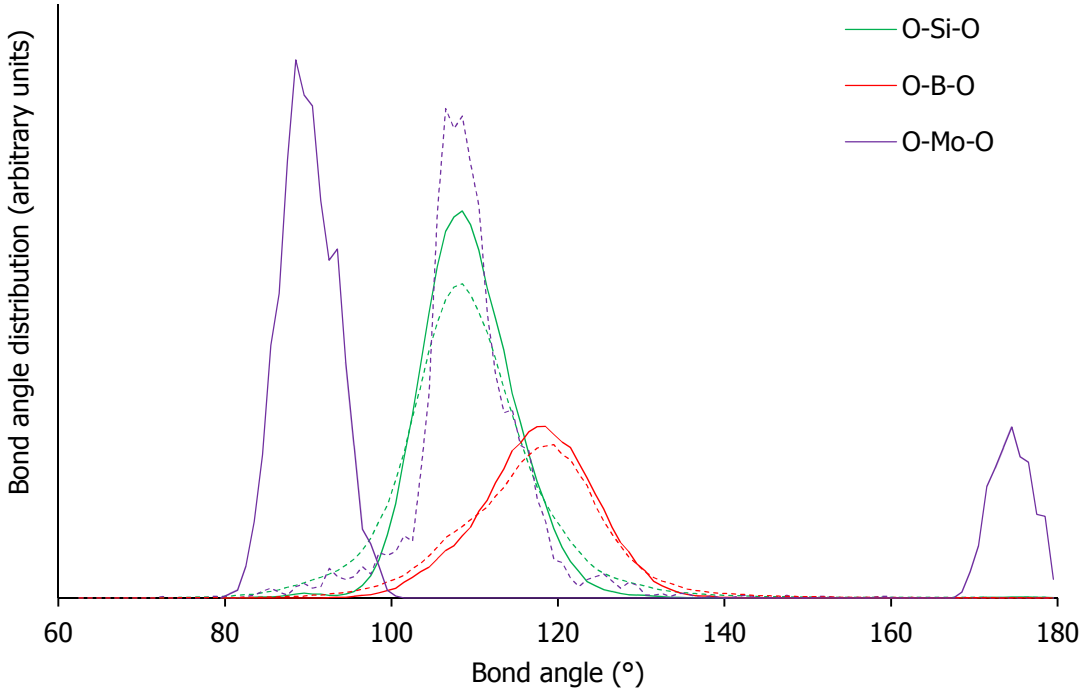

Figure 5.6: Bond angle distribution from simulations of simplified Low Magnox. Solid lines are from Low Mag #1 and dashed lines are from Low Mag #2.

Table 5.9: Average bond angles from simulations of simplified Low Magnox (σ is the standard deviation).

Model	<O-Si-O>	<O-B-O>	<O-Mo-O>
Low Mag #1	109°	117°	90°
σ	6°	8°	3°
Low Mag #2	109°	117°	109°
σ	9°	11°	7°

Both Low Magnox models produce average bond angles of 109° for O-Si-O indicating that silicon atoms are forming SiO_4 tetrahedra. The average bond angle for O-B-O was found to be 117° in both simulations, this value is close to the value of 120° that would be found in BO_3 triangular units. The BAD for O-Mo-O in Low Mag #1 contains two bands: one with a mean at 90° and the other with a mean at 174° (σ = 3°); suggesting the presence of octahedral MoO_6 units. In the Low Mag #2 model, the average O-Mo-O angle was found to be 109° indicating that molybdenum is forming MoO_4 tetrahedra due to the O-Mo-O three-body potential.

5.3.2. Simplified High Magnox Simulation Results

As with the Low Magnox simulations, two simulations of simplified High Magnox were created: one using only two-body potentials (designated Hi Mag #1) and the other, with the three-body potential applied to the O-Mo-O bond angle (designated Hi Mag #2). The three-body potential is described in **Section 5.2.3**. Both simulations were made up of the number of atoms listed in **Table 5.1** above. Visual representations of the Hi Mag #1 and Hi Mag #2 models are presented in **Figures 5.7** and **5.8** respectively.

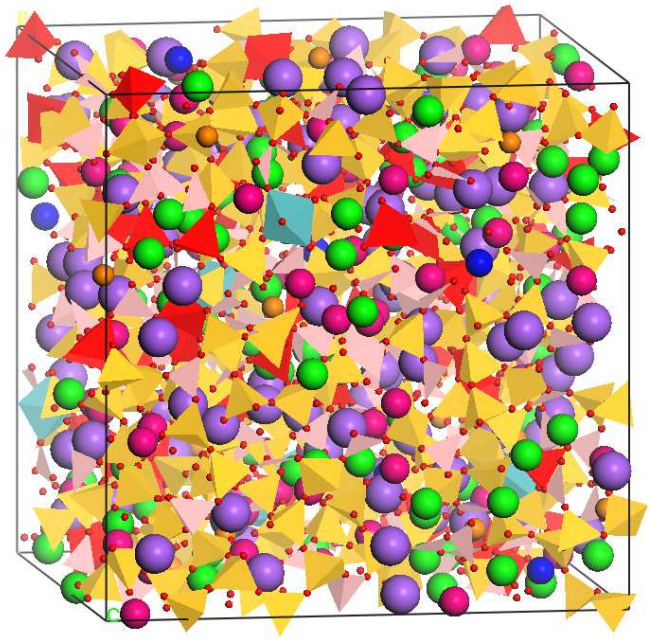

Figure 5.7: Visual representation of the Hi Mag #1 MD model.

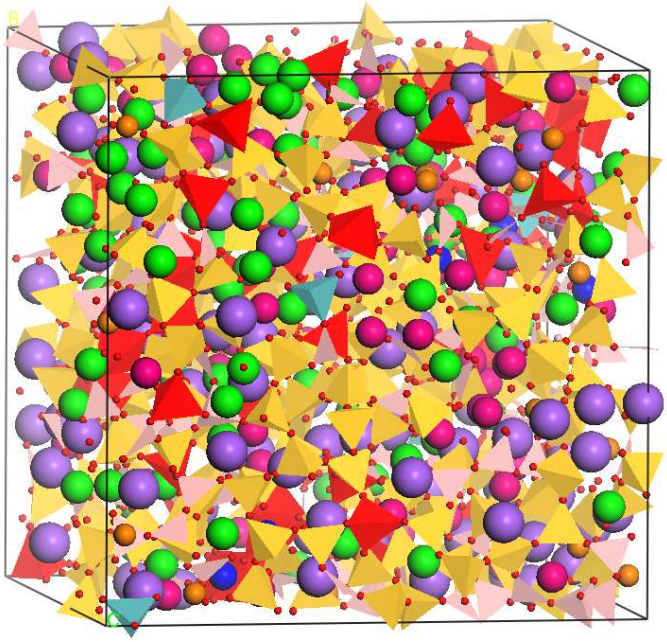

Figure 5.8: Visual representation of the Hi Mag #2 MD model.

Table 5.7 Key for Figure 5.7 and Figure 5.8.

gold tetrahedra:	silicon	light blue polyhedra:	molybdenum
small red spheres:	oxygen	pink triangles/tetrahedra:	boron
red polyhedra:	aluminium	purple spheres:	sodium
orange spheres:	iron	pink spheres:	magnesium
dark blue spheres:	zirconium	green spheres:	lithium

From initial inspection of **Figures 5.7** and **5.8** features similar to those observed in **Figures 5.1** and **5.2** can be observed, i.e. MoO_6 octahedra amongst the glass network in the Hi Mag #1 model and MoO_4 tetrahedra amongst the glass network in Hi Mag #2. Linkage of MoO_4 tetrahedra to silicon and boron in the glass network is discussed in **Section 5.4**.

Radial Distribution Functions (High Magnox)

The Radial Distribution Functions (RDFs) for each cation to oxygen obtained from the simplified High Magnox simulations are shown in **Figure 5.9** below. The average element-oxygen nearest neighbour distances $<d_{X\text{-}O}>$, are presented in **Table 5.10**.

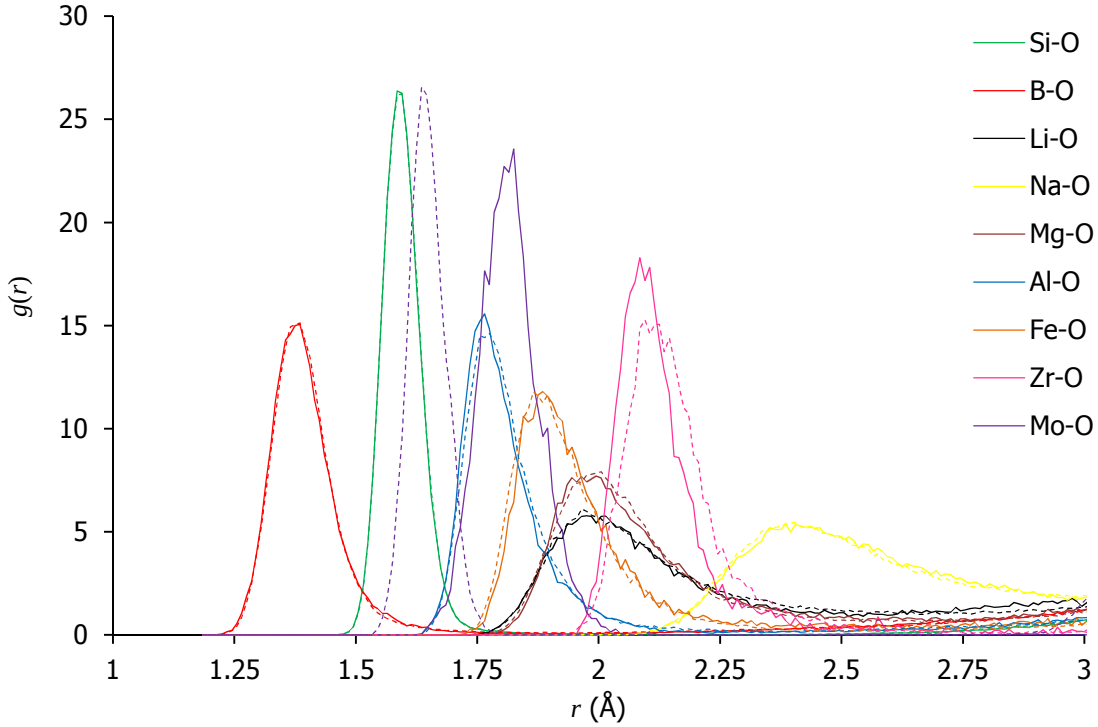

Figure 5.9: RDFs predicted by MD simulations for simplified High Magnox. Solid lines are from Hi Mag #1 and dashed lines are from Hi Mag #2.

Table 5.10: Average element-oxygen nearest neighbour distances from simulations of simplified High Magnox (σ is the standard deviation).

Model	Nearest neighbour distances $<d_{X\text{-}O}>$ (Å)								
	Si-O	B-O	Li-O	Na-O	Mg-O	Al-O	Fe-O	Zr-O	Mo-O
Hi Mag #1	1.60	1.40	2.08	2.59	2.11	1.81	1.96	2.14	1.82
σ (Å)	0.04	0.07	0.17	0.26	0.20	0.09	0.15	0.13	0.06
Hi Mag #2	1.60	1.40	2.12	2.63	2.09	1.82	1.94	2.16	1.65
σ (Å)	0.04	0.07	0.21	0.30	0.18	0.11	0.12	0.12	0.04

The average Si-O bond length was found to be 1.60 Å in both Hi Mag simulations. The average B-O bond length was found to be 1.40 Å in both Hi Mag simulations. The average Zr-O bond length was found to be 2.14 Å and 2.16 Å in Hi Mag #1 and Hi Mag #2 respectively. The average Mo-O distances in simplified High Magnox vary considerably from the experimentally determined value of 1.78 Å [7]. These results are consistent with the Low Magnox models and the comments made in **Section 5.3.1** above for the Low Magnox RDFs also apply to High Magnox. It is recognised that only seven molybdenum and eight zirconium atoms were included in the simplified High Magnox simulations which limits the statistical validity of the results.

Coordination Numbers (High Magnox)

The coordination numbers $CN(r)$ for silicon and boron from the models of simplified High Magnox are shown in **Figure 5.10** below. The cumulative coordination numbers for molybdenum are shown in **Figure 5.11**.

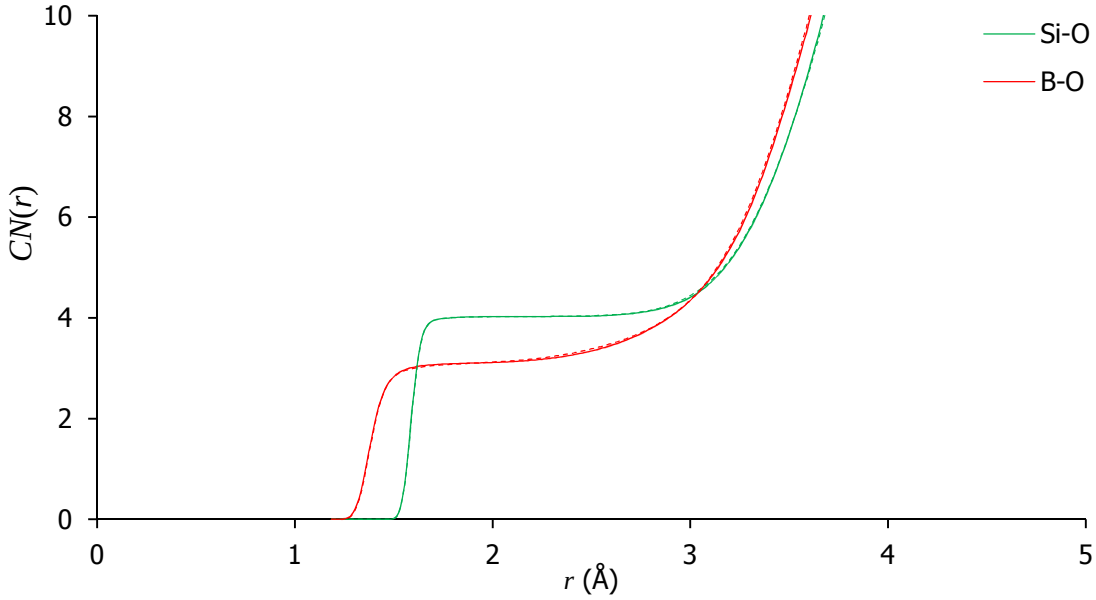

Figure 5.10: Coordination numbers for Si-O and B-O from simulations of simplified High Magnox. Solid lines are from Hi Mag #1 and dashed lines are from Hi Mag #2.

In the Hi Mag #1 simulation, 97 % of silicon atoms were found to be four-coordinated to oxygen and the Hi Mag #2 simulation, 98 % were found to be four-coordinated. The remaining atoms were calculated to be five-coordinated (which is considered unrealistic). In the Hi Mag #1 simulation, 89 % of the boron atoms were found to be three-coordinated and 11 % four-coordinated. In Hi Mag #2, 88 % of the boron atoms were found to be three-coordinated and the remaining 12 % were four-coordinated. As found in the Low Magnox simulations, the O-Mo-O three-body potential has negligible effect on silicon or boron coordination.

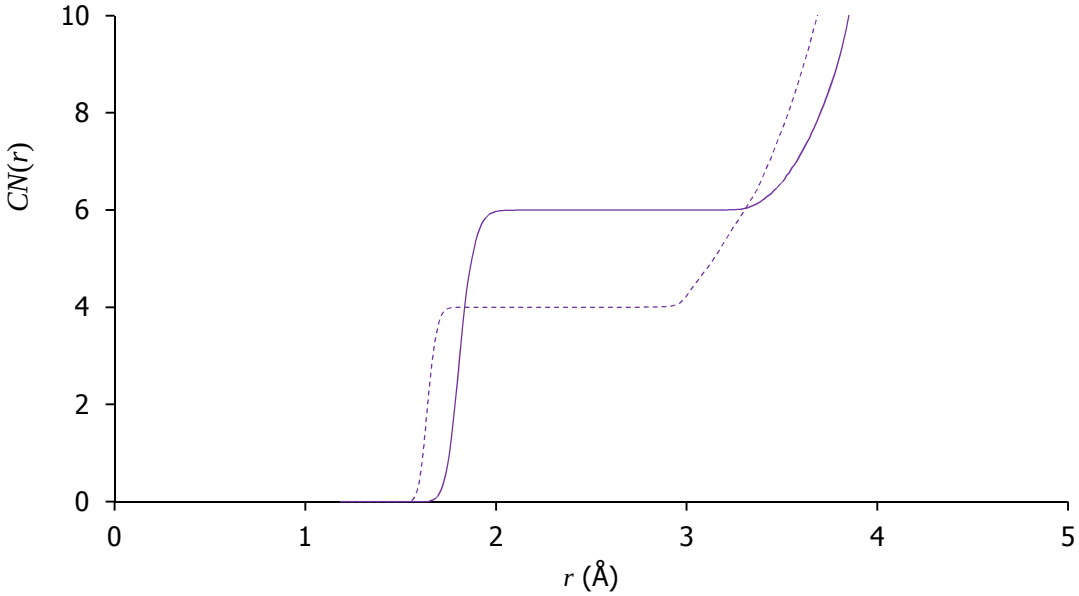

Figure 5.11: Coordination number for Mo-O from simulations of simplified High Magnox. The solid line is from Hi Mag #1 and the dashed line is from Hi Mag #2.

The Hi Mag #1 simulation shows molybdenum with a coordination number of six between r = 2.00–3.30 Å. In the Hi Mag #2 model, the molybdenum coordination number is forced to remain at four until reaching the three-body potential cut-off value of 3.00 Å.

Bond Angle Distributions (High Magnox)

The BADs for O-Si-O, O-B-O and O-Mo-O from the High Magnox simulations are shown in **Figure 5.12** below. The average bond angles found in the simulations are reported in **Table 5.11**.

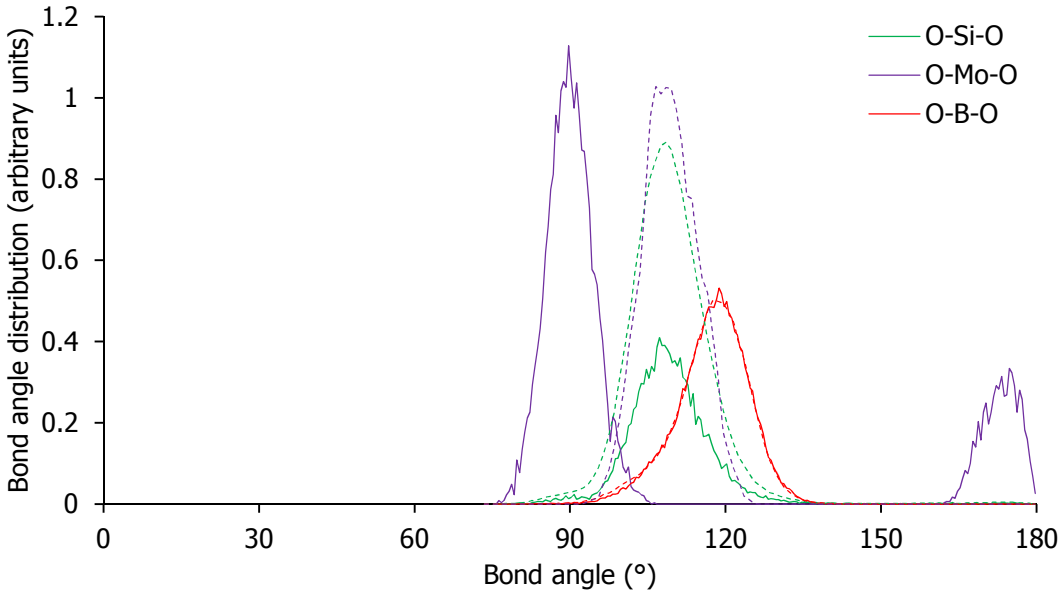

Figure 5.12: Bond angle distribution from simulations of simplified High Magnox. Solid lines are from Hi Mag #1 and dashed lines are from Hi Mag #2.

Table 5.11: Average bond angles from simulations of simplified High Magnox (σ is the standard deviation).

Model	<O-Si-O>	<O-B-O>	<O-Mo-O>
Hi Mag #1	109°	117°	90°
σ	9°	8°	5°
Hi Mag #2	109°	117°	109°
σ	9°	9°	6°

As with the Low Magnox simulations, both simulations of High Magnox produced average bond angles of 109° for O-Si-O and 117° for O-B-O. The BAD for O-Mo-O in Hi Mag #1 contains two bands: one with a mean at 90° and the other with a mean at 173° (σ = 4°); suggesting the presence of octahedral MoO_6 units. In the Hi Mag #2 model, the average O-Mo-O angle was found to be 109° indicating that molybdenum is forming MoO_4 tetrahedra.

5.3.3. Simplified MW + POCO Simulation Results

In a similar vein to the models of simplified Low and High Magnox, two models of simplified MW + POCO glass were created: one (designated MW+POCO # 1) using only two-body Buckingham potentials and the parameters listed in **Table 5.3** and the second (designated MW+POCO #2) with an additional three-body potential applied to the O-Mo-O bond angle (as described in **Section 5.2.3**). Both simulations were made up of the number of atoms listed in **Table 5.1** above. Visual representations of the MW + POCO #1 and MW + POCO #2 models are presented in **Figures 5.13** and **5.14** respectively.

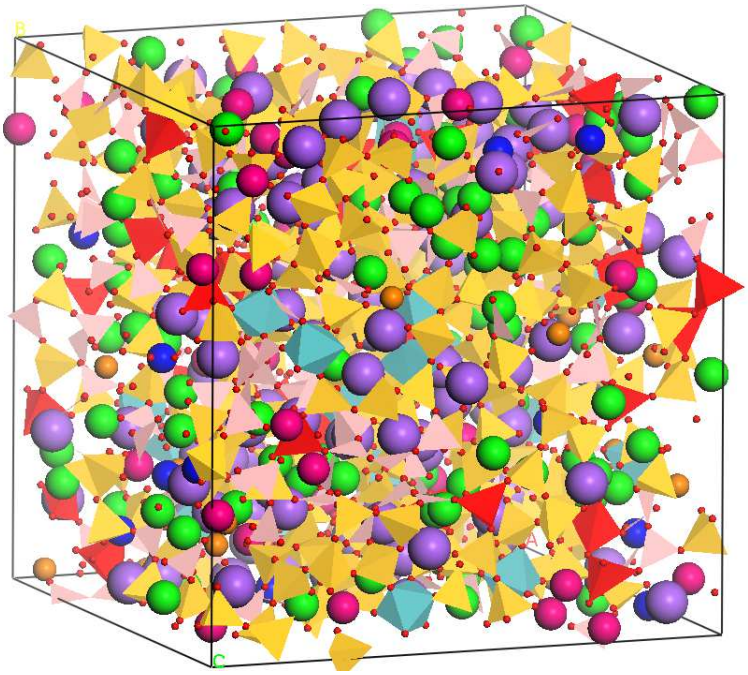

Figure 5.13: Visual representation of the MW + POCO #1 MD model.

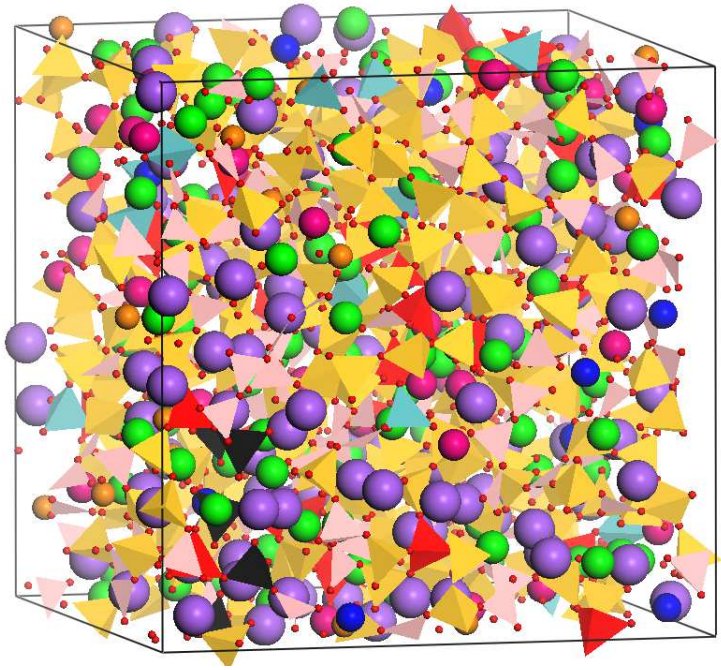

Figure 5.14: Visual representation of the MW + POCO #2 MD model.

Table 5.12: Key for Figure 5.13 and Figure 5.14.

gold tetrahedra:	silicon	light blue/black polyhedra:	molybdenum
small red spheres:	oxygen	pink triangles/tetrahedra:	boron
red polyhedra:	aluminium	purple spheres:	sodium
orange spheres:	iron	pink spheres:	magnesium
dark blue spheres:	zirconium	green spheres:	lithium

In both models of simplified MW + POCO molybdenum polyhedra were observed to be linked to silicon and boron tetrahedra/triangles. However, the MW + POCO #2 model also contains a cluster of MoO_4 tetrahedra (coloured black) surrounded by sodium atoms which can be observed towards the bottom left of **Figure 5.14**. This is consistent with crystal phases containing sodium and molybdenum that were observed in the Raman spectra for MW + POCO (**Section 4.6.3**). Such a cluster was not observed in the MW #1 model (shown in **Figure 5.13**). The connectivity between molybdenum polyhedra with boron and silicon is discussed further in **Section 5.4**.

Radial Distribution Functions (MW + POCO)

The Radial Distribution Functions (RDFs) for each cation to oxygen obtained from the simplified MW + POCO simulations are shown in **Figure 5.15** below. The average element-oxygen nearest neighbour distances $<d_{X\text{-}O}>$, are presented in **Table 5.13** below.

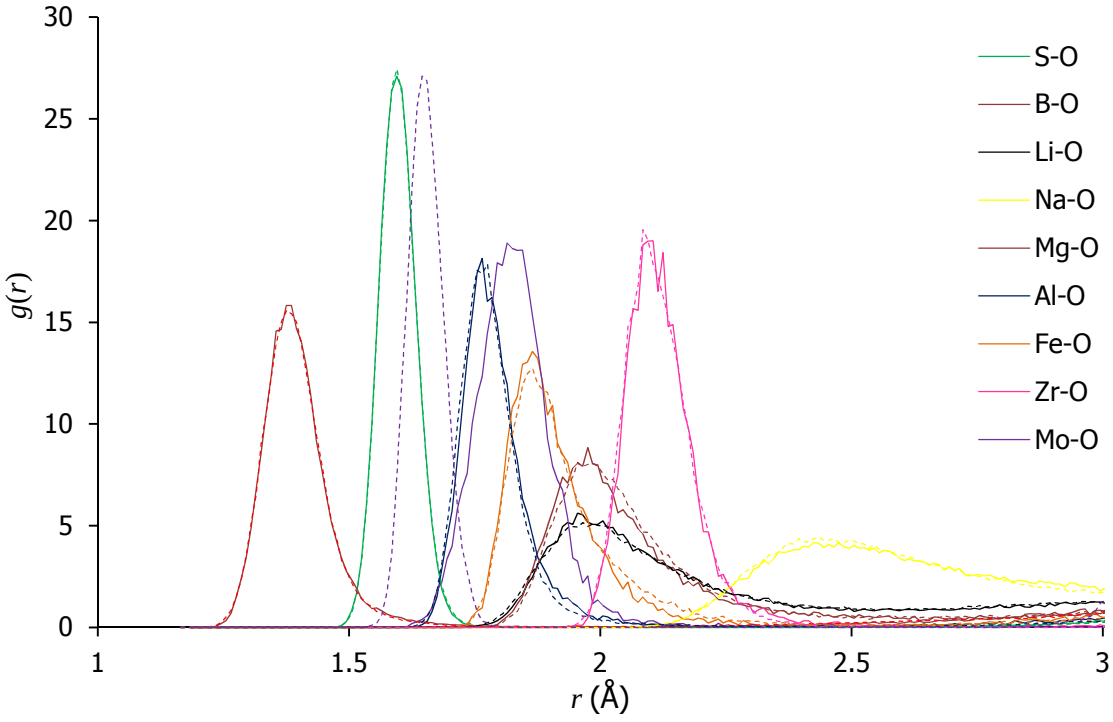

Figure 5.15: RDFs predicted by MD simulations for simplified MW + POCO. Solid lines are from MW + POCO #1 and dashed lines are from MW + POCO #2.

Table 5.13: Average element-oxygen nearest neighbour distances from simulations of simplified MW + POCO (σ is the standard deviation).

Model	Nearest neighbour distances <$d_{X\text{-}O}$> (Å)								
	Si-O	B-O	Li-O	Na-O	Mg-O	Al-O	Fe-O	Zr-O	Mo-O
MW + POCO #1	1.60	1.40	2.08	2.71	2.06	1.79	1.91	2.12	1.83
σ (Å)	0.001	0.01	0.03	0.10	0.03	0.01	0.01	0.01	0.01
MW + POCO #2	1.60	1.40	2.10	2.64	2.05	1.79	1.93	2.12	1.65
σ (Å)	0.002	0.005	0.04	0.07	0.02	0.01	0.02	0.01	0.001

The average Si-O bond length was found to be 1.60 Å in both MW + POCO simulations. These values are consistent with the Si-O bond lengths predicted by the simulations of Low Magnox, High Magnox and the simulations of ABS and MW glass (using Buckingham potentials) reported in **Chapter 3**.

The average B-O bond length was found to be 1.40 Å in both MW + POCO simulations. These values are considered to be consistent with those predicted by the Low Magnox and High Magnox simulations but are slightly higher than the values of 1.38 Å and 1.39 Å found in the simulations of ABS and MW glass using Buckingham potentials reported in **Chapter 3**.

The average Zr-O bond length was found to be 2.12 Å in both MW + POCO simulations. These values are considerably shorter than the average value of 2.18 Å predicted by Connelly et al. [6].

As observed in the Low Magnox and High Magnox simulations, the application of a three-body potential to the O-Mo-O bond significantly reduces the average Mo-O nearest neighbour distance and reduces the variation in nearest neighbour distance. The average Mo-O distances for MW + POCO also vary considerably from the experimentally determined value of 1.78 Å [7] as they did in the models Low and High Magnox.

Coordination Numbers (MW + POCO)

The coordination numbers for silicon and boron from the models of simplified MW + POCO are shown in **Figure 5.16** below. The cumulative coordination numbers for molybdenum are shown in **Figure 5.17**.

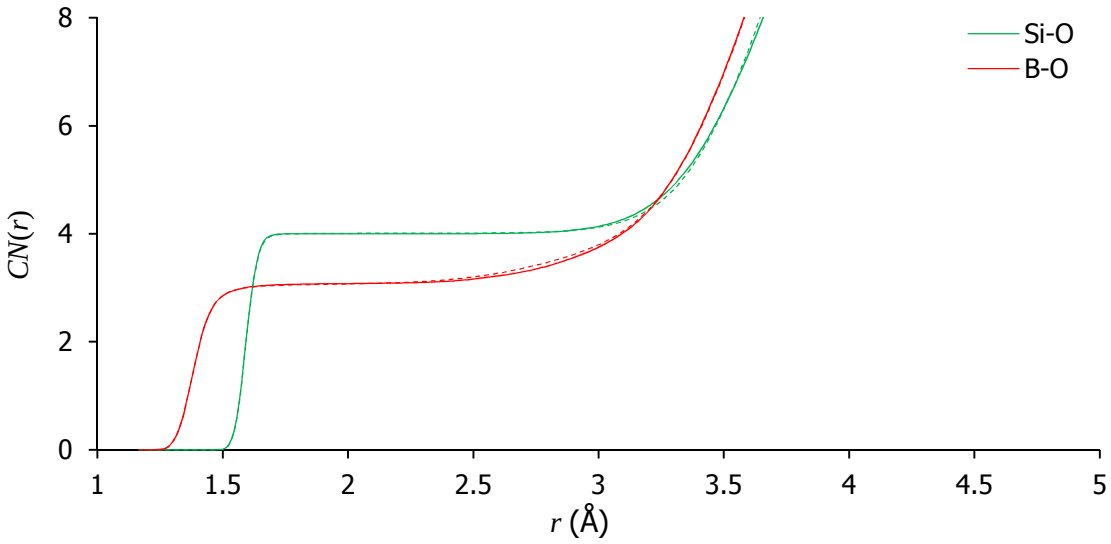

Figure 5.16: Coordination numbers for Si-O and B-O from simulations of simplified MW + POCO. Solid lines are from MW + POCO #1 and dashed lines are from MW + POCO #2.

All silicon atoms were found to be four-coordinated in the MW + POCO #1 simulation. In the MW + POCO #2 simulation, 99 % of the silicon atoms were found to be four-coordinated with the remaining 1 % being five-coordinated (which is considered unrealistic). In the MW + POCO #1 simulation, boron atoms were found to be 92 % three-coordinated and 8 % four-coordinated. In MW + POCO #2, 93 % of the boron atoms were three-coordinated and the remaining 7 % were four-coordinated. The O-Mo-O three-body potential has little effect on silicon or boron coordination as found in the Low and High Magnox simulations.

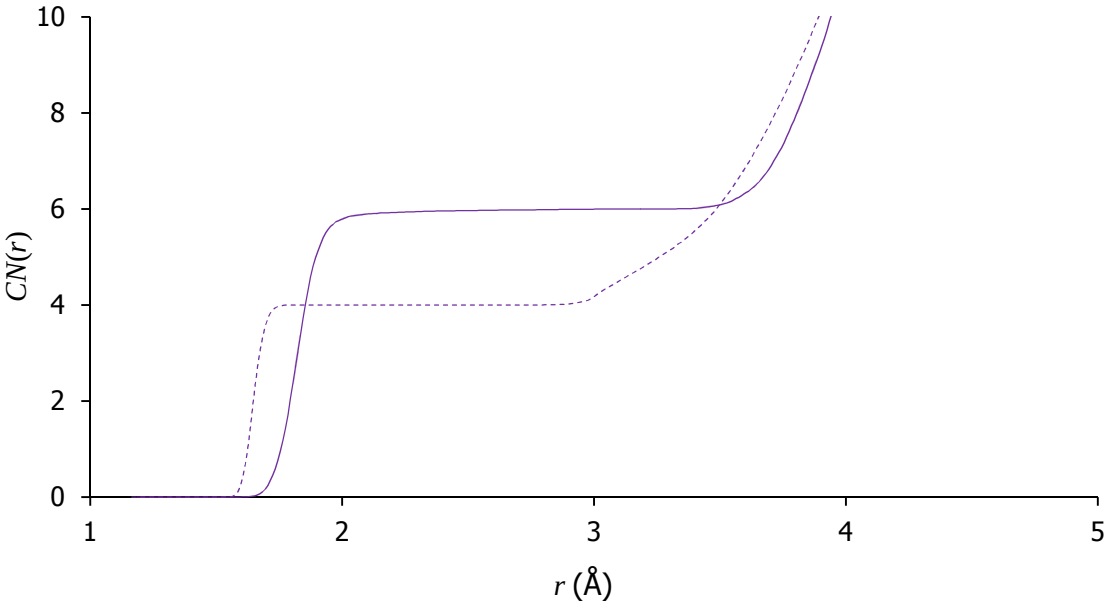

Figure 5.17: Coordination number for Mo-O from simulations of simplified MW + POCO. The solid line is from MW+POCO #1 and the dashed line is from MW+POCO #2.

The coordination number function for MW + POCO #1 shows molybdenum with a coordination number of six between r = 2.00–3.30 Å. The molybdenum coordination number in MW + POCO #2 is forced to remain at four until reaching the three-body potential cut-off value of 3.00 Å.

Bond Angle Distributions (MW + POCO)

The bond angle distributions for O-Si-O, O-B-O and O-Mo-O from the MW + POCO simulations are shown in **Figure 5.18** below. The average bond angles found in the simulations are reported in **Table 5.14**.

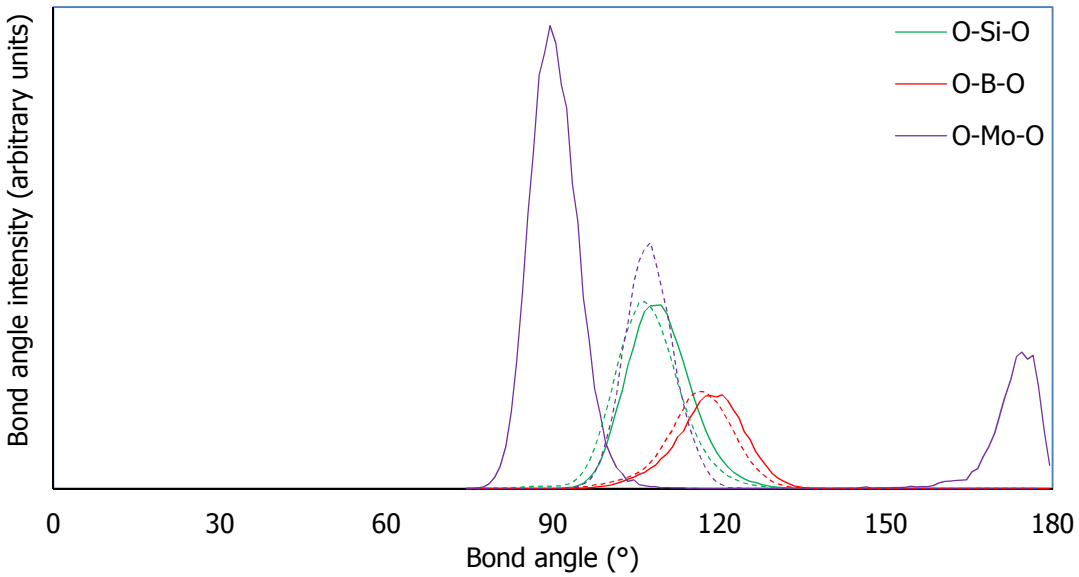

Figure 5.18: Bond angle distribution from simulations of simplified MW + POCO. Solid lines are from MW + POCO #1 and dashed lines are from MW + POCO #2.

Table 5.14: Average bond angles from simulations of simplified MW + POCO (σ is the standard deviation).

Model	<O-Si-O>	<O-B-O>	<O-Mo-O>
MW + POCO #1	109°	118°	90°
σ	6°	8°	5°
MW + POCO #2	109°	118°	109°
σ	7°	8°	5°

As with the Low and High Magnox simulations, both MW + POCO simulations produce average bond angles of 109° for O-Si-O indicating that silicon atoms are forming SiO_4 tetrahedra and the average bond angle for O-B-O was found to be 117° in both simulations. The BAD for O-Mo-O in MW + POCO #1 contains two bands: one with a mean at 90° and the other with a mean at 173° (σ = 6°); suggesting the presence of octahedral MoO_6 units. In the MW + POCO #2 model, the average O-Mo-O angle was found to be 109° indicating that molybdenum is forming MoO_4 tetrahedra.

5.4. Chapter 5 Discussion

The Si-O bond lengths found in all the MD models of simulated vitrified wasteforms were found to be consistent with those found in the models of ABS and MW glasses reported in **Chapter 3**. The B-O bond lengths were consistent in all models however, separate bond lengths for three- and four-coordinated boron could not be distinguished from the RDFs. Nearest neighbour distances for Al-O and Zr-O were considered to be consistent in all models (i.e. differences were no more than 0.04 Å). Differences between 0.04 and 0.07 Å were found in the mean Li-O, Mg-O and Fe-O distances. The maximum difference in Na-O distance between the models was found to be 0.12 Å. The application of a three-body potential to the O-Mo-O angles forced the creation of MoO_4 tetrahedra but also influenced Mo-O bond length. Applying the O-Mo-O potential resulted in short Mo-O bond lengths when compared to experimental data [7]. However, in the absence of a three-body potential, the bond length was longer than those found by experiment. These results imply that the Mo-O potential parameters would benefit from further adjustment.

The mean O-Si-O and O-B-O and O-Mo-O bond angles were consistent in all models. O-Mo-O Bond angles of 90° and 173° were found in all #1 models which did not include a three-body potential. The mean O-Mo-O bond angle was found to be 109° in all #2 models which included a three-body potential.

The amount of four-coordinated silicon was found to be ≥ 97 % in all models. The amount of four-coordinated boron was found to be between 7 and 12 %. From the results in **Chapter 3**, it is expected that these amounts could be greater if alternative B-O potential parameters were applied. The coordination number of molybdenum changed from six to four when a three-body potential was applied.

From manual analysis of the models shown in **Figures 1.1**, **1.2**, **5.7**, **5.8**, **5.13** and **5.14**, the number of boron and silicon atoms connected to each molybdenum atom (via oxygens, i.e. Mo-O-Si or Mo-O-B) were determined.

In **Table 5.15** below, the molybdenum atoms in each model have been segregated into two groups; those which connect to two or less silicon and/or boron atoms and those which connect to three or more silicon and/or boron atoms. For example, if two molybdenum atoms in a model were each found to share oxygens with four silicon atoms and two boron atoms, this will be denoted as '2 × Mo-4Si+2B' in **Table 5.15**. Molybdenum atoms that do not share oxygens with boron or silicon are denoted as 'Mo' and 'none' indicates that no molybdenum atoms were segregated into the group concerned.

Table 5.15: MoO polyhedra connectivity to silicon and boron.

Wasteform	Model	Mo polyhedron connected to two or less Si/B	Mo polyhedron connected to three or more Si/B
Low Magnox	#1	none	1 × Mo-3Si+2B 1 × Mo-3Si
	#2	1 × Mo 1 × Mo-2B	none
High Magnox	#1	1 × Mo-1Si+1B	2 × Mo-4Si+1B 1 × Mo-4Si 1 × Mo-3Si+3B 1 × Mo-2Si+1B 1 × Mo-1Si+2B
	#2	2 × Mo 1 × Mo-1B 4 × Mo-1Si	none
MW + POCO	#1	1 × Mo-1Si 4 × Mo-2Si 2 × Mo-1Si+1B	1 × Mo-3Si+2B 2 × Mo-2Si+1B 2 × Mo-1Si+2B 2 × Mo-1Si+3B 2 × Mo-4Si+1B 1 × Mo-3Si
	#2	3 × Mo-1B 1 × Mo-2Si 2 × Mo-1Si 11 × Mo (includes 5 coloured black in **Figure 5.14)**	none

From **Table 5.15** there is a clear difference between the '#1' and '#2' models. In the #2 models, all the molybdenum atoms form only a maximum of two links with silicon and/or boron. These results indicate strong a tendency for MoO_4 tetrahedra to be detached from the borosilicate network in the #2 models. This is particularly true in the case of MW + POCO where a cluster of five molybdenum atoms were observed (see black tetrahedra in **Figure 5.14**).

It is recognised that only a small number of zirconium and molybdenum cations were included in the models and this may have reduced the statistical validity of calculated features such as mean cation-oxygen distances.

5.5. Chapter 5 References

[1] W. Smith, T. R. Forester and I. T. Todorov, The DL_POLY Classic User Manual, vol. 16, Daresbury, United Kingdom: Daresbury Laboratory, 2006, pp. 1911-1918.

[2] R. J. Short, R. J. Hand, N. N. Hyatt and G. Möbus, "Environment and oxidation state of molybdenum in simulated high level waste glass compositions," *J. Nucl. Mater.*, vol. 340, pp. 179-186, (2005).

[3] G. Mountjoy, B. M. Al-Hasni and C. Storey, "Structural organisation in oxide glasses from molecular dynamics modelling," *J. Non Cryst. Solids.*, vol. 357, no. 14, pp. 2522-2529, 2011.

[4] D. M. Teter, Private communication, 1999.

[5] FIZ Karlsruhe - Leibniz-Insitut für Informationsinfrastruktur GmbH, "Inorganic Crystal Structure Database," Eggenstein-Leopoldshafen.

[6] A. J. Connelly, K. P. Travis, R. J. Hand, N. C. Hyatt and E. Maddrell, "Composition-Structure Relationships in Simplified Nuclear Waste Glasses: 2. The Effect of ZrO_2 Additions," *J. Am. Ceram. Soc.*, vol. 94, no. 1, pp. 78-85, 2011.

[7] G. Calas, M. Le Grand, L. Galoisy and D. Ghaleb, "Structural role of molybdenum in nuclear glasses: an EXAFS study," *J. Nucl. Mater.*, vol. 322, no. 1, pp. 15-20, 2003.

6. Discussion, Further Work and Conclusions

6.1. Discussion: MD Models of Alkali Borosilicate Glasses

6.1.1. MD Models of B_2O_3 Glass

GULP was used to derive a set of Buckingham potential parameters for the B-O interaction. In general, the Buckingham potentials produced smaller differences between the initial and final unit cell parameters and average bond lengths than the BHM potentials. Having stated this, the difference between the initial and final unit cell parameters and average bond lengths are larger for structures containing boron; this indicates that the manually derived B-O potential parameters would have benefitted from further refinement.

The models of B_2O_3 using both Buckingham and BHM potentials produced mean bond lengths close to those found in experimental studies of B_2O_3 glass (i.e. < 2 % difference). The mean O-B-O bond angles were found to be approximately 120° as would be expected for pure B_2O_3 glass. All boron atoms were found to be three-coordinated in the simulation that utilised Buckingham potentials. In the simulation that used BHM potentials, a small number of four-coordinated boron was found (which is unrealistic for pure B_2O_3). These results suggest that the Buckingham potential parameters favour three-coordinated boron.

6.1.2. MD Models of ABS (K=3, R=0.15) and MW Glass

When using BHM potentials two separate bond lengths for three- and four-coordinated boron could be distinguished whereas only one bond length (close to the value expected for three-coordinated boron) was found when using Buckingham potentials. This finding supports the conclusion above that the derived B-O Buckingham potentials favour three-coordinated boron. Li-O nearest neighbour distances were consistent between the models. The mean Na-O nearest neighbour distances found using Buckingham potentials were more

consistent with experimental data than the Na-O distances determined using BHM potentials.

In all models the majority of silicon atoms were found to be four-coordinated. However the models made using BHM potentials had a higher number of five-coordinated silicon atoms than their Buckingham potential counterparts. Applying a three-body potential to O-Si-O triplets would have been beneficial.

The application of BHM potentials resulted in much higher proportions of four-coordinated boron in the ABS #2 and MW #2 glass models being consistent with experimentally determined values. However, it should be noted that use of the NPT ensemble allows the volume (and density) of the modelled glass to change.

Network connectivity analysis showed that a higher number of four-coordinated boron atoms results in higher network connectivity.

It is concluded that the Buckingham and BHM potential parameters applied can adequately reproduce structural features such as Si-O and Li-O bond lengths/nearest neighbour distances and O-Si-O bond angles in models of alkali borosilicate glasses. The Buckingham potential parameters more realistically reproduced structural features such as Si-O coordination and Na-O distances. The BHM potentials more accurately reproduced B-O bond lengths and coordination numbers.

6.2. Discussion: Experimental Studies

6.2.1. Density Determination of Simulated Vitrified Wasteforms

Densities of simulated vitrified wasteforms were determined using helium pycnometry, however no data was found in the literature for comparison. For evaluation purposes, it would have been useful to measure the density of the MW-½Li base glass mixture and compare the experimentally determined value with values in the literature. This would have provided a useful cross check.

6.2.2. X-ray Fluorescence Spectroscopy

X-ray fluorescence spectroscopy data was obtained from the MW-½Li and Ca/Zn-½Li base glasses and the simulated vitrified wasteforms. The XRF results were not in quantitative agreement with the compositions provided by NNL. These discrepancies are due to the lack of standard options for processing results from bulk powder samples. Notwithstanding this, qualitative trends in the XRF results can be matched to quantitative differences in the composition data provided by NNL.

6.2.3. SEM Imaging and EDX

SEM images of the simulated vitrified wasteforms showed evidence of phase separation. SEM EDX revealed phases containing molybdenum were found in wasteforms with MoO_3 concentrations greater than 2.5 wt. % (i.e. MW + POCO and Ca/Zn + POCO). Phases containing ruthenium were found in the Low Magnox wasteform. In High Magnox, a 10 µm sized phase containing cerium and zirconium was seen along with evidence of $(Mg,Ni)(Fe,Cr)_2O_4$ type phases. In MW + POCO, a micron size phase containing cerium, zirconium and gadolinium was found. Evidence of $CaMoO_4$ and RuO_2 phase separation was observed in Ca/Zn + POCO.

6.2.4. Raman Spectroscopy

Raman spectra from Low and High Magnox provided evidence of molybdenum in a glassy environment however no evidence of molybdenum phase separation was observed. Bands in the Raman spectra for MW + POCO were consistent with those from MoO_4 units in a glass environment and with molybdenum in crystalline phases such as $Na(Nd,Gd)(MoO_4)_2$. Raman spectra from Ca/Zn + POCO showed evidence of $CaMoO_4$ and RuO_2 crystal phases in addition to MoO_4 units in a glass network.

6.3. Discussion: MD Models of Simulated Vitrified Wasteforms

Due to the lack of compatible potential parameters, MD models of simulated vitrified wasteforms were not made using BHM potentials as was done for borate and alkali borosilicate glasses. However, models of wasteforms were made using Buckingham potentials. The potential parameters for the B-O and Mo-O interactions were derived manually. From the results of the models of ABS and MW glass, it was expected that the fraction of four-coordinated boron found in the models would be underestimated using Buckingham potentials.

In the models with no O-Mo-O three-body potential applied (i.e. the #1 models), molybdenum tended to form MoO_6 octahedra. Applying a three-body potential to constrain the O-Mo-O bond angles to 109° effectively forced the formation of MoO_4 tetrahedra (as done in the #2 models).

For all wasteforms modelled, the MoO_4 bond lengths were found to differ from experimental data and it is expected that further refinement of the Mo-O two-body potential parameters would improve this.

Manual inspection of images produced by the MD models showed that in the #1 models, MoO_6 octahedra tended to share oxygen atoms with silicon and boron network formers. In the #2 models MoO_4 tetrahedra tended to be detached from the borosilicate network. In the MW + POCO #2 model a cluster of MoO_4 tetrahedra surrounded by sodium atoms was observed – a result consistent with what was observed in the Raman spectra for MW + POCO. This is considered to be a realistic feature of the model.

6.4. Further Work

6.4.1. Improvements to MD Models of Alkali Borosilicate Glasses

The B-O Buckingham two-body potential parameters would benefit from further refinement so that more realistic boron coordination numbers are formed when making models of alkali borosilicate glasses and vitrified wasteforms. In the case of alkali borosilicate glasses, models containing greater numbers of sodium and lithium atoms would improve the statistical validity of results.

6.4.2. Improvements to Experimental Work

Calibration and setup of XRF analysis software to process spectra from powder samples would improve the XRF results reported in this work.

Only a limited number of SEM EDX spectra were acquired in this work due to equipment availability. Further SEM EDX work (in particular on MW + POCO) may reveal other phases in the simulated vitrified wasteforms other than those reported in this work.

Raman spectroscopy results could potentially be improved by using a higher resolution grating along with longer scanning durations.

6.4.3. Improvements to MD Models of Simulated Vitrified Wasteforms

Further refinement of the Mo-O two-body potential parameters is recommended in order to improve the Mo-O bond lengths reported in this work. Models containing greater number of zirconium and molybdenum atoms would improve the statistical validity of results such as Mo-O and Zr-O bond lengths/nearest neighbour distances. Repeats of the models presented in this work could also be attempted with different initial atomic configurations to check reproducibility.

Due to the lack of a Zn-O potential compatible with the partial charge of -1.2e for oxygen, models of Ca/Zn and Ca/Zn + POCO could not be attempted within the timescale of this project. A set of compatible Zn-O potential parameters could

be manually derived using GULP as was done with B-O and Mo-O. With suitable Zn-O potential parameters to hand, MD models of Ca/Zn and Ca/Zn + POCO could be attempted. It would be particularly interesting to see if a model of Ca/Zn + POCO could predict $CaMoO_4$ phase separation as observed in experimental methods.

6.5. Conclusions

SEM EDX and Raman studies of simulated vitrified nuclear wasteforms have been carried out and have identified phase separation in simulated vitrified wasteforms. The results produced are consistent with those found in the literature.

This study reports (to the best of the author's knowledge) the first attempt to create molecular dynamics models of UK vitrified nuclear waste forms. These models provide an insight into the incorporation of tetrahedral MoO_4 units into the wasteforms. This includes evidence of the tendency for phase separation of MoO_4 units with sodium in the MW+POCO wasteform. This feature was also observed in the experimental results. A number of suggestions have been provided as to how the models could be further improved.

APPENDIX A – GULP Results: Buckingham and Three-body Potential Parameters

Buckingham Two-Body Potential Parameters

Table A1 below lists the Buckingham potential parameters used to generate the MD simulations reported in this work. **Table A3**–**Table A21** present the output of the GULP package for various crystal structures using these interactions.

Table A1: Buckingham potential parameters.

Atom 1	Charge (e)	Atom 2	Charge (e)	A (eV)	ρ (Å)	C (eV·Å6)
O	-1.2	O	-1.2	1844.8	0.34365	192.58
Si	2.4	O	-1.2	13702.9	0.19382	54.68
B	1.8	O	-1.2	4300.0	0.18500	11.80
Na	0.6	O	-1.2	4383.8	0.24384	30.70
Li	0.6	O	-1.2	41051.9	0.15611	0.00
Mg	1.2	O	-1.2	7063.5	0.21090	19.21
Al	1.8	O	-1.2	12201.4	0.19563	32.00
Fe	1.8	O	-1.2	19952.3	0.18254	4.66
Zr	2.4	O	-1.2	17943.4	0.22663	127.65
Mo	3.6	O	-1.2	5700.0	0.22900	30.00
Ca	1.2	O	-1.2	7747.2	0.25262	93.109

Note that: i) all interactions were obtained from [1] with except B-O and Mo-O which were derived manually using GULP (**Section 3.2.1**), ii) the Ca-O interaction was not used in any MD simulations.

Three-Body Potential Parameters

Table A2: Three body potential parameters for the O-Mo-O triplet

K (eV)	θ_0 (°)	ρ_1 (Å)	ρ_2 (Å)
100.00	109.47	1.00	1.00

Buckingham Potential Results

Table A3: GULP results for diboron trioxide (B_2O_3) ICSD structure 16021 using the Buckingham potential parameters presented in Table A1.

Parameter	Initial value	Final value	Difference	Percent change
Volume (Å^3)	135.77	153.70	17.93	13.21
a (Å)	4.34	4.58	0.24	5.53
b (Å)	4.34	4.58	0.24	5.53
c (Å)	8.34	8.46	0.12	1.44
α(°)	90.00	90.00	0.00	0.00
β(°)	90.00	90.00	0.00	0.00
γ(°)	120.00	120.00	0.00	0.00
$<d_{B\text{-}O}>$ (Å)	1.37	1.38	0.01	0.73

Table A4: GULP results for alpha quartz (SiO_2) ICSD structure 16331 using the Buckingham potential parameters presented in Table A1.

Parameter	Initial value	Final value	Difference	Percent change
Volume (Å^3)	113.25	114.86	1.61	1.42
a (Å)	4.92	4.94	0.02	0.41
b (Å)	4.92	4.94	0.02	0.41
c (Å)	5.40	5.45	0.05	0.93
α(°)	90.00	90.00	0.00	0.00
β(°)	90.00	90.00	0.00	0.00
γ(°)	120.00	120.00	0.00	0.00
$<d_{Si\text{-}O}>$ (Å)	1.62	1.59	-0.03	-1.85

Table A5: GULP results for alpha quartz (SiO_2) ICSD structure 83849 using the Buckingham potential parameters presented in Table A1.

Parameter	Initial value	Final value	Difference	Percent change
Volume (Å^3)	112.96	114.86	1.90	1.68
a (Å)	4.91	4.94	0.03	0.61
b (Å)	4.91	4.94	0.03	0.61
c (Å)	5.40	5.45	0.05	0.93
α(°)	90.00	90.00	0.00	0.00
β(°)	90.00	90.00	0.00	0.00
γ(°)	120.00	120.00	0.00	0.00
$<d_{Si\text{-}O}>$ (Å)	1.61	1.59	-0.02	-1.24

Table A6: GULP results for lithium oxide (Li_2O) ICSD structure 642216 using the Buckingham potential parameters presented in Table A1.

Parameter	Initial value	Final value	Difference	Percent change
Volume (Å^3)	103.11	97.67	-5.44	-5.28
a (Å)	4.69	4.61	-0.08	-1.71
b (Å)	4.69	4.61	-0.08	-1.71
c (Å)	4.69	4.61	-0.08	-1.71
α(°)	90.00	90.00	0.00	0.00
β(°)	90.00	90.00	0.00	0.00
γ(°)	90.00	90.00	0.00	0.00
$<d_{Li\text{-}O}>$ (Å)	2.03	1.99	-0.04	-1.97

Table A7: GULP results for lithium oxide (Li_2O) ICSD structure 60431 using the Buckingham potential parameters presented in Table A1.

Parameter	Initial value	Final value	Difference	Percent change
Volume (Å^3)	24.78	24.42	-0.36	-1.45
a (Å)	3.27	3.26	-0.01	-0.31
b (Å)	3.27	3.26	-0.01	-0.31
c (Å)	3.27	3.26	-0.01	-0.31
α(°)	60.00	60.00	0.00	0.00
β(°)	60.00	60.00	0.00	0.00
γ(°)	60.00	60.00	0.00	0.00
$<d_{Li\text{-}O}>$ (Å)	2.00	1.99	-0.01	-0.49

Table A8: GULP results for sodium oxide (Na_2O) ICSD structure 644917 using the Buckingham potential parameters presented in Table A1.

Parameter	Initial value	Final value	Difference	Percent change
Volume (Å^3)	42.97	40.57	-2.40	-5.59
a (Å)	3.93	3.86	-0.07	-1.78
b (Å)	3.93	3.86	-0.07	-1.78
c (Å)	3.93	3.86	-0.07	-1.78
α(°)	60.00	60.00	0.00	0.00
β(°)	60.00	60.00	0.00	0.00
γ(°)	60.00	60.00	0.00	0.00
$<d_{Na\text{-}O}>$ (Å)	2.41	2.36	-0.05	-2.07

Table A9: GULP results for sodium borosilicate ($NaBSiO_4$) ICSD structure 39459 using the Buckingham potential parameters presented in Table A1.

Parameter	Initial value	Final value	Difference	Percent change
Volume (Å^3)	430.69	461.87	31.18	7.24
a (Å)	8.04	8.22	0.18	2.24
b (Å)	8.04	8.22	0.18	2.24
c (Å)	7.70	7.88	0.18	2.34
α(°)	90.00	90.00	0.00	0.00
β(°)	90.00	90.00	0.00	0.00
γ(°)	120.00	120.00	0.00	0.00
$<d_{B\text{-}O}>$ (Å)	1.45	1.51	0.06	4.14
$<d_{Si\text{-}O}>$ (Å)	1.63	1.59	-0.04	-2.45
$<d_{Na\text{-}O}>$ (Å)	2.49	2.63	0.14	5.62

Table A10: GULP results for disodium boron oxide ($Na_2B_4O_7$) ICSD structure 2040 using the Buckingham potential parameters presented in Table A1.

Parameter	Initial value	Final value	Difference	Percent change
Volume (Å^3)	588.34	623.71	35.37	6.01
a (Å)	6.54	6.71	0.17	2.60
b (Å)	8.62	8.85	0.23	2.67
c (Å)	10.49	10.61	0.12	1.14
α(°)	93.28	93.50	0.22	0.24
β(°)	94.87	97.05	2.18	2.30
γ(°)	90.84	88.96	-1.88	-2.07
$<d_{B\text{-}O[3]}>$ (Å)	1.37	1.38	0.01	0.73
$<d_{B\text{-}O[4]}>$ (Å)	1.48	1.52	0.04	2.70
$<d_{Na\text{-}O}>$ (Å)	2.53	2.61	0.08	3.16

Table A11: GULP results for sodium dilithium borate ($NaLi_2BO_3$) ICSD structure 62532 using the Buckingham potential parameters presented in Table A1.

Parameter	Initial value	Final value	Difference	Percent change
Volume (Å^3)	547.41	562.98	15.57	2.84
a (Å)	9.51	9.34	-0.17	-1.79
b (Å)	12.04	12.21	0.17	1.41
c (Å)	4.93	5.03	0.10	2.03
α(°)	90.00	90.00	0.00	0.00
β(°)	104.00	101.08	-2.92	-2.81
γ(°)	90.00	90.00	0.00	0.00
$<d_{B\text{-}O}>$ (Å)	1.38	1.37	-0.01	-0.72
$<d_{Li\text{-}O}>$ (Å)	1.99	2.02	0.03	1.51
$<d_{Na\text{-}O}>$ (Å)	2.49	2.51	0.02	0.80

Table A12: GULP results for magnesium oxide (MgO) ICSD structure 88058 using the Buckingham potential parameters presented in Table A1.

Parameter	Initial value	Final value	Difference	Percent change
Volume (Å^3)	18.79	18.24	-0.55	-2.93
a (Å)	2.98	2.95	-0.03	-1.01
b (Å)	2.98	2.95	-0.03	-1.01
c (Å)	2.98	2.95	-0.03	-1.01
α(°)	60.00	60.00	0.00	0.00
β(°)	60.00	60.00	0.00	0.00
γ(°)	60.00	60.00	0.00	0.00
$<d_{Mg\text{-}O}>$ (Å)	2.11	2.09	-0.02	-0.95

Table A13: GULP results for aluminium oxide (Al_2O_3) ICSD structure 51687 using the Buckingham potential parameters presented in Table A1.

Parameter	Initial value	Final value	Difference	Percent change
Volume (Å^3)	84.98	86.40	1.42	1.67
a (Å)	5.13	5.18	0.05	0.97
b (Å)	5.13	5.18	0.05	0.97
c (Å)	5.13	5.18	0.05	0.97
α(°)	55.29	54.80	-0.49	-0.89
β(°)	55.29	54.80	-0.49	-0.89
γ(°)	55.29	54.80	-0.49	-0.89
$<d_{Al\text{-}O}>$ (Å)	1.91	1.93	0.02	1.05

Table A14: GULP results for iron (III) oxide alpha (Fe_2O_3) ICSD structure 82902 using the Buckingham potential parameters presented in Table A1.

Parameter	Initial value	Final value	Difference	Percent change
Volume (Å^3)	100.63	98.96	-1.67	-1.66
a (Å)	5.43	5.41	-0.02	-0.37
b (Å)	5.43	5.41	-0.02	-0.37
c (Å)	5.43	5.41	-0.02	-0.37
α(°)	55.28	55.03	-0.25	-0.45
β(°)	55.28	55.03	-0.25	-0.45
γ(°)	55.28	55.03	-0.25	-0.45
$<d_{Fe\text{-}O}>$ (Å)	2.03	2.01	-0.02	-0.99

Table A15: GULP results for zirconium oxide (ZrO_2) ICSD structure 80046 using the Buckingham potential parameters presented in Table A1.

Parameter	Initial value	Final value	Difference	Percent change
Volume (Å^3)	140.71	138.27	-2.44	-1.73
a (Å)	5.15	5.14	-0.01	-0.19
b (Å)	5.21	5.24	0.03	0.58
c (Å)	5.32	5.18	-0.14	-2.63
α(°)	90.00	90.00	0.00	0.00
β(°)	99.23	97.93	-1.30	-1.31
γ(°)	90.00	90.00	0.00	0.00
$<d_{Zr\text{-}O}>$ (Å)	2.15	2.16	0.01	0.47

Table A16: GULP results for molybdenum oxide (MoO_3) ICSD structure 35076 using the Buckingham potential parameters presented in Table A1.

Parameter	Initial value	Final value	Difference	Percent change
Volume (Å^3)	202.95	175.51	-27.44	-13.52
a (Å)	3.96	3.55	-0.41	-10.35
b (Å)	13.86	13.71	-0.15	-1.08
c (Å)	3.70	3.60	-0.10	-2.70
α(°)	90.00	90.00	0.00	0.00
β(°)	90.00	90.00	0.00	0.00
γ(°)	90.00	90.00	0.00	0.00
$<d_{Mo\text{-}O}>$ (Å)	1.98	2.13	0.15	7.58

Table A17: GULP results for molybdenum oxide (MoO_3) ICSD structure 80577 using the Buckingham potential parameters presented in Table A1.

Parameter	Initial value	Final value	Difference	Percent change
Volume (Å^3)	100.47	87.76	-12.71	-12.65
a (Å)	3.95	3.55	-0.40	-10.13
b (Å)	3.69	3.60	-0.09	-2.44
c (Å)	7.10	7.08	-0.02	-0.28
α(°)	90.00	90.00	0.00	0.00
β(°)	103.75	104.53	0.78	0.75
γ(°)	90.00	90.00	0.00	0.00
$<d_{Mo\text{-}O}>$ (Å)	1.98	1.98	< 0.01	< 0.01

Table A18: GULP results for disodium molybdate (VI) – gamma (Na_2MoO_4) ICSD structure 151971 using the Buckingham potential parameters presented in Table A1.

Parameter	Initial value	Final value	Difference	Percent change
Volume (Å^3)	895.07	864.86	-30.21	-3.38
a (Å)	6.45	6.48	0.03	0.47
b (Å)	12.78	12.65	-0.13	-1.02
c (Å)	10.86	10.54	-0.32	-2.95
α(°)	90.00	90.00	0.00	0.00
β(°)	90.00	90.00	0.00	0.00
γ(°)	90.00	90.00	0.00	0.00
$<d_{Mo\text{-}O}>$ (Å)	1.52	1.63	0.11	7.24
$<d_{Na\text{-}O}>$ (Å)	2.70	2.62	-0.08	-2.96

Table A19: GULP results for disodium molybdate (VI) – gamma (Na_2MoO_4) ICSD structure 151971 using the Buckingham potential parameters presented in Table A1 and the O-Mo-O three-body potential parameters presented in Table A2.

Parameter	Initial value	Final value	Difference	Percent change
Volume (Å^3)	895.07	917.51	22.44	2.51
a (Å)	6.45	6.15	-0.30	-4.65
b (Å)	12.78	12.12	-0.66	-5.16
c (Å)	10.86	12.31	1.45	13.35
α(°)	90.00	90.00	0.00	0.00
β(°)	90.00	90.00	0.00	0.00
γ(°)	90.00	90.00	0.00	0.00
$<d_{Mo\text{-}O}>$ (Å)	1.52	1.73	0.21	13.82
$<d_{Na\text{-}O}>$ (Å)	2.70	2.60	-0.10	-3.70

Table A20: GULP results for calcium molybdate ($CaMoO_4$) ICSD structure 22351 using the Buckingham potential parameters presented in Table A1.

Parameter	Initial value	Final value	Difference	Percent change
Volume (Å^3)	311.93	311.87	-0.06	-0.02
a (Å)	5.22	5.25	0.03	0.57
b (Å)	5.22	5.25	0.03	0.57
c (Å)	11.43	11.31	-0.12	-1.05
α(°)	90.00	90.00	0.00	0.00
β(°)	90.00	90.00	0.00	0.00
γ(°)	90.00	90.00	0.00	0.00
$<d_{Mo\text{-}O}>$ (Å)	1.76	1.66	-0.10	-5.68
$<d_{Ca\text{-}O}>$ (Å)	2.47	2.54	0.07	2.83

Table A21: GULP results for calcium molybdate ($CaMoO_4$) ICSD structure 22351 using the Buckingham potential parameters presented in Table A1 and the O-Mo-O three-body potential parameters presented in Table A2.

Parameter	Initial value	Final value	Difference	Percent change
Volume (Å^3)	311.9267	326.7775	14.85	4.76
a (Å)	5.224	5.295436	0.08	1.53
b (Å)	5.224	5.295436	0.08	1.53
c (Å)	11.43	11.6533	0.22	1.92
α(°)	90.00	90.00	0.00	0.00
β(°)	90.00	90.00	0.00	0.00
γ(°)	90.00	90.00	0.00	0.00
$<d_{Mo\text{-}O}>$ (Å)	1.76	1.77	0.01	0.57
$<d_{Na\text{-}O}>$ (Å)	2.47	2.51	0.04	1.62

APPENDIX B – GULP Results: Born Huggins Mayer Potential Parameters

Table B1 below lists the Buckingham potential parameters used to generate the MD simulations reported in this work. **Table B2**-**Table B10** present the output of the GULP package for various crystal structures using these interactions.

Table B1: BHM potential parameters obtained from [1].

Atom 1	Charge (e)	Atom 2	Charge (e)	A (eV)	B (Å^{-1})	σ (Å)
O	-2	O	-2	0.1105	2.86	2.84
Si	4	O	-2	0.2763	3.45	2.52
Si	4	B	3	0.663	3.45	1.82
Si	4	Na	1	0.3591	3.45	2.27
Si	4	Li	1	0.442	3.45	1.9
Si	4	Si	4	0.442	3.45	2.2
B	3	B	3	0.884	3.45	1.44
B	3	Na	1	0.5801	3.45	1.89
B	3	Li	1	0.663	3.45	1.52
Na	1	Na	1	0.2763	3.45	2.34
Na	1	Li	1	0.3591	3.45	1.97
Li	1	Li	1	0.442	3.45	1.6
Li	1	O	-2	0.2763	3.45	2.22
B	3	O	-2	0.4973	3.45	2.14
Na	1	O	-2	0.1933	3.45	2.59

BHM Potential Results

Table B2: GULP results for diboron trioxide (B_2O_3) ICSD structure 16021 using the BHM potential parameters presented in Table B1.

Parameter	Initial value	Final value	Difference	Percent change
Volume (Å^3)	135.77	229.65	93.88	69.15
a (Å)	4.34	4.68	0.34	7.83
b (Å)	4.34	4.68	0.34	7.83
c (Å)	8.34	12.13	3.79	45.44
α(°)	90.00	90.00	0.00	0.00
β(°)	90.00	90.00	0.00	0.00
γ(°)	120.00	120.00	0.00	0.00
$<d_{B\text{-}O}>$ (Å)	1.37	1.35	-0.02	-1.46

Table B3: GULP results for alpha quartz (SiO_2) ICSD structure 16331 using the Buckingham potential parameters presented in Table B1.

Parameter	Initial value	Final value	Difference	Percent change
Volume (Å^3)	113.25	125.25	12.00	10.60
a (Å)	4.92	5.07	0.15	3.05
b (Å)	4.92	5.07	0.15	3.05
c (Å)	5.40	5.63	0.23	4.26
α(°)	90.00	90.00	0.00	0.00
β(°)	90.00	90.00	0.00	0.00
γ(°)	120.00	120.00	0.00	0.00
$<d_{Si\text{-}O}>$ (Å)	1.62	1.59	-0.03	-1.85

Table B4: GULP results for alpha quartz (SiO_2) ICSD structure 83849 using the Buckingham potential parameters presented in Table B1.

Parameter	Initial value	Final value	Difference	Percent change
Volume (Å^3)	112.96	125.25	12.29	10.88
a (Å)	4.91	5.07	0.16	3.26
b (Å)	4.91	5.07	0.16	3.26
c (Å)	5.40	5.63	0.23	4.26
α(°)	90.00	90.00	0.00	0.00
β(°)	90.00	90.00	0.00	0.00
γ(°)	120.00	120.00	0.00	0.00
$<d_{Si\text{-}O}>$ (Å)	1.61	1.59	-0.02	-1.24

Table B5: GULP results for lithium oxide (Li_2O) ICSD structure 642216 using the Buckingham potential parameters presented in Table B1.

Parameter	Initial value	Final value	Difference	Percent change
Volume (Å^3)	103.11	99.35	-3.76	-3.65
a (Å)	4.69	4.63	-0.06	-1.28
b (Å)	4.69	4.63	-0.06	-1.28
c (Å)	4.69	4.63	-0.06	-1.28
α(°)	90.00	90.00	0.00	0.00
β(°)	90.00	90.00	0.00	0.00
γ(°)	90.00	90.00	0.00	0.00
$<d_{Li\text{-}O}>$ (Å)	2.03	2.01	-0.02	-0.99

Table B6: GULP results for lithium oxide (Li_2O) ICSD structure 60431 using the Buckingham potential parameters presented in Table B1.

Parameter	Initial value	Final value	Difference	Percent change
Volume (Å^3)	24.78	24.84	0.06	0.24
a (Å)	3.27	3.27	0.00	0.00
b (Å)	3.27	3.27	0.00	0.00
c (Å)	3.27	3.27	0.00	0.00
α(°)	60.00	60.00	0.00	0.00
β(°)	60.00	60.00	0.00	0.00
γ(°)	60.00	60.00	0.00	0.00
$<d_{Li\text{-}O}>$ (Å)	2.03	2.01	0.01	-0.99

Table B7: GULP results for sodium oxide (Na_2O) ICSD structure 644917 using the Buckingham potential parameters presented in Table B1.

Parameter	Initial value	Final value	Difference	Percent change
Volume (Å^3)	42.97	41.66	-1.31	-3.05
a (Å)	3.93	3.89	-0.04	-1.02
b (Å)	3.93	3.89	-0.04	-1.02
c (Å)	3.93	3.89	-0.04	-1.02
α(°)	60.00	60.00	0.00	0.00
β(°)	60.00	60.00	0.00	0.00
γ(°)	60.00	60.00	0.00	0.00
$<d_{Na\text{-}O}>$ (Å)	2.41	2.38	-0.03	-1.24

Table B8: GULP results for sodium borosilicate ($NaBSiO_4$) ICSD structure 39459 using the Buckingham potential parameters presented in Table B1.

Parameter	Initial value	Final value	Difference	Percent change
Volume (Å^3)	430.69	520.13	89.44	20.77
a (Å)	8.04	8.59	0.55	6.84
b (Å)	8.04	8.59	0.55	6.84
c (Å)	7.70	8.14	0.44	5.71
α(°)	90.00	90.00	0.00	0.00
β(°)	90.00	90.00	0.00	0.00
γ(°)	120.00	120.00	0.00	0.00
$<d_{B\text{-}O}>$ (Å)	1.45	1.47	0.02	1.38
$<d_{Si\text{-}O}>$ (Å)	1.63	1.57	-0.06	-3.68
$<d_{Na\text{-}O}>$ (Å)	2.49	2.88	0.39	15.66

Table B9: GULP results for disodium boron oxide ($Na_2B_4O_7$) ICSD structure 2040 using the Buckingham potential parameters presented in Table B1.

Parameter	Initial value	Final value	Difference	Percent change
Volume (Å^3)	588.34	751.94	163.60	27.81
a (Å)	6.54	7.16	0.62	9.48
b (Å)	8.62	9.51	0.89	10.32
c (Å)	10.49	11.20	0.71	6.77
α(°)	93.28	88.63	-4.65	-4.98
β(°)	94.87	99.45	4.58	4.83
γ(°)	90.84	91.13	0.29	0.32
$<d_{B\text{-}O[3]}>$ (Å)	1.48	1.48	-0.03	-2.19
$<d_{B\text{-}O[4]}>$ (Å)	1.37	1.34	0.00	0.00
$<d_{Na\text{-}O}>$ (Å)	2.53	2.65	0.14	5.58

Table B10: GULP results for sodium dilithium borate ($NaLi_2BO_3$) ICSD structure 62532 using the Buckingham potential parameters presented in Table B1.

Parameter	Initial value	Final value	Difference	Percent change
Volume (Å^3)	547.41	622.00	74.59	13.63
a (Å)	9.51	9.90	0.39	4.10
b (Å)	12.04	12.42	0.38	3.16
c (Å)	4.93	5.24	0.31	6.29
α(°)	90.00	90.00	0.00	0.00
β(°)	104.00	105.21	1.21	1.16
γ(°)	90.00	90.00	0.00	0.00
$<d_{B\text{-}O}>$ (Å)	1.38	1.32	-0.06	-4.35
$<d_{Li\text{-}O}>$ (Å)	1.97	1.99	0.00	0.00
$<d_{Na\text{-}O}>$ (Å)	2.49	2.58	0.09	3.61

APPENDIX C – DL_POLY Control File Examples

Control File for B_2O_3 #1 300 K Stage

```
CONTROL: NVT @ 300K
temperature                      300.0
pressure                           0.0
ensemble nvt ber                 2.0
steps                            50000
equilibration                    40000
multiple  step                       5
scale                                5
print                             1000
stack                             1000
stats                             1000
rdf                               1000
time-step                        0.001
primary cutoff                     8.0
cutoff                             9.0
delr width                         1.0
rvdw cutoff                        6.5
ewald precision                  1d-5
print rdf
job time                     621000000
close time                         100
cap                               8000
trajectory                1000 1000  0

finish
```

Control File for ABS #1 2000 K NPT Stage

```
867 R=0.15 2000K NPT

temperature                      2000.0
pressure                           61.0
ensemble npt ber                2.0 2.0

steps                            200000
equilibration                    200000
multiple  step                        5
scale                                 5
print                             1000
stack                             1000
stats                             1000
rdf                               1000
time-step                         .0010
primary cutoff                     8.0
cutoff                            10.0
delr width                         1.0
rvdw cutoff                        6.5
ewald precision                   1d-5

print rdf
job time                      621000000
close time                         100
cap                               8000
trajectory                1000 1000  0
finish
```